Journal of Marine Technology and Environment

Vol.I, year 2026

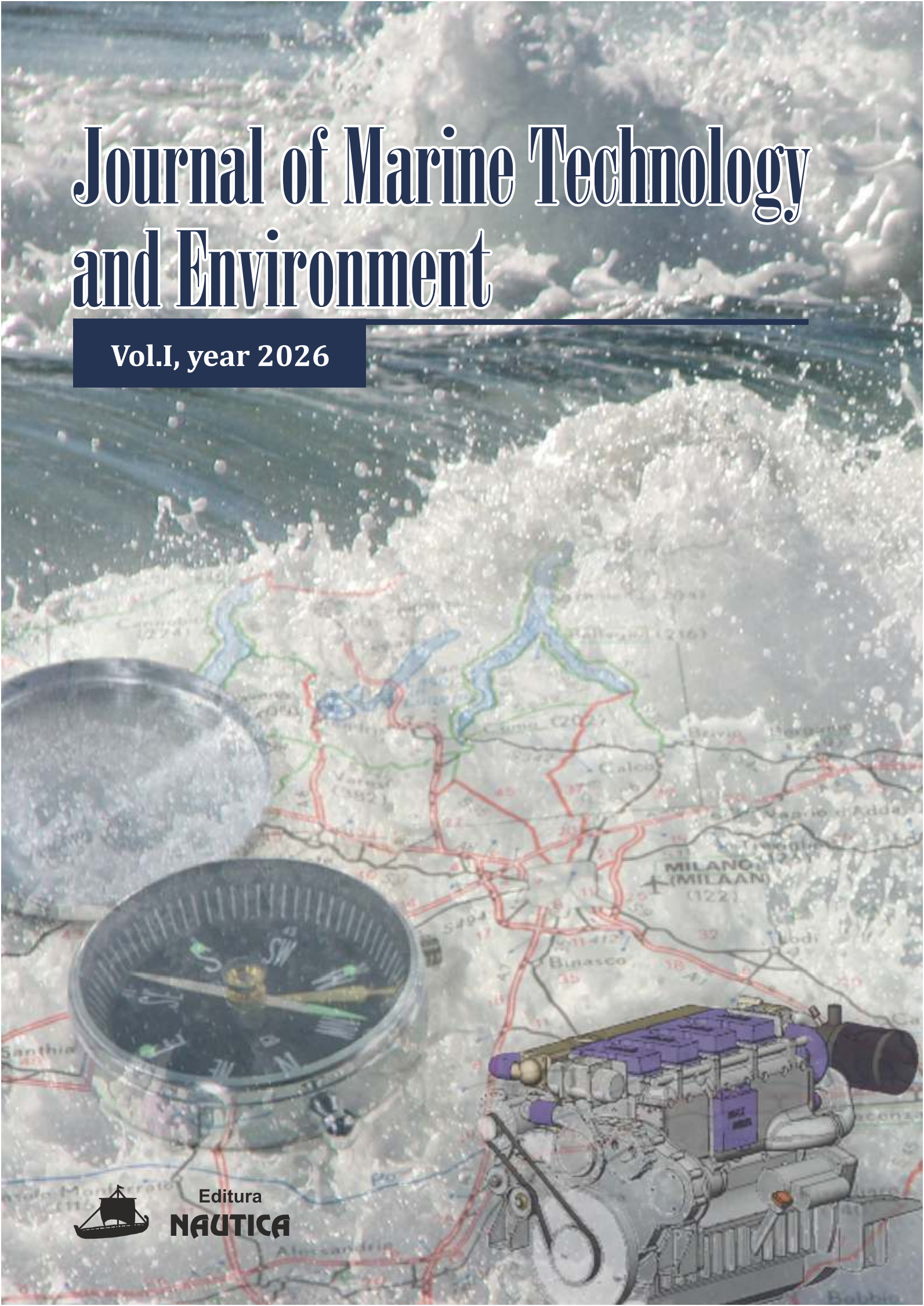

Editura
NAUTICA


UNIVERSITATEA
MARITIMA
CONSTANTA

ISSN (Print): 1844-6116

ISSN (Online): 2501-8795

Journal of Marine
Technology and Environment
DOI: 10.53464/JMTE.01.2026

ISSN (Print): 1844-6116
ISSN (Online): 2501-8795
https://www. jmte.eu

This Journal has been founded in 2008 as a biannual publication of Constanta Maritime University/ROMANIA

Topic: MARITIME AREAS

- Marine Science and Engineering
- Marine Environmental Issues
- Marine Renewable Energy and Sustainability
- Maritime Safety
- Climate changes
- Cyber Security and Maritime Technologies

EDITOR IN CHIEF

PROF. PhD. Eng. Mariana PANAITESCU
Constanta Maritime University, Romania, Marine Engineering Faculty, Department of Engineering Sciences in Mechanics and Environment; 0000-0002-8610-9554

VICE EDITOR IN CHIEF
ASSOC. Prof. PhD. Eng. Feiza-Sucuran MEMET
Constanta Maritime University, Marine Engineering Faculty, Department of General Engineering Sciences , Romania; 0000-0002-3110-4254

GUEST EDITORS
PROF. Ph.D. Tien Anh TRAN
Vietnam, Haiphong Maritime University, Faculty Marine Engineering; University of Malta, Department of Electrical Engineering; 0000-0002-2231-2764

Assistant researcher Jawad LAKZIZ
University Hassan II of Casablanca , Faculty of Science Ben M'Sik, Morocco; 0009-0007-8493-8731

EDITORIAL BOARD

PROF. Dr. Mustafa Taner ALBAYRAK
Piri Reis University, Istanbul, TURKEY; 0000-0002-4743-9235

PROF. PhD. Angelica M.BAYLON
Maritime Academy of Asia and the Pacific, Bataan, PHILIPPINES; 0000-0001-8330-2415

PROF. PhD. Eng. Laurentiu CHIOTOROIU
Jade University of Applied Sciences, GERMANY; 0009-0005-7358-1509

S.L. PhD. Eng. Catalin FAITAR
Constanta Maritime University, Romania; 0000-0001-5950-7795

Creative Commons Attribution BY 4.0 International Licence (CC BY-4.0)

Journal of Marine
Technology and Environment
DOI: 10.53464/JMTE.02.2025

ISSN (Print): 1844-6116
ISSN (Online): 2501-8795
https://www. jmte.eu

Assistant PROF. PhD Mladen JARDAS
University of Rijeka, CROATIA; 0000-0002-2696-8496

PROF.PhD, MSc/ Dip. Momoko KITADA
WORLD MARITIME UNIVERSITY, Malmö, SWEDEN; 0000-0001-6668-8563

PROF. PhD. Kalin Spasov KALINOV
„ Nikola Vaptsarov ” Naval Academy, Varna, BULGARIA; 0000-0002-9705-638X

PROF. PhD. Eng. Gheorghe LAZAROIU
University POLITEHNICA of Bucharest, ROMANIA; 0000-0003-3077-5192

ASSOC. PROF. PhD. Marusya LUBCHEVA
Black Sea Institute Burgas, BULGARIA; 0000-0002-1354-8134

Assoc. PROF. PhD Francesc Xavier MARTINEZ DE OSES
Politehnica University, Barcelona, SPAIN; 0000-0001-9997-6246

DSc. PROF. Irina MAKASHINA
Admiral Ushakov Maritime State University, Novorossisk , RUSSIA; SPIN-COD 6230-9117, AuthorID: 374499

ASSOC.PROF. WALTER K. NADOLNY
State University of, New York , USA

PROF. PhD.Tomasz NEUMANN
Gdynia Maritime University, POLAND; 0000-0002-4149-8293

PROF. PhD. Sc. Nataliya Danailova NIKOLOVA
Nikola Vaptsarov Naval Academy , Varna, BULGARIA; 0000-0001-6160-6280

PROF. PhD. Captain Selcuk NAS
Dokuz Eylül University Maritime Faculty, İzmir, TURKEY; 0000-0001-5053-4594

PROF.PhD. Eng. Fanel – Viorel PANAITESCU
Constanta Maritime University, Romania; 0000-0002-2453-3384

PROF. PhD. Stoyanka Georgieva PETKOVA
University “Prof. Dr. Assen Zlatarov”, Burgas BULGARIA; 0000-0003-0770-7693

PROF.PhD. Hu QINYOU
Merchant Marine College, Shanghai Maritime University, CHINA; 0000-0001-9241-6203

Assoc. Prof. PhD. Gabriel RAICU
RECTOR of Constanta Maritime University, ROMANIA; 0000-0001-5956-7368

PROF. VAdm Eduardo Ma R SANTOS
Maritime Academy of Asia and the Pacific, PHILIPPINES

Assist. PROF. PhD Tanja BRCKO SATLER
University of Ljubljana, SLOVENIA; 0000-0002-1451-2539

Creative Commons Attribution BY 4.0 International Licence (CC BY-4.0)

Journal of Marine
Technology and Environment
DOI: 10.53464/JMTE.01.2026

ISSN (Print): 1844-6116
ISSN (Online): 2501-8795
https://www. jmte.eu

PROF. PhD. Igor SMIRNOV
Russian Academy of Sciences, Saint-Petersburg, RUSSIA; 0000-0003-3098-3346

PROF. Hab.PhD.Eng.Ionuț-Cristian SCURTU
MBN Academy, Constanta, ROMANIA; 0000-0003-3105-6384

Assoc. PROF. Doc. Dr. Sc. Sanjin VALČIĆ
University of Rijeka, CROATIA; 0000-0003-2950-9276

SCIENTIFIC BOARD

HOD Assoc. Prof. Docent Eng. Bohos APRAHAMIAN
Technical University of Varna, BULGARIA; 0000-0003-3595-1861

PROF.Mahmoud El-Sayed El- BAWAB
Arab Academy for Science Technology and Maritime Transport, EGYPT; 0000-0001-7391-7512

PROF. PhD. Florina BUCUR
Military Technical Academy "Ferdinand I", Bucuresti, ROMANIA; 0000-0001-7574-8142

PhD. Milen DIMITROV
Black Sea Institute Burgas, BULGARIA; 0009-0003-6499-3742

Senior Lecturer Ec.Iunusova ELMAZ
Odessa National Maritime University, UKRAINE

M of Sc.,PhD. Ramiro G. ESCUDERO
Universidad Michoacana de San Nicolás de Hidalgo, México; 0000-0003-1635-8421

Dr. Captain Luis G. EVIDENTE
John B. Lacson Foundation Maritime University, PHILIPPINES

ASSOC. PROF. Mahmoud Reza HAGHDOUSTI
UK Higher Education Academy , Tehran, IRAN

ASSOC. Prof. PhD. Radu HANZU-PAZARA
Constanta Maritime University, ROMANIA; 0000-0002-9578-5263

Expert Vladimir KANEV
Sofia, BULGARIA

Doctor Tatiana KOVTUN
Odessa National Maritime University, UKRAINA; 0000-0002-2753-8519

PROF. PhD. Axel LUTTENBERGER
University of Rijeka, CROATIA

Prof. Dr. Valeriu LUNGU
Moldova Technical University, R.MOLDOVA

Creative Commons Attribution BY 4.0 International Licence (CC BY-4.0)

Journal of Marine
Technology and Environment
DOI: 10.53464/JMTE.02.2025

ISSN (Print): 1844-6116
ISSN (Online): 2501-8795
https://www. jmte.eu

PROF. PhD.Teresa J.LEO MENA
Universidad Politecnica de Madrid, SPAIN; 0000-0002-9610-1070

PROF. PhD. Irena MARKOVSKA
University "Prof.d-r Assen Zlatarov" Burgas, BULGARIA

Assist. Prof. PhD.Sabina NEDKOVA
University "Prof.d-r Assen Zlatarov" Burgas, BULGARIA; 0000-0002-4101-579X

ASSOC. Prof. PhD. Alexandra RAICU
Constanta Maritime University, ROMANIA; 0000-0002-2765-719

PROF.Ds. Serghei RUDENKO
Odessa National Maritime University, UKRAINE

Assoc. PROF. Habil. PhD. Eng. Liviu-Constantin STAN
Constanta Maritime University, ROMANIA ;0000-0002-4806-544X

PROF. Habil. PhD. Eng. Razvan TAMAS
Constanta Maritime University, ROMANIA;0000-0001-9253-6256

Lecturer Capt Emre UCAN
Dokuz Eylul University, TURKEY

Prof. PhD. Adam WEINTRIT
Gdynia Maritime University, POLAND; 0000-0002-3233-0966

EDITORIAL SECRETARY

- **Editorial assistants**

ASSOC. PROF. PhD. Eng. Nicoleta ACOMI
Constanta Maritime University, ROMANIA; 0000-0003-3564-6867

ASSOC. PROF. PhD. Eng. Mihaela-Luminita BARHALESCU
Constanta Maritime University , ROMANIA;0000-0002-6683-4353

Senior lecturer PhD. Eng. Ionut VOICU
Constanta Maritime University, ROMANIA; 0000-0001-7706-8378

ASSOC. Prof.Dr. ANCA SIRBU
Constanta Maritime University, ROMANIA; 0000-0001-7132-0595

- **Technical support**

ASSOC. Prof. PhD Catalin Silviu NUTU
Constanta Maritime University, ROMANIA; 0000-0001-7234-6869

- **Web Administrator**

Project Eng. Senior Graphic designer George POPESCU
Constanta Maritime University, ROMANIA

Creative Commons Attribution BY 4.0 International Licence (CC BY-4.0)

Journal of Marine
Technology and Environment
DOI: 10.53464/JMTE.01.2026

ISSN (Print): 1844-6116
ISSN (Online): 2501-8795
https://www. jmte.eu

JOURNAL ADDRESS

Journal of Marine Technology and Environment

Constanta Maritime University, 104, Mircea cel Batran Street, 900663, Constanta, Romania

Tel: +40 241 664 740/ 107

Fax: +40 241 617 260

E-mail: office@jmte.eu
https://jmte.eu/

NAUTICA PUBLISHING HOUSE CONSTANTA, ROMANIA

CONSTANTA MARITIME UNIVERSITY, 104, MIRCEA CEL BATRAN STREET, 900663, CONSTANTA, ROMANIA

EDITOR IN CHIEF – PROF. ENG. PANAITESCU MARIANA PHD. CONSTANTA MARITIME UNIVERSITY

email: mariana.panaitescu@cmu-edu.eu

Creative Commons Attribution BY 4.0 International Licence (CC BY-4.0)

CONTENTS

Journal of Marine
Technology and Environment
DOI:10.53464/JMTE.01.2026.01

ISSN (Print): 1844-6116
ISSN (Online): 2501-8795
https://www. jmte.eu

18 YEARS OF STORIES FOR JOURNAL OF MARINE TECHNOLOGY AND ENVIRONMENT – MORE MATURE, MORE DEDICATED

Mariana PANAITESCU [1], Fanel-Viorel PANAITESCU [2]

[1] Constanta Maritime University, Editor-in- Chief of Journal of Marine Technology and Environmental, Nautica Publish House, 104 Mircea cel Batran Street, 900663, Constanta, Romania, ORCID ID 0000-0002-8610-9554, e-mail address: mariana.panaitescu@cmu-edu.eu

[2] Constanta Maritime University, Faculty of Naval Electro-Mechanics, 104 Mircea cel Batran Street, 900663, Constanta, Romania,ORCID ID 0000-0002-2453-3384, e-mail address: viorel.panaitescu@cmu-edu.eu

Abstract :Journal of Marine Technology JMTE has come of age. This year, it's celebrating its 18th birthday! His journal has ISSN (Print): 1844-6116 ISSN (Online): 2501-8795 (from Volume 2/2016 to present). Number of articles published over the years: 2008, issue 1-14 articles; 2009-issue 1,15 articles; issue 2, 19 articles; 2010-issue 1,33 articles; issue 2-23 articles; 2011-issue 1,issue 2,17; 2012-issue 1,20; issue 2,13; 2013-issue 1,20; issue 2,16; 2014-issue 1,11; issue 2,13; 2015-issue 1,13; issue 2,13;l 2016-issue 1,11; issue 2,12; 2017-issue 1,11; issue 2,17; 2018-issue1,9; issue 2,6; 2020-issue 1,6; issue 2,8; 2021-issue 1,7; issue 2-11; 2022-issue 1, 12; issue 2, 10; 2023-issue 1,10; issue 2,14; 2024-issue 1,11; issue 2,9; 2025-issue 1,11; issue 2,9; 2025-issue 1,12; issue 2,11. From 2008 to 2015, the editor-in-chief was Associate Professor Feiza Memet, Ph.D., Eng., and from 2016 to the present, it has been Professor Mariana Panaitescu, Ph.D., Eng. Initially, the journal published a short abstract. Later, the full-length articles were published. Between 2013 and 2015, the journal was indexed in Copernicus (ICV 2013: 5.69; ICV 2015: 72.06). The Editorial team is currently working to index the journal in other internationally recognized databases. As of 2026, the journal is open access (Creative Commons Attribution 4.0 International License).

Key words : Continuity, dedication, environment, engineering, maturity, progress, technology.

1. INTRODUCTION

It feels like it was just yesterday1 A blank page, lots of enthusiasm, a carefully chosen name, and a burning desire to bring something new to the media landscape. Today, Journal of Marine Technology and Environment turns 18. We have reached the age of majority, a symbolic moment marking the transition from youthful exuberance to a mature, balanced, and, we hope, wise adulthood.

Eighteen years means over 450 issues, thousands of interviews, hundreds of field reports, and, most importantly, a relationship of trust built with you, our readers.

2. LOOKING BACK: A JOURNEY OF AUTHENTICITY

When we started in 2008 (for example), journalism looked different. We've weathered major technological shifts, economic crises, and times of social upheaval.

However Journal of Marine Technology and Environment (JMTE) has remained true to its core principle: "*The truth told responsibly*." We've been there to keep you accurately informed, to analyse, to be the voice of the community, and to uphold the values we believe in.

We fondly remember Volume 2 of 2016, when the journal also launched its online edition—the moment we truly understood the impact the written word can have.

3. WHO ARE WE AT 18?

Today, we want to believe that we are no longer just "the academic newspaper on the breakfast table." We are a multimedia platform, available on tablets, phones, and in the hearts of our readers through the two issues we publish each calendar year. We have grown together. We have undergone design changes and adapted to the public's new demands, but we have always maintained editorial rigor.

These 18 years have been possible thanks to a dedicated team, from the reviewers who leave their mark

Creative Commons Attribution BY 4.0 International Licence (CC BY-4.0)

Journal of Marine
Technology and Environment
DOI:10.53464/JMTE.01.2026.01
ISSN (Print): 1844-6116
ISSN (Online): 2501-8795
https://www. jmte.eu

by verifying and promoting quality articles, to the technical and marketing teams that ensure continuity.

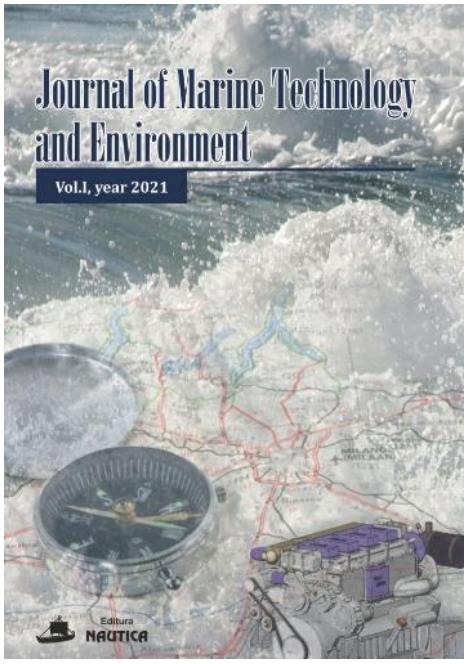

Figure 1 Journal of Marine Technology and Environment-Cover

JMTE has indexing CrossRef with DOI (10.53464) for each paper from 2021.

JMTE apply the Creative Commons Attribution BY 4.0 International Licence (CC BY-4.0) to all manuscripts to be published.

From 2008 to 2015, the Editor-in-chief was Associate Professor Feiza Memet, Ph.D., Eng., and from 2016 to the present, it has been Professor Mariana Panaitescu, Ph.D., Eng. The editorial team consists of internationally renowned experts who help enhance the journal's prestige and international visibility.

4. ACKNOWLEDGMENTS AND THE FUTURE

This milestone isn't just about us—it's about you. Thank you for your loyalty, for your messages—whether praise or criticism—and for letting us be a part of your lives.

What's next? Coming of age means responsibility. We are committed to improving quality, investing in in-depth investigations, and remaining a trusted source in a world full of fast-paced but often superficial information.

JMTE is turning 18. We're all grown up. We're ready for the next phase.

Happy birthday to us, happy birthday to you!

Creative Commons Attribution BY 4.0 International Licence (CC BY-4.0)

Journal of Marine
Technology and Environment
DOI:10.53464/JMTE.01.2026.02

ISSN (Print): 1844-6116
ISSN (Online): 2501-8795
https://www. jmte.eu

SIMPLIFIED MODELING AND SIMULATION OF RUDDER CONTROL FOR PARAMETRIC ROLLING REDUCTION IN SHIPS

Dumitru DELEANU[1]

[1] Constanta Maritime University, Faculty of Naval Electro-Mechanics, 104 Mircea cel Batran Street, 900663, Constanta, Romania, e-mail address: dumitrudeleanu@yahoo.com

Abstract: Parametric rolling is a resonance phenomenon affecting the safety and operational performance of ships, especially in head or following seas. This paper investigates the possibility of attenuation of parametric roll oscillations by using rudder-based stabilization. To this goal, the ship is represented as a single-degree of freedom oscillator with nonlinear damping and time-varying nonlinear stiffness, subjected to a proportional-derivative (PD) control applied via the rudder. Numerical simulations are performed to measure the influence of the main model parameters, including control gains, initial conditions, encounter wave frequency, on the ship response in roll. Results demonstrate that PD rudder control are able to reduce substantially roll amplitudes for an extensive range of operating conditions. The findings provide insight into the effectiveness of rudder-based control of ship rolling and can be used as a foundation for future research using more complex ship models.
Key words: parametric roll, rudder-based control.

1. INTRODUCTION

Parametric rolling is a nonlinear dynamic phenomenon commonly observed in ships navigating in head or following seas. The main reason for its triggering is the periodic variation of the ship's restoring moment and the result of its development consists in the appearance of excessive roll oscillations that can compromise crew safety and cargo integrity, especially if the wave encounter frequency is twice the ship natural frequency in roll and the wave and ship lengths are almost equal [1, 2].

Over the years, several techniques have been proposed to attenuate it. Passive systems, such as bilge keels or anti-roll tanks, provide limited effectiveness against high-frequency or parametric excitations. Active systems, including fin stabilizers and rudder-based roll stabilization, offer a more adaptable solution to varying sea conditions in real time [3 - 6].

The present study focuses on rudder roll stabilization (RRS), where the ship's rudder is used to generate a corrective roll torque [7, 8]. To this aim, the ship is modelled as a single-degree-of-freedom roll oscillator with nonlinear time-varying stiffness and damping and a proportional-derivative (PD) control is applied through the rudder to counteract roll oscillations.

The rest of the paper is organized as follows: Section 2 describes the mathematical model of the ship in rolling and the rudder-based control system. Section 3 presents the numerical results and the associated comments. Section 4 concludes with the main findings and highlights the potential directions for further research.

2. MATHEMATICAL MODELING

The governing equation used in the paper for describing the parametric roll oscillation of a ship take account of ship inertia, hydrodynamic nonlinear damping, a time-varying nonlinear restoring moment due to the periodic variation of metacentric height, and the moment generated by the rudder. Thus, it is written as:

$$(I_x + \delta I_x)\ddot{\theta} + d_1\dot{\theta} + d_2|\dot{\theta}|\dot{\theta} + \\ +\rho g \nabla (GM_m + GM_a cos\omega_e t)\theta + k_3\theta^3 = M_{rudder} \quad (1)$$

Here, θ is the roll angle, I_x and δI_x represent the ship and added mass inertia in roll, d_1 and d_2 stand for linear and quadratic roll damping coefficients, ρ is the water density, g the terrestrial gravitational acceleration, ∇ the ship displacement, k_3 the cubic coefficient of the nonlinear restoring moment, GM_m and GM_a are the constant and variable parts of the metacentric height, ω_e represents the wave encounter frequency, and M_{rudder} is the moment generated by the rudder control.

The last quantity is considered to be proportional with the applied rudder deflection δ,

$$M_{rudder} = k_r\,\delta \quad (2)$$

Creative Commons Attribution BY 4.0 International Licence (CC BY-4.0)

Journal of Marine
Technology and Environment
DOI:10.53464/JMTE.01.2026.02
ISSN (Print): 1844-6116
ISSN (Online): 2501-8795
https://www. jmte.eu

where k_r is a constant showing the effectiveness of the rudder in producing an anti-roll torque. The actuation of the rudder is provided by a servomechanism, so the control of the rudder is constrained by the properties of this system. The main constraints are the maximum rudder deflection, δ_{max}, the maximum rate of δ, $\dot{\delta}_{max}$, and the delay, T_δ, between the commanded control input δ_c and the actual angle of the rudder, δ. Usually, these constraints can be incorporated in a first-order differential equation of form:

$$T_\delta \cdot \dot{\delta} + \delta = \delta_c \tag{3}$$

with $|\delta| \leq \delta_{max}$ and $|\dot{\delta}| \leq \dot{\delta}_{max}$.

The rudder-based control is implemented using a proportional-derivative (PD) feedback law of form

$$\delta_c(t) = -\left(K_p\theta + K_d\dot{\theta}\right)/k_r \tag{4}$$

where K_p and K_d are the proportional and derivative gains. To tune these values, one can use either a manual adjustment or methods as Niegler - Nichols or Cohen-Coon [9].

3. RESULTS AND DISCUSSION

The nonlinear roll model described in the previous section was implemented in MATLAB using *ode45* solver. The running time was set to 400 seconds (with some exceptions) to ensure sufficient observation of the ship response to wave excitation and rudder-based PD control. The ship parameters, taken from experimental research, are presented in Table 1.

Table 1. The parameters involved in Equation (1)

Parameter	Value	Unit
$I_x + \delta I_x$	$1.6184 \cdot 10^{10}$	$kg \cdot m^2$
d_1	$3.2 \cdot 10^8$	$kg \cdot m^2/s$
d_2	$2.99 \cdot 10^8$	$kg \cdot m^2/rad$
k_3	$1.7844 \cdot 10^{10}$	$kg \cdot m^2/s^2 rad^2$
ρ	1000	kg/m^3
g	9.81	m/s^2
∇	76468	m^3
GM_m	1.91	m
GM_a	0.84	m
ω_e	0.592	rad/s

The ship natural frequency in roll is given by:

$$\omega_\theta = \sqrt{\frac{\rho g \nabla GM_m}{I_x + \delta I_x}} = 0.2975\ rad/s$$

such as $\omega_e/\omega_\theta = 1.99$.

3.1 Single – case dynamics

We first simulated the ship's behaviour in the absence of rudder control. As expected, approaching the resonance condition $\omega_e \approx 2\omega_\theta$ causes any initial disturbance to be greatly amplified. Figure 1 shows the time histories of ship roll angle, $\theta(t)$, the phase plane, $(\theta, \dot{\theta})$, and the ship energy in roll, $E(t) = \frac{1}{2} I_x \dot{\theta}^2 + \frac{1}{2} C_m \theta^2$, where $C_m = \rho g \nabla GM_m$. Even if the ship has good damping, the initial disturbance of 1^0, perhaps caused by a gust of wind or a wrong maneuver, is increased in about two minutes to 10^0, followed by a slow stabilization to the value of 8.3^0. For short time periods this level of rolling generally does not cause permanent damage, but noticeable discomfort for the crew is to be expected and the unsecured equipment may start to shift. A failure of one of the other existing damping systems (possible) would decrease the coefficients d_1 and d_3 values, which would lead to much higher roll angles (20^0 - 30^0) and, consequently, to a real danger to the integrity of the cargo and the safety of the crew [10].

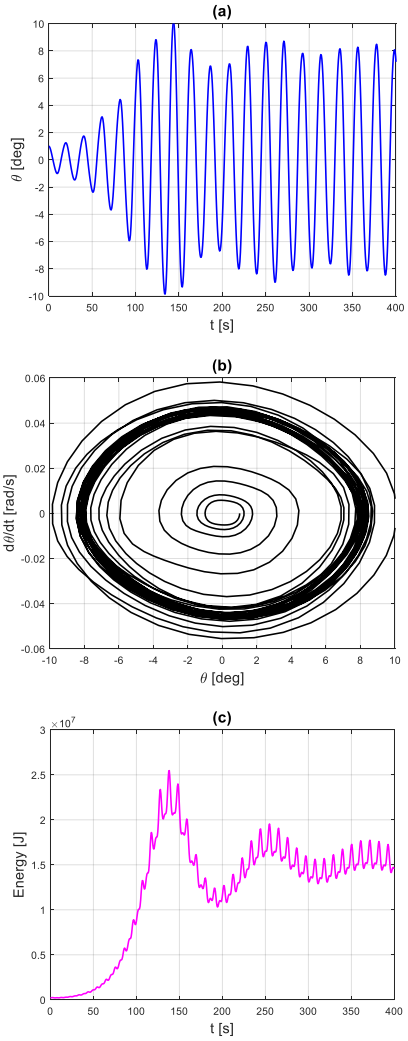

Creative Commons Attribution BY 4.0 International Licence (CC BY-4.0)

Journal of Marine
Technology and Environment
DOI:10.53464/JMTE.01.2026.02
ISSN (Print): 1844-6116
ISSN (Online): 2501-8795
https://www. jmte.eu

Figure 1 Ship behaviour in the absence of a rudder control: (a) Roll angle time histories; (b) Phase plane; (c) Ship energy.

Then, for cancel out or diminish this undesirable oscillation, the effectiveness of the PD rudder control strategy was evaluated.

The fixed values $k_r = 2 \cdot 10^8\ Nm/rad$, $T_\delta = 0.5\ s, \delta_{max} = 25^0$, $K_d = 10^8\ Nms/rad$ and variable gain K_p were chosen. Figures 2 and 3 present the roll angle, rudder angle and ship energy for $K_p = 2.5 \cdot 10^8\ Nm/rad$ and $K_p = 3.0 \cdot 10^8\ Nm/rad$, respectively.

In first case, the PD controller reduced the roll oscillation to 2.3^0. In the second one, we witness to a cancellation of the initial perturbation. The rudder angle δ followed the same trend as the roll angle θ and never exceeded 5^0.

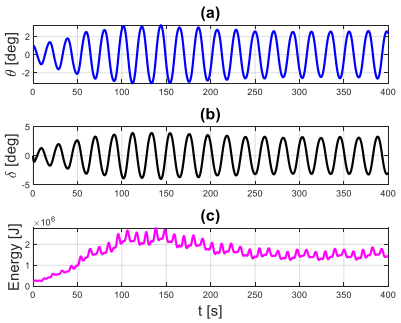

Figure 2 Dependence on time of the roll angle, rudder angle and ship energy for $K_p = 2.5 \cdot 10^8\ Nm/rad$

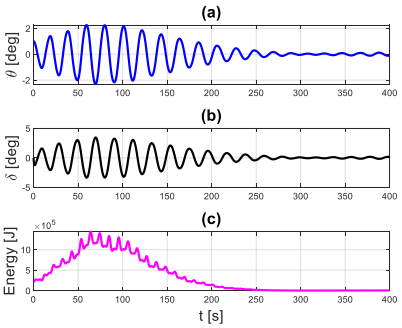

Figure 3 Dependence on time of the roll angle, rudder angle and ship energy for $K_p = 3.0 \cdot 10^8\ Nm/rad$

3.2 *Influence of control gains*

To give more insight about the influence of control gains K_p and K_d on the ship rolling, we make use of large-scale of them to generate two dimensional colormaps of maximum rolling and rudder amplitudes, and of final energy of ship rolling (see Figure 4).

For a fixed derivative gain K_d, increasing proportional gain K_p reduces the maximum amplitude of ship rolling in the stationary phase, $max|\theta|$ and, as consequence, the ship energy in roll. For a better separation of the plane (K_p, K_d) into areas with slower or faster stabilization of roll oscillations, representative coloured contour lines were used (e.g., $\theta_{max} = 2^0$).

The situation is somewhat different in the case of the rudder angle δ. It is possible in some cases that an increase in the parameter K_p will cause the actuator to saturate, i.e., exceed the value δ_{max}. This possibility shows that a careful tuning of PD gains is required to balance roll attenuation and physical limitations of the rudder system.

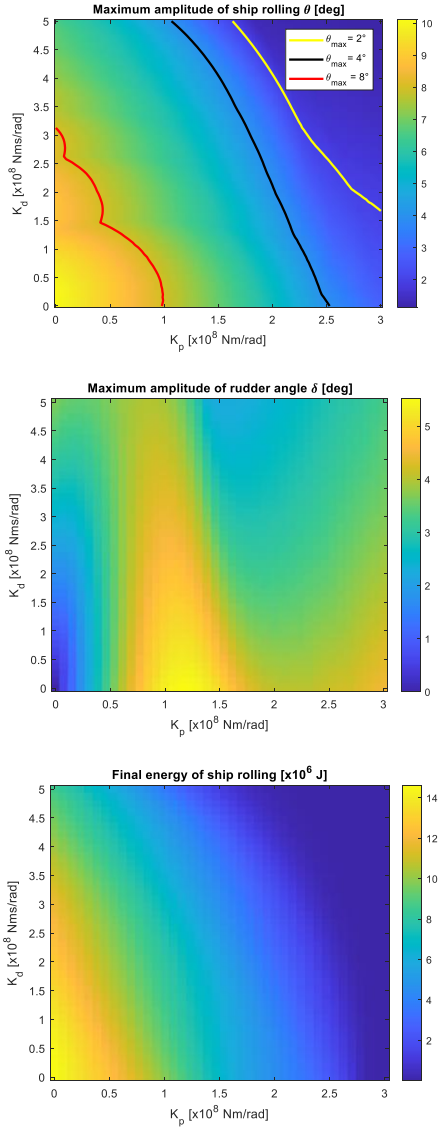

Figure 4 Colormaps for the maximum amplitudes of roll and rudder angles, and the ship's final energy in roll as functions of PD control gains

3.3 *Influence of initial conditions*

Roll amplitudes and rudder angles are strongly influenced by initial disturbances. With appropriate

Creative Commons Attribution BY 4.0 International Licence (CC BY-4.0)

Journal of Marine
Technology and Environment
DOI:10.53464/JMTE.01.2026.02
ISSN (Print): 1844-6116
ISSN (Online): 2501-8795
https://www. jmte.eu

control gains, small initial angles $\theta_0 = \theta(0)$ and rates $\dot{\theta}_0 = \dot{\theta}(0)$ result in a rapid ship stabilization and reduced rudder effort. Large disturbances θ_0 and $\dot{\theta}_0$ will maintain the dangerous oscillation for a long period of time, no matter the control gains values.

As Figures 1 and 2 demonstrate, parametric roll develops rapidly in the first 50 - 100 seconds, both in the absence of control and in its presence. In this regard, Figure 5, made with the same inputs as Figure 3, presents colormaps for the dependencies of maximum roll and rudder angles in the first 100 seconds on initial conditions. In the area associated with high θ_0 values, the rudder is seriously stressed and rudder constraint $\delta = \delta_{max}$ is reached.

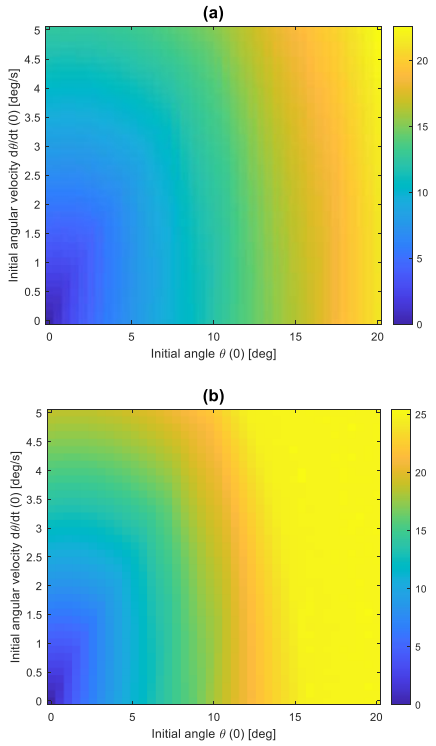

Figure 5 Colormaps for the maximum amplitudes of roll (a) and rudder (b) angles as functions of initial disturbances in the first 100 seconds of simulation

For long term, the robustness of rudder – based PD control succeed to mitigate the roll oscillation. Figure 6 shows the maximum roll angle in the last 50 seconds (from 400) for different $(\theta_0,\ \dot{\theta}_0)$ and K_p. The other parameters were kept unchanged. A consistent reduction, towards more than acceptable limits, of the roll amplitudes can be observed across the entire range of ICs tested. The most interesting aspect in this simulation is the placement of the roll amplitudes on the strips.

3.4 Roll played by encounter wave frequency

Parametric excitation due to waves can induce resonance, leading to increased roll amplitudes, even in the presence of a rudder control. Figures 7*a* and *b* present angle θ_{max} as a function of wave encounter frequency ω_e for a fixed initial perturbation $(\theta_0 = 1^0, \dot{\theta}_0 = 0^0/s)$ in the first 100 s, respectively last 50 s from 400 s. The results prove that the PD rudder control effectively cancel this small disturbance across the entire frequency range with some exceptions. High amplitudes are observed near the resonance frequency $\omega_e \approx 2\omega_\theta$ even for controlled rudder. For the chosen values of the gain K_p and fixed K_d, only a shifting toward right of the curve $\theta_{max}(\omega_e)$ is observed. This emphasizes the great importance of appropriately tuned control gains to ensure a robust performance under parametric excitation.

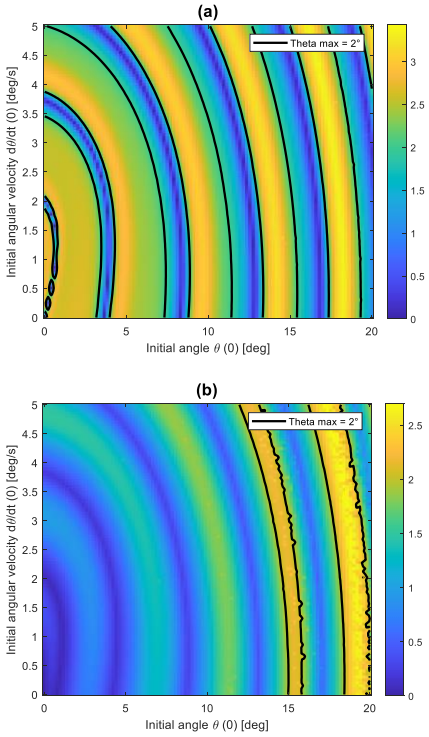

Figure 6 Colormaps for the maximum amplitudes of roll angle as functions of initial disturbances in the last 50 seconds of simulation (from 400).
(a) $K_p = 2.5 \cdot 10^8 Nm/rad$;
(b) $K_p = 3.0 \cdot 10^8\ Nm/rad$

The shift towards higher values of the frequency ω_e with the increase of the gain K_p is illustrated in figure 7*c*. It is obvious that only a reconsideration of K_p will produce an exit from the area of large stationary amplitudes.

Figure 7*b* highlights a potentially dangerous frequency range in the case of controlled rudder, located around the value $\omega_e \approx 0.65$. To investigate the control efficiency in this band, Figure 7*d* shows the angle θ_{max} as a function of the two gains for $\omega_e = 0.67$. In this variant, only values of K_p below $10^8 Nm/rad$ will ensure a decay of the oscillation.

Creative Commons Attribution BY 4.0 International Licence (CC BY-4.0)

Journal of Marine
Technology and Environment
DOI:10.53464/JMTE.01.2026.02
ISSN (Print): 1844-6116
ISSN (Online): 2501-8795
https://www. jmte.eu

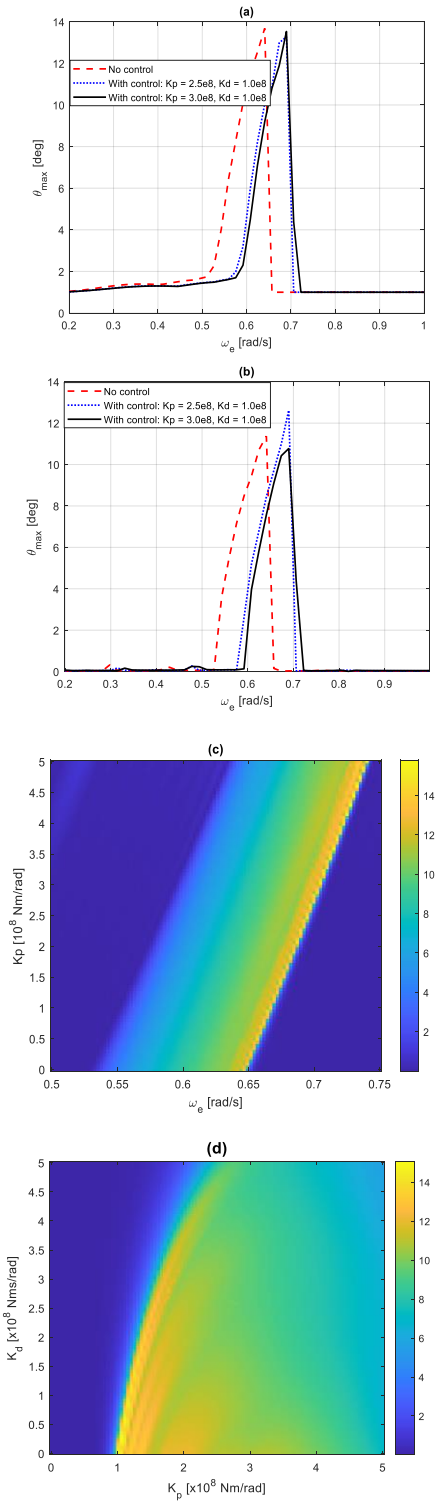

Figure 7 Maximum roll amplitude in the first 100 seconds (a) and in the last 50 s from 400 s (b) as a function of wave encounter frequency; Colormap showing θ_{max} in the last 50 s as a function of ω_e and K_p (c) or K_p and K_d for $\omega_e = 0.67$ (d)

3.5 *Influence of an irregular sea*

A real wave is generally very different from a sinusoidal one. As a first step towards an irregular wave, we will replace the constant part of the time-varying restoring moment, C_m, by the slowly varying term $C_m(1 + 0.3 \sin 0.05\,\pi t)$. The rest of the parameters coincide with those used in creating Figure 6. In addition to a slight increase in the amplitude of the steady state, a deviation from the parallelism of the contour lines is also observed in the right area. It is expected that a stochastic wave model will substantially affect the appearance of these colormaps.

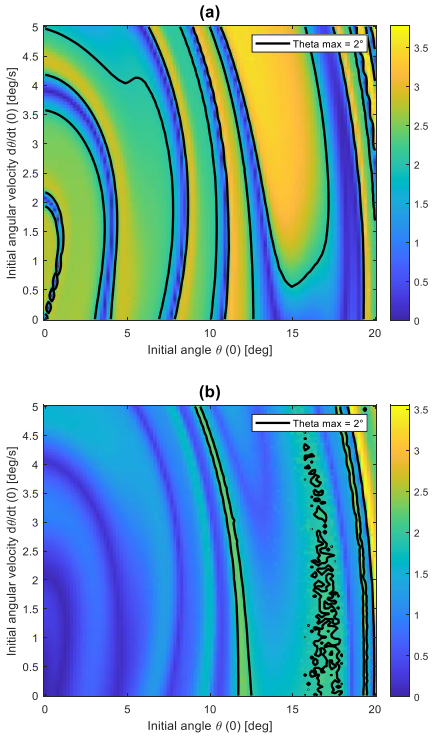

Figure 8 The same as in Figure 6 but for C_m replaced by $C_m(1 + 0.3 \sin 0.05\,\pi t)$

3.6 *Settling time analysis*

In this section, by settling time we understand the time required for $|\theta(t)|$ to remain permanently below a threshold of 1^0.

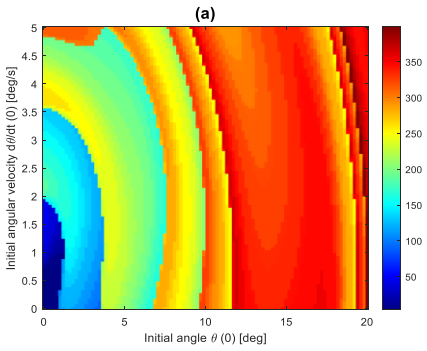

Creative Commons Attribution BY 4.0 International Licence (CC BY-4.0)

Journal of Marine
Technology and Environment
DOI:10.53464/JMTE.01.2026.02
ISSN (Print): 1844-6116
ISSN (Online): 2501-8795
https://www. jmte.eu

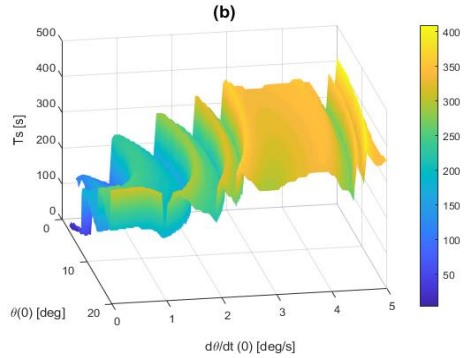

Figure 9 Two (a) and three (b) colormap describing the settling time T_S as a function of initial conditions

Figure 9 presents two and three dimensional colormaps of the settling time T_S (in seconds) for different combinations $(\theta_0, \dot{\theta}_0)$ and $\omega_e = 0.592$. The simulation confirms that low initial disturbances lead to short settling times (< 100 s), moderate disturbances. result in settling times up to 150 s, while severe initial perturbations require hundreds of seconds for stabilization (if it really happens for the combination chosen for control gains).

4. CONCLUSIONS

The present study investigated the attenuation of parametric roll oscillations in ships using rudder-based proportional-derivative (PD) control. The main findings are summarized as follows:

i) The PD rudder controller effectivelly succeded to diminish or vanish roll amplitudes across a wide range of wave frequencies and initial conditions both in regular or irregular-like seas;
ii) Roll amplitudes and settling times are strongly dependent on initial perturbations. Small initial roll angles and rates result in a rapid stabilization, while large perturbations cannot be attenuated regardless the control gains or require long settling times;
iii) The wave excitation is dangerous only in the proximity of resonance. A suitable choice of control gains will produce a shift of the frequency-response curve and, as consequence, an exit from the high amplitudes region;
iv) Despite the model's simplifications, the study provides valuable information about rudder-based stabilization of ship rolling.

Future work may include extensions of the model to multi-degree-of-freedom systems, incorporate more nonlinear features and stochastic wave spectra, and/or experiments to validate the numerical predictions.

5. Credit Author Statement

Conceptualization: D.D.

Data curation: D.D.

Formal analysis: D.D.

Funding acquisition: D.D.

Investigation: D.D.

Methodology: D.D.

Project administration: D.D.

Resources: D.D.

Software: D.D.

Supervision: D.D.

Validation: D.D.

Visualization: D.D.

Writing – original draft: D.D.

Writing – review & editing: D.D.

6. REFERENCES

[1] Ikeda, Y., Ouchi, T., 2008, *Parametric rolling in head seas: Mechanisms and countermeasures*, Journal of Marine Science and Technology, Vol.13, no.2, pp. 123 - 136.

[2] Pauling, J.R., 2011, *Parametric rolling on ships: then and now. Contemporary ideas on ship stability and capsizing in waves*, Fluid Mechanics and its Applications, Vol. 97, pp. 253 - 266.

[3] Novac, I., Faitar, C., 2016, *Consideration upon fixed anti-rolling passive systems*, „Mircea cel Batran Naval Academy" Scientific Bulletin, Vol. 19, no. 2, pp. 260 – 266.

[4] Larsson, L., Stern, F., 2013, *Roll stabilization of ships: A review of active and passive methods*, Journal of Ship Research, Vol. 57, no. 3, pp. 190 – 204.

[5] Larsson, L., Ory, F., 2017, *Analysis of parametric roll resonance and mitigation using active control systems*, Applied Ocean Research, Vol. 63, pp. 1 – 12.

Creative Commons Attribution BY 4.0 International Licence (CC BY-4.0)

Journal of Marine
Technology and Environment
DOI:10.53464/JMTE.01.2026.02
ISSN (Print): 1844-6116
ISSN (Online): 2501-8795
https://www. jmte.eu

[6] Liu, B., 2023, *Study of modern ship stabilizer technology*, Highlights in Science, Engineering and Technology, Vol. 72, pp. 788 – 792.

[7] Grue, J., Faltinsen, O.M., 2001, *Rudder-induced roll control in ships under parametric excitation*, Ocean Engineering, Vol. 28, no. 11, pp. 1303 – 1320.

[8] Von Amerengen, J., Van der Klugt, P.G., Van Nauta Lemke, H.R., 1990, *Rudder roll stabilization for ships*, Automatica, Vol. 26, no. 4, pp. 679 – 690.

[9] Tagnacca, S., D'Ambrosio, F., 2015, *PD control of ship roll: Simulation and optimization*, Journal of Marine Science and Application, Vol. 14, no. 2, pp. 102 – 112.

[10] Deleanu, D., Dumitrache, C.L., 2019, *Numerical study of a container ship model for the uncoupled parametric rolling*, IOP Conference Series: Materials Science and Engineering, **591**012106.

Creative Commons Attribution BY 4.0 International Licence (CC BY-4.0)

Journal of Marine
Technology and Environment
DOI:10.53464/JMTE.01.2026.03

ISSN (Print): 1844-6116
ISSN (Online): 2501-8795
https://www. jmte.eu

GREENING THE OPERATION OF THE ARLEIGH BURKE-CLASS (DDG-51) VESSEL UNDER CLIMATE CHANGE SCENARIOS: A COST AND EMISSIONS PERSPECTIVE

A. DESHPANDE[1]

[1]U. Strathclyde, Glasgow, UK, G40GE, e-mail addeshpa@gmail.com

Abstract: Since its inception in 1991, the DDG-51 naval class vessel continues to be a workhorse for the US Navy. In the coming three decades, naval performance is expected to be influenced by climate change. We would like to investigate whether the current marine diesel run vessel will benefit from retrofitting any other technology to tackle climate change impact and contribute to a greener operation. We argue that substituting diesel with methane gas while retrofitting with air lubrication can indeed lend help to this effort. More technically, drawing inspiration from maritime logistics, we arrive at our conclusion that the conventional diesel run DDG-51 naval vessel with air lubrication will offer similar CO_2 per ton nautical mile emissions and related costs per ton nautical mile like the environmentally better methane gas fuel run without air lubrication. We thus conclude that the methane gas run vessel with air lubrication is better than diesel run vessel with air lubrication. This conclusion is shown to be valid via a climate scenario projection for three decades into the future.

Key words: Air lubrication, Arleigh Burke-class (DDG-51), cost and emissions per ton-nautical mile, retrofitting**.**

1. INTRODUCTION

In commercial shipping, LNG powered ships are being encouraged as a means to provide reduced carbon footprint of maritime vessel operations [13]. This process is termed as "Greening". From a naval perspective, greening operation has recently been given serious thought. The US navy plans to achieve net zero carbon emissions by 2050 [14]. The Arleigh Burke-class (DDG-51) has appeared to be representative of the wider fleet of conventional fuel driven vessels of the US Navy [7]. The present work of ours investigates greening operation on the same. More precisely, in this article we study impact of climate change on its operation with regards to emissions and costs for three decades starting from the year 2025. We then recommend technologies for its greening objective. For this analysis, we choose a strategically important travel path for the vessel. Hence the vessel is assumed to travel from Florida to Chagos island with a distance of around 7000 nautical mile (nm). It traverses though Atlantic, Southern and the Indian ocean. Distance traversed one way from Florida to Chagos island is divided into following three sections (Table 1):

Table 1. Ocean routes

Ocean route	Distance (nm)
Florida to North of Southern Ocean	6000
North of Southern Ocean to Madagascar	200
Madagascar to Chagos island	1400

Like any other oceans, these oceans have been thought to be impacted adversely by the climate change. The IPCC report [8] leads us to the following conclusion on the sea states with regards to sea surface temperature, salinity and wave heights (Table 2):

Table 2. Projections of climate variables

Ocean	Salinity	Sea Surface temperature	Wave height
North Atlantic	↑↔	↖↑	↓↑
South Atlantic	↑↔	↖↑	Null

Creative Commons Attribution BY 4.0 International Licence (CC BY-4.0)

Journal of Marine
Technology and Environment
DOI:10.53464/JMTE.01.2026.03
ISSN (Print): 1844-6116
ISSN (Online): 2501-8795
https://www. jmte.eu

Southern	↓↔	↑↑	↑↑
Indian	Null	Null	Null

We read the table in the following way: the IPCC concludes that for the South Atlantic Ocean, it has high confidence (up arrow) that the sea surface temperature will be increasing in a non-decreasing way (north west arrow). For the Southern Ocean, one has medium confidence (left right arrow) that the salinity will decrease (down arrow). For Indian ocean there is no discussion on salinity. We can similarly read the other entries of the above table. We translate these projections into numbers for various sea states drawn from the IPCC reports [9] which we now describe.

South Atlantic Ocean is assumed to have the following projected growth in temperature, density and viscosity of ocean water (Table 3).

Table 3. South Atlantic climate projections

Climate variables	2025-2035	2036-2045	2046-2056
Temperature(F)	75.15	75.28	75.42
Viscosity $(ft^2/s)\times10^5$	1.0392	1.033	1.030
Density $(lb\text{-}s/ft^4)$	1.986	1.9859	1.9858

Southern Ocean is assumed to have the following projected growth in temperature, density and viscosity of ocean water (Table 4):

Table 4. South Ocean climate projections

Climate variables	2025-2035	2036-2045	2046-2056
Temperature(F)	69.86	69.72	69.58
Viscosity $(ft^2/s)\times10^5$	1.0519	1.055	1.060
Density $(lb\text{-}s/ft^4)$	1.986	1.9859	1.9858

Indian ocean is assumed to have the following projected growth in temperature, density and viscosity of ocean water.

Table 5. Indian Ocean climate projections

Climate variables	2025-2035	2036-2045	2046-2056
Temperature(F)	75.50	75.80	76.10
Viscosity $(ft^2/s)\times10^5$	1.030	1.028	1.020
Density $(lb\text{-}s/ft^4)$	1.986	1.9859	1.9858

To understand the comparative futuristic values of the wave height we investigate the literature on the same and synopsize it in the Table 9 in appendix.

Based on those, we assume the following values of sea states with regard to the wave height for the following oceans (Table 6):

Table 6. Wave heights

Oceans	2025-2035 (m)	2036-2045 (m)	2046-2055 (m)
S. Atlantic	10	8	7
Southern	7	8	10
Indian	8	8	8

Having the above climate data in mind, we set further to analyze its impact. The article is organized as follows. In the next section, we tabulate the key characteristics of the DDG-51 class destroyer. The statistics of the cost per ton mile and emissions as a function of total hull resistance that the vessel will encounter while at sea will be described. In the third section, we present the output. In the fourth section, we present the deductions from the output. In section 5, the appendix refreshes vessel performance preliminaries useful for understanding naval performance modeling. As expected, this material is fairly standard, and we have borrowed it from the lecture notes on Ship performance taught at US Naval Post Graduate School [11]. An algorithm to calculate the total hull resistance is mentioned at the end.

2. THE DDG-51 CLASS DESTROYER

The Arleigh Burke class destroyer (DDG-51) put into operations on 4th July 1991, is a representative of US navy fleet [7]. Its dimension is below

Table 7. The DDG-51 characteristics

Characteristics	Dimensions
Waterline length (L_s)	142 m
Beam (B_s)	18 ft
Draft, T_s	6.4 m
Wetted Hull Area ,(S_s)	3001 m^2
Displacement, Δ_s	8768 metric tons
DWT	8373 tons
Propeller diameter (D_0)	18 m
Fuel	F-76 diesel fuel
Fuel carbon factor (K_F)	12.2 g CO_2e/MJ

The DDG-51 is powered by four General Electric LM2500 gas-turbine engines which can produce 80000

Creative Commons Attribution BY 4.0 International Licence (CC BY-4.0)

Journal of Marine Technology and Environment
DOI:10.53464/JMTE.01.2026.03
ISSN (Print): 1844-6116
ISSN (Online): 2501-8795
https://www. jmte.eu

kW in shaft power. For cruising speed of 15 knots only, single engine powers a single shaft while other engines are idle. In full power mode, all engines are operational and can steam a ship at 30 knots.

The LM2500 is assumed to run on marine diesel. A methane gas run dual engine is also available. Characteristics of these fuels viz. carbon factor (C_F), specific fuel consumption (SFC) and assumed costs are (Table 8)

Table 8. Fuel characteristics

Fuel	C_F	SFC(g/kwh)	Cost in USD per ton
Marine diesel	3.206	200	700
Methane	2.750	200	781

The cost of fuel is assumed to be constant throughout the three decades. We make this assumption to understand the cost runs solely as a function of climate variables rather than via inflationary adjustment on fuel cost.

2.1 Assumptions

1. We ignore the impact of fouling. This is in fact known to significantly corrode the hull leading to frequent maintenance. However, for our focus on operational cost and emissions, this may be ignored.
2. We nullify the impact of slow steaming by assuming constant velocity throughout the journey of the vessel.
3. Turbo sails, Flettner rotor, Towing kite and Ship lengthening aren't feasible carbon reduction strategies for the DDG-51 owing to the latter's military application.

Thus, we are left to focus on the air-lubrication technology and it impact on carbon emission and cost to run. Similarly, fuel-wise, we are limited to the current available feasible engines that run either on marine diesel and methane gas. Hence, we can rule out other possible fuels even though they may be creating low carbon foot print.

A modified formula from [4] of CO_2 emitted per ton nautical mile
(e_{V_i}) is given by

$$e_{V_i} = \frac{1}{DM}\sum_{i=0}^{n}\frac{D_i}{V_i} * SFC * P_i * K_F \qquad (1)$$

where the factor $\frac{1}{DM}$ transforms the cost per voyage to a cost per ton nautical mile for which D which is the voyage distance and M is ``light displacement,'' and has a assumed value of 2000 ton. The sectoral factor $\frac{D_i}{V_i}$ gives the hours in each ocean section of the voyage for velocity V_i. P_i=R_T for section i is the total hull resistance and K_F is the carbon factor in (t- CO_2/t-Fuel). Here we have n=3 sections.The cost of fuel burnt in this voyage is likewise calculated by

$$c_{V_i} = \frac{1}{DM}\sum_{i=0}^{n}\frac{D_i}{V_i} * SFC * P_i * C_{Fuel} \qquad (2)$$

An algorithm to calculate the Total hull resistance P_i has been described in the appendix. From the SFC values in the Table 8 and equations (1), it is apparent that the emissions from Marine diesel will be about $\frac{3.206\text{-}2.75}{2.75}*100 \approx 17\%$ higher than that of methane. If air lubrication is involved, it is expected that the total hull resistance will be reduced by about 10-20% [5][6]. Hence if climate change does not grossly impact operability of the DDG-51 for coming three decades, then diesel run engines retrofitted with air lubrication will result in a performance similar to the expensive Methane gas run operation. Further, if we were to substitute fully the diesel operation with methane and air lubrication; though expensive than diesel, we achieve approximately twice the reduction in emission than the conventional diesel run without air lubrication. This is in line with the US State department's initiative to invest in upgrading technology to battle greenhouse gas emissions [1]. Hence, it is imperative to understand the performance of the vessel with respect to cost and emissions under climate change for various vessel speeds. If these don't vary much for each speed, then our observation that conventional diesel run vessel with air lubrication will provide similar performance to costly methane gas-run vessel without air lubrication will get validated.

3. RESULTS

Throughout this section, speeds range from 5 knots to 20 knots with increment of 5 knots on Y axis. For marine diesel run engines we have, emissions $e_5, e_{10}, \ldots, e_{20}$ in CO_2 emitted per ton nautical mile and cost $c_5, \ldots, c_{20}$ in USD for corresponding vessel speeds on X axes of the below two charts respectively (Figure 1, Figure 2).

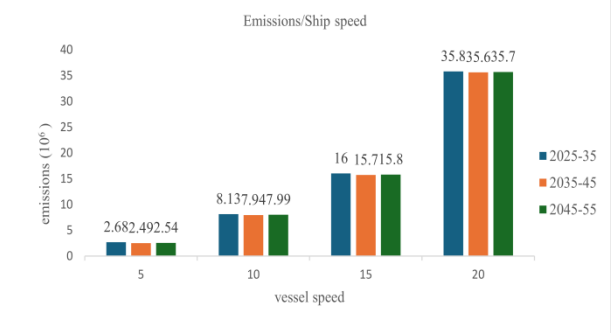

Creative Commons Attribution BY 4.0 International Licence (CC BY-4.0)

Journal of Marine
Technology and Environment
DOI:10.53464/JMTE.01.2026.03
ISSN (Print): 1844-6116
ISSN (Online): 2501-8795
https://www. jmte.eu

Figure 1 Emissions/speed

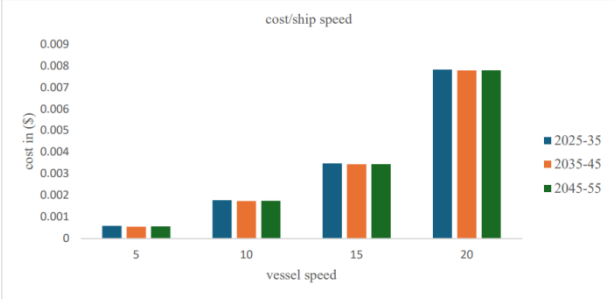

Figure 2 Costs/speed

3.1 Observations

1. The total hull resistance has a very large value in contrast to the energy added by the term describing the square of the wave heights in equation (7).
2. From the Figure 1 and 2 on cost and emissions for DDG 51 respectively, we observe that there is only slight variation between emissions and costs over three decades for a fixed speed ranging from 5 knots till 20 knots even under climate change. In fact, there is a slight decreasing trend. Though it may seem surprising at first, we can deduct from the total hull resistance equation (7) being quadratic in ship speed when inputted in to the cost and the emissions formula (1-2), which upon division by ship speed V_i in section i; results in an expression consisting of being weighted linear in ship speed. Since over time, climate change impacts for worse, the vessel expectedly will travel at a similar or lesser than assumed speed with non-increasing weight multiplier like here thus producing similar or close to decreasing emissions and costs. However, this observation does not preclude the fact that from the perspective of naval operations, the vessel will take a hit in the form of disruptions as climate change worsens [3].
3. As speed increases, costs and emissions increase. The difference is rather large. For example, emissions and costs rise by 1400% between speeds of 5 knots and 25 knots. However, for military applications, slow steaming is not always feasible. Hence, we need to focus on retrofitting the vessel with green technology.

4. CONCLUSIONS

1. We conclude that the DDG-51 operation is spectacularly green if it performs slow steaming. However, strategically speaking, slow steaming is not expected. On the other hand, effective air lubrication is known to reduce the power consumption by around 10-20%. Since no other green technology like Towing kite, solar panels, wind energy harnessing, ship lengthening is feasible in a retrofit, we can conclude that air lubrication is a feasible green technology for the DDG-51.
2. The projected climate change does not impact the cost or emission per ton-nm performance of DDG-51. Hence the diesel run engines with the vessel retrofitted with air lubrication will result in a performance similar to the expensive Methane gas run operation without air lubrication. Methane gas run vessel with effective air lubrication of course leads to green and cost comparative running vis a vis the diesel run engine.

5. APPENDIX

5.1 Vessel performance preliminaries

Ships performance is solely impacted by the resistance it faces to its hull. The total hull resistance is written as

$$R_T=R_v+R_w+R_a \tag{3}$$

where R_v is viscous (friction) resistance, R_w is wave making resistance and R_a is air resistance caused by ship moving in calm air. We rewrite this equation in terms of dimensionless constants as $C_T=C_v+C_w$ where C_T is total hull resistance, C_v is viscous (friction resistance and C_w is wave making resistance. We note here that here there is no air making resistance in dimensionless form. Since the total hull resistance is a function of hull form, ship speed, and the water properties, the coefficients of total hull resistance is also a function of these and given by

$$C_T=\frac{R_T}{\frac{1}{2}\rho S V^2} \tag{4}$$

where ρ is density of water in (lb-s^2/ft^4), S is wetted surface area of the underwater hull (ft^2) , V is velocity (ft/s). We elaborate on the various dimensionless coefficients further.

5.2 Wave making resistance

As Ships traverse, they create waves which in turn ``drag" the ship by its resistance. As ship speed increases, the height of the waves produced increases and therefore the energy required to produce these waves increases. From the wave theory, the length of a free wave on the surface is related to velocity as follows:

$$L_w=\frac{2\pi V_s^2}{g} \tag{5}$$

where L_w is wave length (ft), V_s is ship velocity (ft/s) and g is acceleration due to gravity ft/s^2.
We have $V_s\approx 1.212\sqrt{L_w}$. The speed where wavelength equals ship length can be solved for in the above equations and is given by

$$V_s=1.34\sqrt{L_s}\left(kt/\sqrt{ft}\right) \tag{6}$$

where V_s is ship speed in knots and
L_s is ship length (ft). This is called as hull speed rule of thumb. Hence, we have $L_w\approx 1.22\,L_s$. When wavelength L_w is close to L_s the hull speed is the least efficient speed

Creative Commons Attribution BY 4.0 International Licence (CC BY-4.0)

Journal of Marine Technology and Environment
DOI:10.53464/JMTE.01.2026.03
ISSN (Print): 1844-6116
ISSN (Online): 2501-8795
https://www. jmte.eu

for displacement of ship. Likewise, if $L_w=1.5L_s$, hull speed is the worst speed to operate at. From above equations it is obvious that increase in ship speed increases R_T. From wave theory, energy in a wave is proportional to the wave height. This if wave height increases wave making resistance becomes dominant. Hence $R_w=L_s+H^2$. Since L_s is given constant, we can assume that $R_w \approx H^2$.

5.2 Air resistance (R_a)

Air resistance is the resistance caused by the flow of air over the ship with no wind present. This component of resistance is affected by the shape of the ship above the waterline, the area of the ship exposed to the air, and the ships speed through the water. Resistance due to air typically are 4-8% of total ship resistance but may be as high as 10% for aircraft carriers. Hence, we can safely assume that $R_a=0.1R_T$. Hence

$$R_T=R_v+R_w+R_a$$
$$=R_v+H^2+0.1R_T$$
$$=\frac{C_v*\frac{1}{2}\rho V_s^2*S+H^2}{0.9} \quad (7)$$

Here C_v is affected by hull form, speed and water properties as before. C_v takes into account the friction of the water on the ship as well as the influence of hull form on the viscous pressure drag $C_v=C_F+KC_F$ where C_F is tangential component of viscous resistance; KC_F is normal viscous pressure drag component of viscous resistance. The skin friction coefficient given below is based on the assumption that the hull is a flat plate moving through the water and is a function of Reynolds number (ship speed, its length and kinematic viscosity). The form factor K accounts for the effect of hull form on viscous resistance. Both the skin friction coefficient and the form factor equation are empirically derived from many tests on the flat plates and ships.

$$C_F=\frac{0.075}{[\log_{10}(L_S V_S/v)^{-2}]} \quad (8)$$

$$K\approx 19\times\left(\frac{\nabla}{L_s^2\times T}\right)^2 \quad (9)$$

We further complete our discussion on power shaft calculation by defining the thrust T as

$$T=\frac{1}{2}\rho A_0 V_A^2 * A_F \quad (10)$$

where A_0 is propeller disc area, V_A is speed of advance given by $V_A=V_S-V_W$ i.e. ship speed minus the wave speed. A_F is the axial flow factor given by $2b+b^2$. Below is the algorithm to calculate the total hull resistance.

Algorithm:

1. From ideal propulsion efficiency η_I calculate b via $\eta_I=\frac{2}{(1+(1+b))}$
2. Decide the wave velocity V_W . $V_A=V_S-V_W$
3. A_0 is obtained via the propeller diameter.
4. $\nabla=\frac{Displacement}{(waterdensity*g)}$
5. $K\approx 19\times\left(\frac{\nabla}{L_s^2\times T}\right)^2$
6. $C_v=C_F+KC_F$.
7. $S=\nabla^{2/3}\times\left(3.4+\frac{L_s}{2\times\nabla^{1/3}}\right)$ is wetted surface area.
8. Hence calculate R_T.

Table 9. Wave height predictions

Ocean	Unit	Values till 2100 References
Southern	Annual Mean wave height (AMWH)	5-10% (5-8%) rise Ref. [10], [12], [2]
South Pacific	AMWH[Annual Extreme wave height (AEWH)]	5-10% (5-8%) rise Ref. [10], [12], [2]
N. Atlantic/ Mediterranean	AMWH	Up to 10% decrease Ref. [10],[2]
N. Pacific	AMWH	Up to 10% decrease Ref. [10],[2]
S. Atlantic	AMWH[AEWH]	0-20% [5-8%] rise Ref. [12],[2]
Indian	AMWH[AEWH]	Upto 10% [5-8%] rise Ref. [12],[2]

6. CREdit authors statement

Conceptualization, Data curation, Formal analysis, Funding acquisition, Investigation, Methodology, Project administration, Resources, Software, Supervision, Validation, Visualization, Writing – original draft, Writing – review & editing:. A. D.

7. REFERENCES

[1] Breslin, D.A., 2008, *Climate change and the future of shipping and ship design*, Naval Engineers Journal. , Vol. 118, no.3

Creative Commons Attribution BY 4.0 International Licence (CC BY-4.0)

Journal of Marine
Technology and Environment
DOI:10.53464/JMTE.01.2026.03
ISSN (Print): 1844-6116
ISSN (Online): 2501-8795
https://www. jmte.eu

[2] Casas-Prat, M. Hemer, M.A., Dodet, G., Morin, J., Wang, X.L., Mori, N., Yough, I.,Erikson, L., Kamranzad, L., Kumar, P., Menendez, M., Feng, Y., 2024, *Wind-wave climate changes and their impacts*, Nature Reviews Earth and Environment, Vol. 5.

[3] https://theliquidgrid.com/climate-change-affects-the-navy/

[4] Lindstad, H., Asbjornslett, B.E., Jullumstro, E., 2013, *Assessment of profit,cost and emissions by varying speed as a function of sea conditions and freight market*, Transportation Research Part D, Vol. 19.

[5] Mäkiharju, S. A., Perlin, M., Ceccio, S.L., 2012, *On the energy economics of air lubrication drag reduction*, International Journal of Naval Architecture and Ocean Engineering, Vol. 4, no.4.

[6] Kantharia, R., 2021, *How Air Lubrication System for Ships Works?* https://www.marineinsight.com/green-shipping/how-air-lubrication-system-for-ships-work/

[7] Schultz, M.P., Bendick, J.A., Holm, E.R., Hertel,W.M., 2011, *Economic impact of biofouling on a naval surface ship*, Biofouling, Vol. 27, No. 1.

[8] https://www.ipcc.ch/data/

[9] https://www.ipcc.ch/synthesis-report/

[10] https://tinyurl.com/2t42ze3b

[11] https://www.usna.edu/NAOE/academics/en400.php

[12] https://tinyurl.com/mr22yrax

[13] Branza, G, 2023, *Green shipping. Study on regulations and sustainable options for decarbonization*, Journal of Marine Technology and Management, Vol. 2.

[14]https://www.navy.mil/Press-Office/Press-Releases/display-pressreleases/Article/3041221/department-of-the-navy-releases-climate-action-2030.

Creative Commons Attribution BY 4.0 International Licence (CC BY-4.0)

Journal of Marine
Technology and Environment
DOI:10.53464/JMTE.01.2026.04

ISSN (Print): 1844-6116
ISSN (Online): 2501-8795
https://www. jmte.eu

EFFECT OF CAVITATION EROSION OVER A NI-AL-BRONZE PROPELLER

George Ciprian IATAN[1], Adrian LUNGU[2]

[1] Transilvania University of Brasov, Materials Engineering and Welding Department, Eroilor Blvd., 29, 500036 Brasov, Romania; george.iatan@unitbv.ro
[2]"Dunarea de Jos" University of Galati, Department of Naval Architecture, 47 Domneasca Street, 800008 Galati, Romania, adrian.lungu@ugal.ro

Abstract: Commercial vessels with large deadweight capacity engaged in international voyages are generally powered by a single propeller. Hence, because the responsibility for developing the thrust force lays upon a single thrust component and redundancy cannot be ensured, a comprehensive evaluation for the operational conditions is to be carried out, as the propeller is closely related with the hydrodynamic seaworthiness of the vessel, which should precede any propulsion analysis, [1-2]. Despite the proven reliability of the nickel–aluminium-bronze alloy (NAB hereafter) used in its manufacturing, a marine propellers exposed to the risk of extended cavitation, the propeller is prone to localised wear and surface degradation. This is the reason of the present research aimed at is addressing the problematics of cavitation erosion of NAB propellers by employment of CFD investigation instruments. Cavitation occurrence is emphasised on a simplified three blades propeller together with hydrodynamic characteristics evaluation. Hence, the initiation of the cavitation on the blades surfaces is described together with a brief introduction of the most commonly used mitigation and recondition techniques of cavitation affected areas of propeller blades through modern methodologies.
Keyword: Cavitation erosion, CFD, NAB, propeller wear

1. INTRODUCTION

Throughout the International Maritime Organization (IMO) fundamental principles a key role is to perpetuate technical advancement of the components engaged in fuel efficiency of a maritime vessel, [1]. To accomplish that, a comprehensive analysis should focus not only on the propulsive equipment performances but also on a hull hydrodynamics introspection, [2-3].

It was Ene et al., who have proven in [4] that the key parameters of propulsion descriptors are the thrust force and the torque moment, as functions dependant of a series of parameters such as propeller diameter, blades number, hull interference thrust advance, pitch and propeller rotational speed. Although in its early design stage the propeller might seem to develop the necessary hydrodynamic performances, during the vessel operation, its overall efficiency becomes highly dependent on maintenance factors, such as close up examination for potential damage identification, periodic cleaning and polishing, [1].

A significant damage source which needs to be assessed is the cavitation erosion. The phenomenon of cavitation refers to phase discontinuities occurrence throughout the fluid flow, generated by pressure drops on the propeller blades. The unwanted influence of cavitation is not only affecting the efficiency of the propeller through a thrust breakdown, but also by the induced vibrations on the superstructure accommodation area which is usually positioned in the aft part of the ship.

It has already been proven that the cavitation risk can be avoided either by an efficient geometry design of the propeller through a proper design sustained either by comprehensive experimental tests performed in cavitation tunnels, or by numerical simulations of the local flow features by using the CFD techniques [5-6]. Under such circumstances, the design criteria of the propeller had to be addressed in the past years, such as the permanent challenges of increasing the propulsion efficiency be met.

While in the 20th century cavitation occurrence was avoided by increasing the blade area under the cost of reducing the revolution rate, the pursuit of keeping a reasonable cost imposed by the ship shareholders led to a limitation of the available measures for avoiding the cavitation occurrence. In such a context, it became commonly accepted to tolerate a certain level of cavitation on the propeller blades and hub within a strictly controlled level of noise on board, limited by international conventions, [6].

On the other hand, although the marine propeller is commonly manufactured from a complex alloy of nickel aluminium and bronze with proven good resistance at corrosion and erosion properties, once the cavitation phenomenon is occurring into a fluid containing erosive

Creative Commons Attribution BY 4.0 International Licence (CC BY-4.0)

Journal of Marine
Technology and Environment
DOI:10.53464/JMTE.01.2026.04
ISSN (Print): 1844-6116
ISSN (Online): 2501-8795
https://www. jmte.eu

particles, the synergistic effect of the cavitation on a surface may exceed the resistance threshold of the NAB alloy and the surface degradation is unavoidably initiated.

As mentioned above, analysing the behaviour of a propeller working in a cavitation regime, experimental tests on scaled propeller models in cavitation tunnels might be a proper choice in spite of their high costs. On the contrary, in such cases numerical predictions can be used to get accurate overall images of cavitation erosion areas at considerable lower costs, [7-8].

In response to the challenges of experimental cavitation assessment, a thorough instrument should be represented by a comprehensive numerical investigation through the computational fluid dynamics. Commonly known as an instrument highly dependent on the computational processing power, satisfactory outcomes may be available through the numerical solution of the Reynolds averaged Navier-Stokes (RANS) equations. Due to its capacity for using the averaging the turbulence close-up details, the methodology is decreasing the necessary CPU and computation time, [6].

2. MILESTONES OF THE CFD SETUP

Aimed at having a better description not only of the hydrodynamic performances of the propeller, but also of an accurate prediction of the cavitation mechanism, i.e. inception, development and extension, a CFD technique is proposed in the followings. A three-bladed propeller model of the DTMB 5415 ship is chosen to fit the purpose. The reason for choosing a 3 blades propeller was given by the limited computational resources, which eventually required a reasonable number of the discretisation cells.

The numerical simulation employs the ISIS-CFD solver of the Numeca Fine Marine software package. The very powerful numerical platform is regarded as one of the most reliable instruments for CFD analysis since it can solve the flow features by integrating the unsteady viscous free-surface flow equations accomplished by a wide variety of turbulence models. The partial differential equation set is iteratively solved within a given margin for the numerical errors. A sufficiently small step time is imposed such that the Courant number be below the unity. Meshing is performed such that a proper clustering be achieved on both leading and trailing edges, where the gradients of fluid pressure and velocity are expected to be significant. Consequently, a high discretization is also done in the intersection area of the boss with the blades, where violent separations are expected to develop. Due to the viscous friction, the speed drops to zero inside the boundary layer. This phenomenon does not occur linearly, but being described by a given low that defines the geometry of the velocity defect. The final mesh is depicted in Figure 1.

Table 1. Propeller particularities

Propeller diameter [m]	0.3
Advance speed [m/s]	3.0
Revolution rate [rpm]	1000

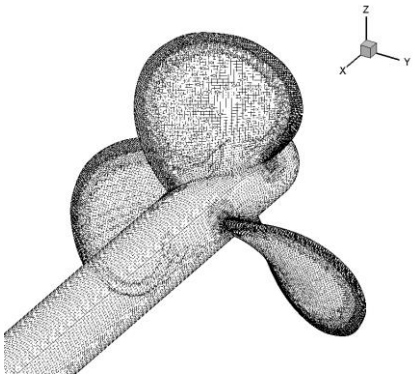

Figure 1 Isometric view of the geometry mesh

3. RESULTS AND DISCUTIONS

Three different simulations were performed for different revolution rates, under the hypothesis of constant axial flow speed. The advance coefficient defined as $J = v/nD$, where v is the advance speed, n is the propeller revolution rate and D is the propeller diameter, was calculated for each case, as tabulated in Table 2.

Table 2. Advance ratio coefficient values

Simulation	n [rpm]	J
1	900	0.666
2	1000	0.6
3	1100	0.545

Figures 2 (a) to (c) show not only a progressive increment of the pressure values, but also a decrease of the advance coefficient from 0.666 to 0.545. Obviously, the pressure gradients on the regions behind the leading edges are extending to the rest of the blade surface depending to the rotation increment from 900 rpm to 110 rpm, a fact that is confirmed by the physics. An increase of the loading for the blades is seen with the decrease of

Creative Commons Attribution BY 4.0 International Licence (CC BY-4.0)

Journal of Marine
Technology and Environment
DOI:10.53464/JMTE.01.2026.04
ISSN (Print): 1844-6116
ISSN (Online): 2501-8795
https://www. jmte.eu

the advance coefficient, when the propeller is not heavy loaded. On the other hand, Figure 2 (d)…(f) clearly shows a pressure drop on the suction side of the running edge, marked with blue. Hence, the pressure difference between the suction side and the pressure side of the blades increases with the augmentation of the rotation rate, a fact that set the pace for cavitation initiation.

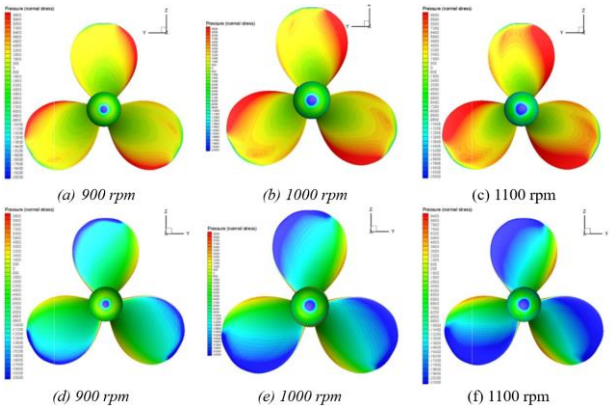

Figure 2 Pressure distribution on the pressure side (a) to (c) and on the suction side (d) to (f)

Figure 3 bears out the second invariant of the velocity gradient coloured in terms of pressure, Figure (a) to (c) and helicity, Figure (d) to (f), respectively. Vortices released by the blade tips unveil a well-defined helical structure growing up on the axial direction, then being eventually washed down in the stream. The increase of the revolution rate from 900 rpm to 1100 rpm brings out the slight decrease of the vortices pitch, as expected. Worth mentioning that a significant hub vortex develops axially behind the hub which coexists with the tip vortices and finally merge to weaken each other at the downstream.

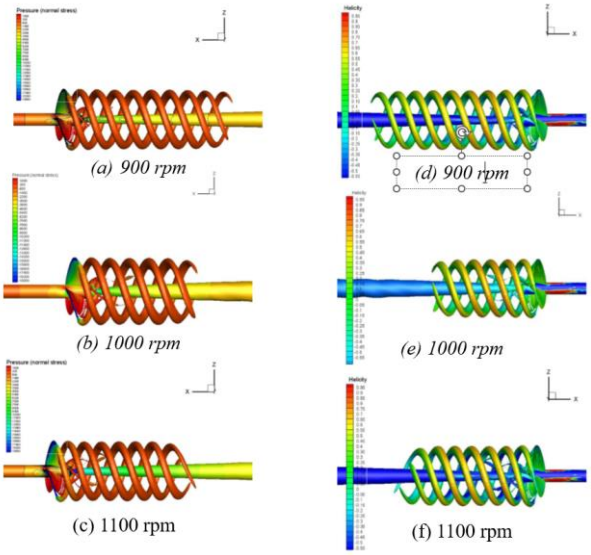

Figure 3 Pressure distribution considering second invariant (a) to (c) and helicity values (d) to (f)

Figure 4 depicts the main turbulent flow parameters drawn in the propeller wake for the three advance ratio coefficients considered in here. In spite of a rather poor discretization of the fluid domain behind the propeller, one may see the progressively decrease of the energy determined by the viscous dissipation, a fact that will further influence the overall propeller hydrodynamic performances.

After completing the numerical analyses, the thrust T, and the torque Q, produced by the propeller, were calculated in Table 3 and used to get the thrust and torque diagram, using KT and KQ coefficients, according to same advance ratio, see Figure 5. Because the two propellers of the ship rotate each in the other side, torque values may have negative values, depending the board where is mounted. For the sake of a proper evaluation, KQ values are introduced with their positive values.

Creative Commons Attribution BY 4.0 International Licence (CC BY-4.0)

Journal of Marine
Technology and Environment
DOI:10.53464/JMTE.01.2026.04
ISSN (Print): 1844-6116
ISSN (Online): 2501-8795
https://www. jmte.eu

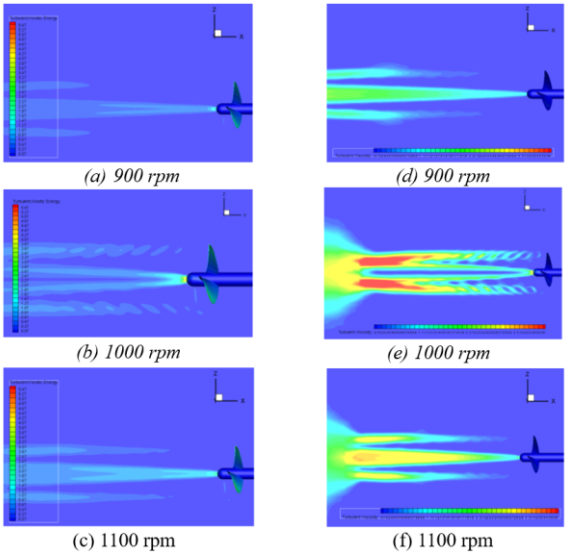

Figure 4 Turbulent kinetic energy (a) to (c) and turbulent viscosity (d) to (f)

Table 3. Thrust and torque values and coefficients

n [rpm]	J	T [N]	Q [Nm]	KT	KQ
900	0.666	428.6	-23.865	0.229	-0.042
1000	0.6	600.57	-32.335	0.26	-0.046
1100	0.545	792.89	-41.916	0.284	-0.05

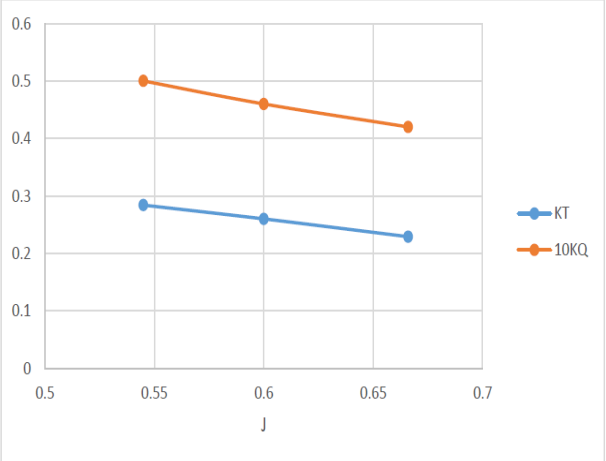

Figure 5 KT and KQ variation with the advance coefficient

As shown in Table 3, an increase of the revolution rate of the propeller, leads to higher values for the thrust and torque of the propeller, but under an unavoidable increment of the pressure fluctuation on the blade.

4. MITIGATION TECHNIQUES AND CONCLUDING REMARKS

The CFD simulation was performed with the aim of highlighting cavitation formation and occurrence, and it depicted how the vortices are initiated and developed. However, the context in modifying for the situation where cavitation erosion is observed in real operational conditions. Although it is not a common situation, the full scale propeller can suffer from cavitation erosion and its effects might be identified during periodical maintenance at the dry docking. In this case, the available time frame to implement a repair methodology and mitigation techniques it is very limited. Even so, measures are to be taken firstly to recondition the cavitation affected surfaces and furthermore, to optimise the cavitation resistance of the propeller alloy for the future.

For complex alloys such as the NAB from the marine propeller, repair techniques are a double challenge. On one side, depending on the affected area of the propeller, the repair itself might be prohibited, as regulated by IACS UR W24, and detailed more in other paper of the author, [1]. On the other side, the metallurgical structure and the high thermal conductivity of the NAB makes the alloy to be susceptible to cracking, residual stress between the grains and phases imbalances. Even so, it has been reported satisfactory repair of bronze alloy from the marine propeller with implementation of the emerging technology of laser cladding.

Tang et al. [9] obtained defect free laser cladding deposition on manganese nickel aluminium bronze propeller, with continuous laser methodology. Their technique revealed not only the possibility to rebuild the affected propeller, but also to expand the cavitation erosion resistance of the alloy up to almost 30 times more than the original material. Good outcome from laser cladding registered also Iatan et al. [10] by identification of the optimal parameters for laser cladding of a NAB substrate from a marine propeller with a pulsed laser. The study showed increasing the micro hardness and corrosion resistance of the original substrate, with the inherent asset of obtaining a defect free coating.

The present study describes through CFD instruments how cavitation occurs and grows on a marine propeller, pointing out on how the phenomenon can be analysed and limited at an early design stage. Furthermore, modern laser repair and material optimisation methodologies are introduced as a response to the situation where cavitation erosion became a consistent and real problem for vessel in operation.

Creative Commons Attribution BY 4.0 International Licence (CC BY-4.0)

Journal of Marine
Technology and Environment
DOI:10.53464/JMTE.01.2026.04
ISSN (Print): 1844-6116
ISSN (Online): 2501-8795
https://www. jmte.eu

5. FUNDING

There was no funding received for the present article.

6. CREdit authors statement

Conceptualization: G.I.

Data curation; A.L.

Formal analysis: G.I.

Funding acquisition: NIL

Investigation: G.I.

Methodology: G.I.

Project administration: G.I.

Resources: A.L.

Software: Numeca Fine Marine software

Supervision: A.L.

Validation: A.L.

Visualization: G.I.

Writing – original draft: G.I.

Writing – review & editing:. A.L.

7. REFERENCES

[1] Turof, M., 2023, *Analysis and dimensioning of the fuel supply system of bulk-carrier*, Journal of Marine Technology and Environment, ISSN: 2501-8795. https://doi.org/10.53464/JMTE.02.2023.14

[2] Lungu, A., 2007, *Numerical Simulation of the Free-Surface Turbulent Flow around a VLCC Ship Hull*, AIP Conf. Proc. 936, 647. https://doi.org/10.1063/1.2790231

[3] Iatan, G.C., Pascu, A., 2025, *Importance of periodical examination and maintenance of propellers for ensuring seaworthiness of cargo vessels*, The annals of "Dunarea de jos" University of Galati Fascicle XI – Shipbuilding. ISSN 1221-4620, e-ISSN 2668-3156. https://doi.org/10.35219/AnnUgalShipBuilding/2025.48.14

[4] Ene, O., Dinu D., 2024, *Short introduction on present design and trends regarding energy efficiency improvement on large crude oil tankers*, Journal of Marine Technology and Environment, ISSN (Online): 2501-8795. https://doi.org/10.53464/JMTE.02.2024.03

[5] Lungu, A., 2018, *Numerical simulation of the cavitating KP505 propeller working in open water conditions*, IOP Conf. Series: Materials Science and Engineering 400 (2018) 042035. https://iopscience.iop.org/article/10.1088/1757-899X/400/4/042035/pdf

[6] Lungu, A., 2020, *A DES-SST Based Assessment of Hydrodynamic Performances of the Wetted and Cavitating PPTC Propeller*, J. Mar. Sci. Eng. 2020, 8, 297. https://doi.org/10.3390/jmse8040297

[7] Abbasi, A., Franzosi, G., Viviani, M., Bertetta, D,, Tani, G., 2024, *Experimental analysis of blade root cavitation erosion on set of model propellers*, Ocean Engineering 311 (2024) 118766. https://doi.org/10.1016/j.oceaneng.2024.118766

[8] Aktas, B., Usta, O., Atlar, M., 2020, *Systematic investigation of coating application methods and soft paint types to detect cavitation erosion on marine propellers*, Applied Ocean Research 94 (2020) 101868. https://doi.org/10.1016/j.apor.2019.101868

[9] Tang, C. H., Cheng, F. T. , Man, H. C. , 2006, *Laser surface alloying of a marine propeller bronze using aluminium powder Part I: Microstructural analysis and cavitation erosion study*, Surface & Coatings Technology, 200, 2602–2609.

[10] Iatan, G. C., Cuculea, D. C., Ardelean, G., Stanciu, E. M, Pascu, A, 2025, *Optimization of Pulsed Laser Cladding for Reconditioning of Ni–Al–Bronze (NAB) Marine Propeller*, Materials 2025, 18. https://doi.org/10.3390/ma18184301

Creative Commons Attribution BY 4.0 International Licence (CC BY-4.0)

Journal of Marine
Technology and Environment
DOI:10.53464/JMTE.01.2026.05

ISSN (Print): 1844-6116
ISSN (Online): 2501-8795
https://www. jmte.eu

ENERGY-EXERGY ANALYSIS VERSUS ENERGY, EXERGY AND THERMOECONOMIC ANALYSIS – A CASE OF STUDY

Feiza MEMET[1]

[1] Constanta Maritime University, Faculty of Naval Electro-Mechanics, 104 Mircea cel Batran Street, 900663, Constanta, Romania, ORCID ID:0000-0002-3110-4254, feizamemet@yahoo.com

Abstract: On board of ships, cascade refrigeration systems are used when both frozen and refrigerated products are transported. In such a situation, two different levels of temperature are ensured in the same time. There are needed two conventional refrigeration systems which are coupled by a cascade heat exchanger. Thermodynamic analysis of these systems are important when aiming efficient design and performance optimization. The main objective of this paper is to present different analysis means such as energy, exergy or thermoeconomic (exergoeconomic). Also, there are analysed the challenges to be faced by engineers when developing a thermoeconomic analysis of cascade vapour compression refrigeration systems. Thermoeconomics analysis is a "sensitive issue" due to the interdisciplinary approach, being combined concepts of economics and thermodynamics to evaluate cost formation process of these thermal systems.

Key words: analysis, cascade, exergoeconomy, refrigeration.

1. INTRODUCTION

Refrigeration relyies on the first and second laws of thermodynamics, its goal being heat remove from a cold space to a higher temperature environment; this process is not a spontaneous one, being needed work input and phase changes of the working fluid (the refrigerant); this sector is growing rapidly and impacts areas such as: air conditioning, preservation and transportation of perishables, food processing, storing, etc [1].

Vapour compression refrigeration systems are commonly used in many refrigeration areas, including marine refrigeration. High demand regarding this industry rised challenges seeing important energy consumption amounts. For this reason, the optimization of these cycles is of a high importance. Because these systems are designed to work in optimum conditions, it is aimed the economical operation regime.

On board ships, cascade refrigeration systems are used when both frozen and refrigerated products are transported, in which case two different temperature levels must be ensured simultaneously. This system is obtained by coupling two conventional refrigeration systems. This coupling is made possible by a dual purpose heat exchanger (cascade heat exchanger). This heat exchanger plays the role of condenser for one of the conventional systems and the role of evaporator for the second system. Two different refrigerants circulate through the two traditional systems. These, having different thermodynamic properties, allow different temperature levels to be ensured during the voyage.

This paper deals with energy, exergy and thermoeconomic (exergoeconomic) analysis aspects of a cascade refrigeration system.

Exergy analysis, which is based on the first law of thermodynamics provides theoretical information on estimation of energy demands.

But the reality of practical settings is associated with the irreversibility of real processes. This is why both quantity and quality aspects of energy should be addressed in order to get a realistic perspective on the performance.

The solution is found in the use of exergy analysis which allows the understanding of energy losses by pointing out the sites of irreversible losses.

Moving forward, joining energy and exergy analysis with thermoeconomic analysis it is possible to achieve a comprehensive evaluation and optimization of the cascade refrigeration system.

Thermoeconomics is a new multidisciplinary field, suitable for the design optimization and diagnosis of energy systems which combines thermodynamic and economic analysis, by considering both efficiency and costs from second law perspective. According to Valero et al [2] and [3], exergy (which is introduced by the second law) is very suitable to allocate costs.

The exergy balance (eq. 1) quantifies the degradation of exergy and refers to the assessment of the useful energy inside a system.

Creative Commons Attribution BY 4.0 International Licence (CC BY-4.0)

Journal of Marine
Technology and Environment
DOI:10.53464/JMTE.01.2026.05
ISSN (Print): 1844-6116
ISSN (Online): 2501-8795
https://www. jmte.eu

$$Ex_i - Ex_o = I > 0 \quad (1)$$

where:
Ex_i – exergy input,
Ex_o – exergy output,
I – irreversibilities.

Seeing that the objective of a process is its efficiency, the following equation puts the efficiency expressed by concepts defined in the field of economics; these are the product and the resource.

$$\text{efficiency} = P/F \quad (2)$$

where:
P – product,
F – resource.

From this perspective, it is possible to write eq. 3 as:

$$F - P = R + I > 0 \quad (3)$$

where:
R – residues.

Another goal of this paper is to provide a descriptive overview of the engineering challenges faced by the specialists when dealing with economic aspects to be introduced in an exergoeconomic analysis of a cascade vapour compression refrigeration system.

2. SYSTEM DESCRIPTION AND ENERGY, EXERGY AND THERMOECONOMIC ANALYSIS EQUATIONS

Figure 1 provides the schematic layout of the considered system. As mentioned above, there are two classic vapour compression refrigeration systems: a low temperature circuit – LTC and a high temperature circuit– HTC, connected in series by the use a cascade condenser (CC). The cascade condenser acts as a condenser for the LTC and as an evaporator for the HTC.

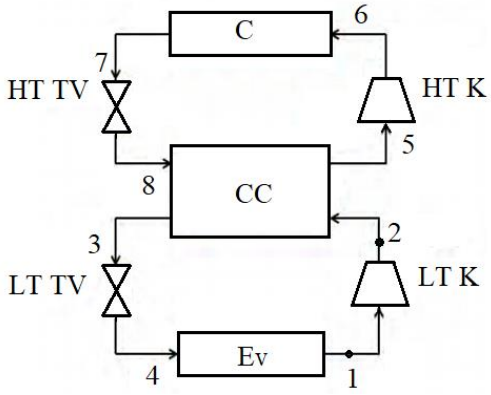

Figure 1 Cascade refrigeration system:
K – compressor, C – condenser, TV – throttling valve, Ev - evaporator

Energy analysis: the modelling is provided below [4], [5] as:

For the HTC:

$$\dot{m}_{HTC} = \frac{\dot{Q}_{CC}}{h_5 - h_8} \quad (4)$$

$$\dot{W}_{HTC} = \frac{\dot{m}_{HTC}(h_6 - h_5)}{\eta_{C,H}} \quad (5)$$

$$\dot{Q}_C = \dot{m}_{HTC}(h_6 - h_7) \quad (6)$$

For the LTC:

$$\dot{m}_{LTC} = \frac{\dot{Q}_{Ev}}{h_1 - h_4} \quad (7)$$

$$\dot{W}_{LTC} = \frac{\dot{m}_{LTC}(h_2 - h_1)}{\eta_{C,L}} \quad (8)$$

For all the system:

$$COP = \frac{\dot{Q}_{Ev}}{\dot{W}_{HTC} + \dot{W}_{LTC}} \quad (9)$$

Since there are three heat exchangers in the analysed system, the following equations are introduced:

$$\dot{Q} = U \cdot A \cdot LMTD \quad (10)$$

Creative Commons Attribution BY 4.0 International Licence (CC BY-4.0)

Journal of Marine
Technology and Environment
DOI:10.53464/JMTE.01.2026.05
ISSN (Print): 1844-6116
ISSN (Online): 2501-8795
https://www. jmte.eu

$$LMTD = \frac{(T_{h.i} - T_{c.o}) - (T_{h.o} - T_{c.i})}{\ln \frac{(T_{h.i} - T_{c.o})}{(T_{h.o} - T_{c.i})}} \quad (11)$$

where:
$\dot{m}$ – refrigerant mass flow rate, kg/s,
$\dot{W}$ – power input, W,
h – specific enthalpy, J/kg,
$\dot{Q}$ – heat flux, W,
η_C – isentropic efficiency of the compressor,
COP – Coefficient of Performance,
U – overall heat transfer coefficient of the heat exchanger, W/m^{2}K,
A – heat transfer surface, m^2,
LMTD – logarithmic mean temperature difference between two refrigerants,
T – temperature, K,
h/c – hot/cold,
i/o – inlet/outlet.

Exergy analysis: the modelling is provided below [6] as:

For the HTC:

$$\dot{E}x_{D.HTC} = \dot{W}_{HTC} + \dot{E}x_6 - \dot{E}x_5 \quad (12)$$

$$\dot{E}x_{D.C} = \dot{E}x_7 - \dot{E}x_6 \quad (13)$$

$$\dot{E}x_{D.HTTV} = \dot{E}x_8 - \dot{E}x_7 \quad (14)$$

$$\dot{E}x_{D.CC} = (\dot{E}x_8 - \dot{E}x_5) - (\dot{E}x_3 - \dot{E}x_2) \quad (15)$$

For the LTC:

$$\dot{E}x_{D.LTC} = \dot{W}_{LTC} + \dot{E}x_2 - \dot{E}x_1 \quad (16)$$

$$\dot{E}x_{D.Ev} = \dot{E}x_4 - \dot{E}x_1 \quad (17)$$

$$\dot{E}x_{D.LTTV} = \dot{E}x_4 - \dot{E}x_3 \quad (18)$$

$$\dot{E}x_{D.TOT} = \dot{E}x_{D.HTC} + \dot{E}x_{D.C} + \dot{E}x_{D.HTTV} + \dot{E}x_{D.CC} + \dot{E}x_{D.LTC} + \dot{E}x_{D.Ev} + \dot{E}x_{D.LTTV} \quad (19)$$

$$\eta_{ex} = \frac{(\dot{W}_{HTC} + \dot{W}_{LTC}) - \dot{E}x_{D.TOT}}{\dot{W}_{HTC} + \dot{W}_{LTC}} \quad (20)$$

where:
$\dot{E}x_D$ – exergy destruction, W,
$\dot{E}x$ – exergy, W,
η_{ex} – exergy efficiency.

Thermoeconomic analysis: the modelling is provided below [7], [8], [9], [10], [11] as:

Cost and price are different economic concepts. While cost is the amount of resources incurred in obtaining a product, price is the payment need for the acquiring of the product.

Cost estimation depends on policies and price estimation is done through facts. Processes to generate products are irreversible.

Since when exergy was proposed (as an energy term) to be related to cost, resulted a new analysis method (also known as exergoeconomic) suitable to be used in thermal systems optimization with a correctness not achievable by traditional methods.

Between price and worth can be establish a similitude.

Assessing an asset's worth involves a personal view– when it is about its estimation

The total capital investment of the cascade refrigeration system ($\dot{Z}_{system}$) and the capital investment cost rate of the k-th component of the system ($\dot{Z}_k$) are found by the use of the following formulae.

$$\dot{Z}_{system} = \sum_k \dot{Z}_k + \dot{Z}_{OPS} + \dot{Z}_{env} \quad (21)$$

where:
$\dot{Z}_{OPS}$ – operational cost of the system,
$\dot{Z}_{env}$ – environmental cost.

$$\dot{Z}_k = Z_k \cdot \Phi \cdot CRF \quad (22)$$

where:
Z_k – capital cost function,
Φ – maintenance factor,
CRF – capital recovery factor.

For the evaporator:

$$Z_{ev} = 1397 \cdot A_{ev}^{0.89} \quad (23)$$

For the condenser:

$$Z_C = 1397 \cdot A_C^{0.89} \quad (24)$$

For the cascade condenser:

$$Z_{CC} = 383.5 \cdot A_{CC}^{0.65} \quad (25)$$

For the HTC:

$$Z_{HTC} = 9624.2 \cdot W_{HTC}^{0.46} \quad (26)$$

Creative Commons Attribution BY 4.0 International Licence (CC BY-4.0)

Journal of Marine
Technology and Environment
DOI:10.53464/JMTE.01.2026.05
ISSN (Print): 1844-6116
ISSN (Online): 2501-8795
https://www. jmte.eu

For the LTC:

$$Z_{LTC} = 10167.5 \cdot W_{LHTC}^{0.46} \quad (27)$$

For the HTTV:

$$Z_{HTTV} = 114.5 \cdot \dot{m}_{HTC} \quad (28)$$

For the LTTV:

$$Z_{LTTV} = 114.5 \cdot \dot{m}_{LTC} \quad (29)$$

$$CRF = \frac{(i+1)^n}{(i+1)^n - 1} \quad (30)$$

where:
i – annual time interest rate,
n – life time of the system.

$$\dot{Z}_{OPS} = A_h \cdot (W_{HTC} + W_{LTC}) \cdot Z_{elec} \quad (31)$$

where:
A_h – annual operational time (in hours),
Z_{elec} – cost of electricity.

$$\dot{Z}_{env} = \dot{m}_{CO_2} \cdot Z_{CO_2} \quad (32)$$

where:
$\dot{m}_{CO_2}$ – amount of greenhouse gas emissions released by the cascade vapour compression system,
Z_{CO_2} – the cost of CO_2.

$$\dot{m}_{CO_2} = \lambda (\dot{W}_{HTC} + \dot{W}_{LTC}) \quad (33)$$

where:
λ – emission conversion factor, kg/kWh.

3. ENGINEERING CHALLENGES

Below are given identified challenges for engineers when introducing economic knowledge into cascade vapour compression refrigeration system (CVCRS) analysis within a thermoeconomic (exergo economic) approach.

A. The challenge of cost function accuracy – while conventional exergy analysis equations are governed by physical constants, thermoeconomic is ruled by cost functions; these are known to be difficult to be defined with precision for the vapour compression cascade systems.

Examples of non-liniar equipment cost are the cost of compressors or heat exchangers, which do not scale linearly with size, making engineers to work with specific power law equations.

There are also material constraints, since these systems might work at very low temperatures, while the two circuits of the system require for different material.

Engineers might be in difficulty when estimating the cost of specialized low temperature steels or alloys, without a specific training.

B. Temporal and macroeconomic volatility – within an energy analysis, the performance of the CVCRS is given by COP, which is constant for specific working input data.

Instead, thermoeconomic analysis reflects specific economic conjuncture.

In it important to pay attention to energy tariffs dynamism, seen that compressors are high energy consumers and the tariff for electricity depends on different factors, such as: hour of day, season, region, etc.

On the other hand, considering the lifetime of the system, it is obvious the need to predict interest rates and inflation.

A slightly change in borrowing costs can put pressure on a business decision, such as choosing between an expensive, energy-efficient system and a cheaper, less efficient one.

The initial decision might favour the high-efficiency option due to long-term savings, but if interest rates rise even gently, the increased cost of the initial investment makes the low-cost option more financially attractive.

C. The "cost allocation" uncertainty

As shown above, in CVCRS the cascade condenser plays two roles: one of condenser for the LTC and of evaporator for the HTC, resulting a systemic challenge from thermoeconomic point of view.

Specialists have to answer to the question: "how should be allocated the cost for exergy destruction in this heat exchanger?".

Engineers have to choose between two options: irreversibilities should be charge to the product (meaning the cooling at LTC evaporator) or should be shared between the two circuits.

Also, there is a recurrent costing, since the output of a cycle is the input for the second one.

In order to be solved the specific cost balance equations, are needed skills in matrix algebra that overpass the lacking between economics and thermodynamics.

D. Multi-objective optimization conflicts – resulting from antagonist position of thermodynamic perspective and economic profit.

Creative Commons Attribution BY 4.0 International Licence (CC BY-4.0)

Journal of Marine
Technology and Environment
DOI:10.53464/JMTE.01.2026.05
ISSN (Print): 1844-6116
ISSN (Online): 2501-8795
https://www. jmte.eu

It is needed the use of the exergoeconomic factor, that is able to reveal to engineers if the cost of the system is subjected by the initial purchase price or the operational inefficiency.

In the case of low values of this factor, specialists should be aware that they have to buy a more performant equipment.

Also, nowadays engineers have to pay attention to environmental regulations. Thus, they must consider the exergoenvironmental costs, such as carbon taxes or refrigerant GWP penalties. They must incorporate variable environmental compliance costs alongside total annual costs, that introduces a significant new dimension to financial modelling.

4. CONCLUSIONS

The main conclusions are given below:

- energy analysis offers limited outcomes since it provides theoretical information on estimation of energy demands,
- exergy analysis permits the understanding of energy losses, being able to indicate the sites of irreversible losses,
- exergoeconomic (thermoeconomic) analysis establishes a link between identification and quantification of irreversibilities and costs,
- for engineers, thermoeconomics is a delicate mission, they having to handle with the challenge of cost function accuracy, temporal and macroeconomic volatility, “cost allocation” uncertainty and multi-objective optimization conflicts.

5. CREdit Authors Statement

Conceptualization, Data curation, Formal analysis, Funding acquisition, Investigation, Methodology, Project administration, Resources, Software, Supervision, Validation, Visualization, Writing – original draft, Writing – review & editing: M. F.

6. REFERENCES

[1] Hajabdollahi H., Hosseini, Z., 2020, *Dynamical modelling and thermo-economic optimization of a cold room assisted vapor-compression refrigeration cycle*, Energy Equipment Systems, Vol. 8, No. 2, pp. 153-167.

[2] Valero A., Cuadra C.T., *Thermoeconomic analysis*, Exergy, Energy System Analysis and Optimization, Vol. II, Oxford, United Kindom: EOLSS Publishers, 2006, pp. 1-30, ISBN: 978-1-84826-165-5.

[3] Valero A., Uson S., Torres C., Valero A., 2010, *Application of thermoeconomics to industrial ecology*, Entropy, Vol. 12, pp. 592-611.

[4] Shanmugasundar G., Logesh K., Cep R., Roy R., 2023, *Evaluating eco-friendly refrigerant alternatives for cascade refrigeration systems: a thermodynamic analysis*, Processes, Vol. 11, pp. 1-17.

[5] Hacipasaoglu S.G., Ozturk I.T., 2025, *Thermoeconomic analysis and optimization of cascade refrigeration cycles incorporating ejector and environmentally friendly nano-refrigerant: a comparison study*, Journal of Thermal Analysis and Calometry, Vol. 150, pp. 10141-10155.

[6] Arouca L.B.P., Almeida A.G.S., Almeida F.S., da Cruz Duarte L.G., 2013, *Exergy analysis of cascade refrigeration system for low temperatures using ecological fluids*, Proc. of 22nd International Congress of Mechanical Engineering (COBEM2013), November 3-7, 2013, Ribeirao Preto, SP., Brazil, pp. 10221-10230.

[7] Aksu B., Uysal C., Kurt H., 2019, *Thermoeconomic analysis of a water to water heat pump under different condenser and evaporator conditions*, Journal of Thermal Engineering, Vol. 5, No.3, pp. 198-209.

[8] Picallo-Perez A., Sala J.M., del Portillo L., Vidal R., 2021, *Delving into thermoeconomics: a brief theoretical comparison of thermoeconomic approaches for simple cooling systems*, Frontiers in Sustainability, Vol. 2, pp. 1-12.

[9] Mohammadi K., Powell K.M., 2021, *Thermoeconomic evaluation and optimization of using different environmentally friendly refrigerants pairs for a dual-evaporator cascade refrigeration*, Processes, vol. 9, pp. 1-28.

[10] Carvalho F.N., Barbieri P.E.L., 2021, *Thermoeconomic simulation of cascaded and integrated vapour compression-absorption refrigeration systems*, Engenharia Termica (Thermal Engineering), Vol. 20, No. 1, pp. 93-99.

[11] Hajabdollahi H., Hosseini Z., 2020, *Dynamical modelling and thermo-economic optimization of a cold room assisted vapor compression cycle*, Energy Equipment and Systems, Vol. 8, No. 2, pp. 153-167.

Creative Commons Attribution BY 4.0 International Licence (CC BY-4.0)

Journal of Marine
Technology and Environment
DOI:10.53464/JMTE.01.2026.06

ISSN (Print): 1844-6116
ISSN (Online): 2501-8795
https://www. jmte.eu

THE IMPLICATIONS OF NEUROMARKETING IN CONTEMPORARY MARKETING TECHNIQUES AND CONSUMER BEHAVIOUR

Vanesa PETRAȘCU [1*], Elena CARP[1]

[1*] Moldova State University, 60 Alexei Mateevici street, Chisinau, R. Moldova, e-mail address:vanessapetrascu14@gmail.com

Abstract : Neuromarketing is an emerging interdisciplinary field that combines neuroscience with marketing research to uncover insights into consumer behavior at the neural level. This article offers an academic examination of how neuromarketing techniques are applied in modern marketing practices and analyzes their implications for consumer decision-making. The study outlines the theoretical foundations of neuromarketing, including its methods for investigating consumers' subconscious responses. Key findings indicate that neuromarketing has significantly influenced areas such as advertising design, branding strategies, pricing tactics, and product development by revealing unspoken preferences and emotional reactions from consumers.
Key words : Neuromarketing; consumer behavior; neuromarketing techniques; neuroscience; subconscious responses; marketing research.

1. INTRODUCTION

Neuromarketing is a relatively new field, officially emerging in 2002 when Professor Ale Smidts coined the term "neuromarketing" [1]. Although the term itself seems suggestive enough, suggesting a combination of marketing and neuroscience, to properly define neuromarketing is a challenging task due to the various interpretations and perspectives associated with the term in question.

If we break down the core components of the term and analyze them particularly, traditionally, marketing can be defined as the activity aimed at creating a connection between products and consumers through the analysis and understanding of human behavior in the context of today's market. Regarding neuroscience, according to Plassmann (2012) [2], it can be defined as " the study of the nervous system aimed at understanding the biological basis of behavior"[3].

By synthesizing these two particular definitions, we can interpret neuromarketing as a field that aims to understand consumer behavior through the lens of unconscious processes. Lee (2007) defines neuromarketing as "the application of neuroscientific methods to analyze and understand human behavior in relation to markets and marketing exchanges"[4].

Neuromarketing can be considered a branch of neuroeconomics, which is itself a branch of neuroscience [3]. Thus, if we were to analyze neuromarketing as an integrated part of neuroscience, we can interpret it as a field of study that applies brain research methods to better understand consumer behavior and implement these insights in marketing strategies.

At the same time, it is important to view neuromarketing as a field with a strong interdisciplinary character, due to the fact that this field has its origins in various academic domains. This interdisciplinary nature not only contributes to the complexity of the field but also provides a solid foundation for understanding consumer behavior through diverse perspectives. Neuromarketing's connection with psychology offers the ability to understand the fundamental processes behind consumer decision-making, their motivation, as well as emotions.

From an economic point of view, neuromarketing complements the classical value theory by highlighting variations in value perception and interpreting purchasing acts as financial losses. Simultaneously, sociological implications (such as social structures, consumption trends, and cultural factors) offer in-depth insights into the sociological profiles of consumers.

2. METHODOLOGY

This study is conducted as a qualitative research based on a thorough review of existing literature on neuromarketing. The approach involves synthesizing findings from various academic sources, including conference papers and graduation theses focused on integrating neuroscience with marketing. By examining a range of academic perspectives – from theoretical models to empirical case studies – the paper provides an

Creative Commons Attribution BY 4.0 International Licence (CC BY-4.0)

Journal of Marine
Technology and Environment
DOI:10.53464/JMTE.01.2026.06
ISSN (Print): 1844-6116
ISSN (Online): 2501-8795
https://www. jmte.eu

overview of the current state of neuromarketing and its practical implications.

2.1 Theoretical Framework and Analysis :

Neuromarketing can be defined as the commercial use of neuroscientific tools—such as functional magnetic resonance imaging (fMRI), electroencephalography (EEG), and eye-tracking—to gain more reliable insights into consumer responses [5].

In essence, it seeks to uncover what consumers truly feel and think about marketing stimuli, even when those reactions occur at a subconscious level beyond the consumers' own awareness [5].

Researchers identify consumers' implicit emotional and cognitive reactions to advertisements, brands, and products by measuring physiological and neural signals [5]. For example, changes in brain activity can reveal a viewer's engagement or emotional arousal when exposed to a television commercial, offering a window into consumer preferences that traditional self-report methods might miss.

2.2 Neuromarketing Technologies:

A variety of technologies drawn from neuroscience and psychology are employed in neuromarketing studies to capture these hidden responses. Common neuromarketing techniques include neuroimaging methods like fMRI, which detects changes in blood flow in the brain to infer neural activation, and EEG, which records electrical brain waves in real time [6].

Other tools, such as eye-tracking cameras, monitor where and how long a person focuses on different elements of a visual ad or webpage; facial coding software analyzes micro-expressions for emotional cues; and biometric sensors measure arousal through galvanic skin response or heart rate. Table 1 provides an overview of several key neuromarketing tools and their uses in capturing consumer reactions.

Table 1. Neuromarketing Techniques and Their Uses

Technique	**Description**	**Application example**
EEG (Electroencephalography)	Records electrical activity of the brain with high temporal resolution, showing patterns of brainwaves (e.g., alpha, beta) in response to stimuli.	Testing real-time reactions to advertisements or identifying moments of peak engagement during a TV commercial.
fMRI (Functional Magnetic Resonance Imaging)	Measures changes in blood flow in the brain (via the BOLD signal) to map which regions are activated by certain stimuli.	Discovering which parts of a print advertisement draw attention first, or how a shopper scans a product display.
Eye-Tracking	Tracks eye movements and fixations to reveal where visual attention is directed on an ad, package, or webpage.	Discovering which parts of a print advertisement draw attention first, or how a shopper scans a product display.
GSR & Pupillometry	Galvanic skin response (measures skin conductance) and pupil dilation tracking, both indicators of physiological arousal or interest.	Assessing a viewer's emotional arousal during a movie trailer, or noting increased pupil size when a consumer sees a preferred option.
MEG (Magnetoence phalography)	Detects magnetic fields produced by neural activity, offering millisecond-level timing (like EEG) with improved spatial localization.	Researching the precise timing of brain responses to marketing stimuli (e.g., a neural reaction to a short subliminal message).

By applying these techniques, neuromarketing research can delve into the subconscious drivers of behavior that classical marketing models often treat as a "black box." Decades ago, marketing theorists acknowledged a gap in understanding what happens in consumers' minds between the marketing stimulus and the resulting purchase decision. Neuromarketing helps

Creative Commons Attribution BY 4.0 International Licence (CC BY-4.0)

Journal of Marine
Technology and Environment
DOI:10.53464/JMTE.01.2026.06
ISSN (Print): 1844-6116
ISSN (Online): 2501-8795
https://www. jmte.eu

fill this gap by directly observing neural correlates of attention, emotion, and decision-making [3]. This approach aligns with findings in cognitive psychology and behavioral economics which show that context, emotions, and automatic processes (i.e., the brain's fast "System 1" thinking) dominate much of consumer decision-making [5]. Kahneman's dual-system theory, for instance, suggests that intuitive and emotional judgments often guide consumer choices before rational deliberation ("System 2") comes into play [7]. Neuromarketing techniques, by capturing instinctive brain responses within milliseconds, essentially tap into the System 1 processes underlying consumer preferences. As illustrated in Table 1, an EEG readout of a consumer viewing an advertisement might show spikes in certain brainwave frequencies that correspond to heightened attention or emotional engagement at specific moments in the ad (e.g., during a dramatic scene or when a brand logo appears).

3. RESULTS AND DISSCUTIONS

The application of neuromarketing techniques in real-world marketing has yielded insights that directly inform strategy and tactics. In advertising, for example, neuromarketing studies help identify which elements of a commercial or print ad evoke the strongest neural and emotional responses, allowing creatives to optimize content [8]. One famous neuromarketing experiment used fMRI brain scans to compare consumer preferences for Coca-Cola vs. Pepsi [5]. When participants tasted the drinks without brand information, a majority preferred Pepsi. However, when they knew which brand they were tasting, many reported preferring Coca-Cola – and the brain scans revealed a substantially higher activation in emotional memory centers for Coke, driven by its powerful brand image [5]. This finding demonstrated how brand associations can actually overwrite taste preferences at the neural level, confirming the profound influence of branding on consumer experience.

Neuromarketing has likewise been employed to refine product design and packaging. By observing neural reactions to different package designs or product concepts, firms can choose the options that elicit the most positive subconscious response. Frito-Lay, for instance, worked with a neuroconsultancy to test consumer brain responses to various potato chip package designs [9].

The research indicated that glossy, image-laden bags triggered guilt-related brain responses in female consumers, whereas matte packaging with subtle visuals did not. This insight led the company to introduce new packaging that appealed more to their target market, contributing to increased sales [1].

In another case, automotive company Hyundai used EEG-based neuromarketing tests with a sample of consumers to develop a new car prototype; participants' brainwave feedback guided design adjustments that ultimately made the car more appealing [10], [11]. These examples illustrate how neuromarketing allows for data-driven tweaks to marketing elements that traditionally would rely on intuition or self-reported preferences.

Beyond individual case studies, broader marketing domains have been impacted by neuromarketing findings. Research indicates that neuromarketing can significantly influence marketing's core "four P's": product, price, place (distribution), and promotion. Neuroscientific insights have been used to fine-tune pricing strategies (for example, identifying pricing formats that the brain perceives as more attractive or fair), to optimize store layouts and product placements in retail environments, and to shape branding strategies that resonate emotionally with consumers [1], [3].

In terms of promotion, advertisements designed with neuromarketing input often aim to tell stories or use imagery that activates desired brain regions associated with pleasure, trust, or memory. Branding efforts, similarly, focus on building sensory and emotional associations (sound, color, imagery) that reinforce brand identity at a subconscious level.

As neuromarketing knowledge permeates the industry, even marketers who do not have direct access to fMRI machines or EEG labs are adopting its lessons. Seemingly minor design choices—such as the color scheme of a website or product packaging—are now recognized as having outsized effects on consumer perception and are often informed by psychological research [1]. Colors can evoke specific emotions and associations: for example, using shades of blue in a logo or store décor can foster feelings of trust and stability, while black or gold can connote luxury [1]. Similarly, the placement of visual elements follows principles gleaned from eye-tracking studies; for instance, important messages or call-to-action buttons are positioned where viewers' eyes naturally travel. Despite these promising applications, the rise of neuromarketing has been met with considerable scrutiny regarding ethics and consumer welfare.

Observers have raised concerns that neuromarketing could be used to manipulate consumers at a neurological level, effectively finding a "buy button" in the brain that, if pressed, would compel people to purchase involuntarily [5], [6]. Such fears, while exaggerated, underscore the importance of transparency and consent in any research that scans brain activity for commercial purposes.

In reality, neuromarketing does not confer mind control—consumers still exercise free will—but it does provide marketers with more effective means of persuasion, which must be handled responsibly.

Some early claims around neuromarketing's power proved to be hype, and researchers caution against

Creative Commons Attribution BY 4.0 International Licence (CC BY-4.0)

Journal of Marine
Technology and Environment
DOI:10.53464/JMTE.01.2026.06
ISSN (Print): 1844-6116
ISSN (Online): 2501-8795
https://www. jmte.eu

misconceptions. For instance, the idea of a single neural trigger that guarantees a sale is a myth [5], and reputable neuromarketing studies focus on probabilistic increases in effectiveness rather than absolute guarantees of consumer behavior change. To address ethical concerns, industry organizations and scholars have begun developing guidelines for the responsible use of neuromarketing. There is a growing consensus that consumers' privacy and autonomy should be respected – for example, brain data should not be collected without informed consent, and interpretations of neural signals should be handled with care to avoid overreach. The Neuromarketing Science and Business Association (NMSBA) has even introduced a code of ethics, and academic discussions have proposed globally applicable ethical standards for neuromarketing research [3].

If such standards are rigorously applied, they can mitigate the risk of neuromarketing being used in manipulative or harmful ways [3]. Indeed, when conducted ethically, neuromarketing research can be seen as a tool to better satisfy consumer needs – for example, by avoiding advertisements that consumers subconsciously find distressing, or by designing products that genuinely delight users. Thus, the implication for consumer behavior is twofold: marketers gain deeper insight into how to influence choices, but they also carry a greater responsibility to align those influences with consumers' true well-being.

4. CONCLUSIONS

In summary, neuromarketing represents a significant advance in the toolkit of marketing research, illuminating the hidden layer of consumer cognition and emotion that traditional methods often cannot reach. The implications for contemporary marketing techniques are substantial: campaigns and product designs can be iteratively improved based on neural feedback, leading to marketing strategies that are not only more effective but also more attuned to genuine consumer preferences.

The influence of neuromarketing on consumer behavior is most vident in its confirmation of a long-held suspicion in marketing: much of consumer decision-making happens beyond conscious awareness. Neuromarketing provides concrete, empirical support for this idea, showing that factors like brand familiarity, emotional resonance, and sensory cues can sway consumers on an unconscious level [5].

Acknowledging this reality has encouraged marketers to craft experiences that connect with consumers more authentically – for instance, by storytelling that evokes emotion rather than relying on rational arguments alone. At the same time, this knowledge places greater ethical demands on marketers to avoid exploiting vulnerabilities in the consumer psyche.

As an evolving interdisciplinary field, neuromarketing still faces challenges, including technical limitations, the need for more standardized methodologies, and ongoing skepticism from both the public and some academics. Yet, its trajectory points toward growing integration with mainstream marketing. Continued research and technological progress (such as more portable brain-scanning devices or advanced AI for data analysis) are likely to make neuromarketing insights even more accessible and actionable in the near future.

Ultimately, when applied judiciously, neuromarketing has the potential to create more effective marketing campaigns and better products – innovations that benefit businesses and consumers alike – while also deepening our scientific understanding of how and why people make the choices they do.

As we look ahead, the synergy of neuroscience and marketing may well become a cornerstone of consumer research, enabling a future in which marketing not only sells more effectively, but also resonates more meaningfully with the human brain and heart.

5. CREdit authors statement

Conceptualization:P.V; C.E.

Creative Commons Attribution BY 4.0 International Licence (CC BY-4.0)

Journal of Marine
Technology and Environment
DOI:10.53464/JMTE.01.2026.06
ISSN (Print): 1844-6116
ISSN (Online): 2501-8795
https://www. jmte.eu

Data curation: P.V; C.E.

Formal analysis: P.V; C.E.

Funding acquisition:-

Investigation: P.V; C.E.

Methodology: P.V; C.E.

Project administration: P.V.

Resources: P.V; C.E.

Software:-

Supervision: P.V; C.E.

Validation: P.V; C.E.

Visualization: P.V; C.E.

Writing – original draft: P.V.

Writing – review & editing:P.V.

6. REFERENCES

[1] Tamașciuc, V., 2019. *Neuromarketing: art, science, opportunity*. In: Proceedings of the 17th International Scientific Symposium of Young Researchers, ISBN 978-9975-75-961-8, 73–74, Chișinău, Moldova.

[2] Plasmann, H., Ramsøy, T.Z., Milosavljevic, M., 20212. *Branding the Brain – A Critical Review and Outlook*, Journal of Consumer Psychology, vlo. 22(1):18–36.

[3] Roth, V. A., 2013. *The Potential of Neuromarketing as a Marketing Tool* (Bachelor's thesis), University of Twente, 25-28. Enschede, Netherlands.

[4] Lee N, Broderick AJ, Chamberlain L., 2007. *What is 'neuromarketing'? A discussion and agenda for future research*, Int J Psychophysiol, vol. 63:199–204.

[5] Strieder, N., 2022. *Neuromarketing: Human Behaviour & Decision Making in Consumer Based Neuroscientific Research* (Master's thesis), Aalborg University Business School, 4-7, Aalborg, Denmark.

[6] Nastai (Remete), A. N.,2022. *Cercetări în neuromarketing* [Research in neuromarketing] (Doctoral dissertation summary), p. 2; 4-6. Technical University of Cluj-Napoca, Romania.

[7] Kahneman, D., 2011. Thinking, Fast and Slow. Penguin Books.

[8] McClure, S. M., Li, J., Tomlin, D., Cypert, K. S., Montague, L. M., & Montague, P. R., 2004. *Neural correlates of behavioral preference for culturally familiar drinks*. Neuron, 44 (2):379-387.

[9] https://www.tastingtable.com/1024171/the-science-behind-frito-lays-potato-chip-marketing-technique/

[10] https://www.forbes.com/forbes/2009/1116/marketing-hyundai-neurofocus-brain-waves-battle-for-the-brain.html

[11] Atilla Yücel, Ahmed İhsan Simsek, 2019. *measuring consumer brand perceptions in terms of neuromarketing by using the EEG method: An experimental study on the automotive industry*, Eurasian Journal of Researches in Social and Economics (EJRSE)ISSN:2148-9963, 121-133.

Creative Commons Attribution BY 4.0 International Licence (CC BY-4.0)

Journal of Marine
Technology and Environment
DOI:10.53464/JMTE.01.2026.07

ISSN (Print): 1844-6116
ISSN (Online): 2501-8795
https://www. jmte.eu

A REVIEW OF INNOVATIVE WIND TURBINES AND PHOTOVOLTAIC ARCHITECTURES

Ciprian POPA[1] & Andrei-Darius DELIU[2*]

[1]Romanian Naval Academy "Mircea cel Bătrân", Faculty of Marine Engineering, 1 Fulgerului Street, 900218, Constanța, Romania, ORCID ID 0009-0001-8630-7729, e-mail address: ciprian.popa@anmb.ro
[2*]National University of Science and Technology Politehnica Bucharest, Faculty of Electrical Engineering, 313 Splaiul Independentei Street, 060042, Bucharest, Romania, corresponding e-mail address: andrei_darius.deliu@stud.electro.upb.ro

Abstract: This study is framed by the accelerating displacement of fossil energy carriers, driven by depletion and externalities (GHG emissions and ecosystem impacts), and by the global shift toward converter-interfaced variable renewable energy (VRE). The objective is to justify, using recent deployment evidence, why next-generation photovoltaic (PV) and wind energy conversion system (WECS) technologies constitute the highest-leverage innovation targets for near-term capacity scale-up and grid-compatible decarbonization. Methodologically, the work combines (i) macro-trend interrogation of IRENA renewable capacity statistics (2015–2024) with (ii) a structured technology review of emerging wind concepts (vortex-induced vibration bladeless harvesters, passive/ducted building-integrated turbines, and modular multi-rotor architectures) and advanced PV architectures (bifacial modules and transparent PV/TLSC devices), focusing on dominant physical mechanisms, conversion chains, and deployment constraints. Results show that 2024 delivered a record +585 GW (+15.1%) renewable capacity expansion, with PV (+452 GW; +32.2%) and wind (+113 GW; +11.1%) contributing 96.6% of net additions, whereas hydro, bioenergy, and geothermal exhibited marginal growth. Key technology bottlenecks are identified: resonance-bandwidth limits in VIV harvesters (addressable via adaptive stiffness tuning), aerodynamic losses and siting dependence in passive systems, and load/wake management in multi-rotor arrays; bifacial PV bankability remains coupled to rear-irradiance modelling and mismatch control, while TPV is constrained by the transparency-efficiency trade-off. The findings indicate that accelerating PV/WECS innovation is pivotal for sustained renewable expansion under realistic environmental variability.

Key words: Energy conversion, bladeless wind turbine, photovoltaic systems, renewable energy, wind energy conversion systems.

1. INTRODUCTION

The progressive depletion of conventional fossil-based energy carriers, most notably petroleum and natural gas, together with their well-documented externalities (greenhouse-gas emissions, criteria air pollutants, and broader ecosystem impacts), has reached a level that is increasingly viewed as a systemic constraint for long-term industrial development. This convergence of resource scarcity, climate forcing, and environmental degradation has intensified scientific and engineering efforts toward scalable, low-carbon energy conversion pathways and has accelerated innovation across the renewable energy landscape [1], [2], [3], [4], [5].

Within this framework, renewable resources have acquired strategic relevance because they are intrinsically replenished on human time scales, exhibit favorable life-cycle environmental profiles, and are broadly available across diverse geographies. Among the main renewable options: solar, wind, hydropower, and marine/tidal systems, solar photovoltaics (PV) and wind energy conversion systems (WECS) have emerged as the fastest-growing technologies worldwide, driven by rapid cost declines, modular deploy ability, and maturity of manufacturing and grid-integration ecosystems. From a physical standpoint, these technologies directly transduce naturally occurring energy fluxes into electrical power: PV modules convert incident solar irradiance into direct current via semiconductor junction processes (photogeneration, charge separation, and carrier collection), whereas wind turbines extract kinetic energy from atmospheric flow and convert it to electricity through aerodynamic torque production

Creative Commons Attribution BY 4.0 International Licence (CC BY-4.0)

Journal of Marine
Technology and Environment
DOI:10.53464/JMTE.01.2026.07
ISSN (Print): 1844-6116
ISSN (Online): 2501-8795
https://www. jmte.eu

coupled to electromechanical generators. Importantly, during operation both pathways provide electricity generation with negligible direct atmospheric emissions, enabling decarbonized power supply when appropriately integrated with power electronics, control strategies, and grid-support functionalities [6], [7], [8], [9], [10].

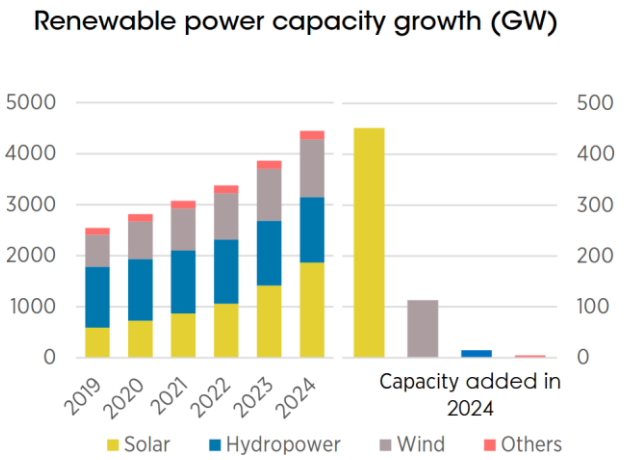

Figure 1 Global cumulative installed renewable power capacity by energy source, 2015–2024 (IRENA data) [11]

Based on IRENA (International Renewable Energy Agency) statistics, global renewable installed power capacity registered an unprecedented expansion in 2024, increasing by 585 GW, which corresponds to a +15.1% year-on-year growth rate. The decomposition of net additions by technology indicates a highly concentrated growth pattern dominated by variable renewable energy (VRE) sources: solar photovoltaics (PV) contributed +452 GW (+32.2%), accounting for more than three quarters of the total capacity increment, while wind power added +113 GW (+11.1%). In contrast, dispatchable and legacy renewable technologies exhibited markedly lower marginal growth: renewable hydropower increased by +15.0 GW (+1.2%), bioenergy by +4.6 GW (+3.2%), and geothermal by +0.4 GW (+2.5%) [11].

From a system-level perspective, the 2024 capacity build-out is characterized by an intensified reliance on PV–wind deployment, with solar and wind jointly representing 96.6% of all net renewable additions. This technological skew underscores the continued acceleration of converter-interfaced generation within the global portfolio, driven by the scalability and modularity of PV and the mature supply-chain dynamics of onshore/offshore wind [11].

Motivated by these highly consequential IRENA-derived capacity expansion trends, where solar PV and wind exhibit a markedly accelerated, near-exponential growth trajectory relative to other renewable technologies, this study strategically concentrates on the most recent technological advancements in photovoltaic module architectures and wind turbine systems, as these rapidly evolving, high-deployment-rate domains presently constitute the dominant vectors of global renewable capacity growth and, consequently, offer the greatest leverage for performance gains, cost reduction, and grid-integration scalability.

2. INNOVATIVE WIND TURBINE TECH CONCEPTS

2.1 Bladeless turbine

In recent years, a growing body of research has focused on enhancing the energy-conversion efficiency of wind harvesting devices that rely on vortex-induced vibration (VIV) as the primary transduction mechanism, rather than conventional aerodynamic torque production [12], [13], [14], [15]. Within this class, hybrid bladeless turbines have emerged as a promising architecture, integrating electromagnetic induction (EMI) and piezoelectric transduction in a single system to broaden the conversion pathways and increase net electrical output. The hybridization strategy is motivated by the complementary characteristics of the two mechanisms, namely, the comparatively high current capability and robustness of EMI-based generators versus the high voltage density and compact form factor of piezoelectric elements, thereby enabling improved electromechanical coupling and potentially higher overall conversion efficiency under suitable operating conditions [16]. Nevertheless, the performance of VIV-based harvesters remains strongly governed by frequency matching: peak energy extraction occurs only when the excitation (vortex-shedding) frequency is synchronized with the structure's natural frequency, i.e., within the resonant lock-in regime, which constrains efficiency under highly variable wind fields [12], [13], [14], [15], [16].

A canonical bladeless wind turbine typically comprises a slender mast (often approximated as a circular cylinder) elastically mounted to a rigid foundation via a compliant element (flexible rod or spring–damper assembly), as schematically indicated in Fig. 2. Unlike classical horizontal-axis or vertical-axis turbines, this configuration does not employ rotating blades to generate shaft power; instead, it converts the wind's kinetic energy into transverse structural oscillations driven by vortex shedding. As uniform flow impinges on the cylindrical body, separation occurs and a periodic wake develops, producing alternating low-pressure regions on either side of the cylinder and thereby generating an oscillatory lift force approximately normal to the mean flow direction. For appropriate Reynolds-number intervals, the wake organizes into a von Karman vortex street, and the corresponding unsteady aerodynamic loading can excite the structure into sustained vibrations. Under lock-in conditions, the vortex-shedding frequency adapts toward the structure's natural frequency, substantially amplifying vibration amplitude and, consequently, the available mechanical

Creative Commons Attribution BY 4.0 International Licence (CC BY-4.0)

Journal of Marine
Technology and Environment
DOI:10.53464/JMTE.01.2026.07
ISSN (Print): 1844-6116
ISSN (Online): 2501-8795
https://www. jmte.eu

power for conversion. The harvested energy thus follows a two-stage pathway: wind kinetic energy → mechanical vibration energy → electrical energy via coupled transducers [12], [17], [18], [19].

From an electromechanical integration perspective, the compliant support is coupled to an energy conversion module consisting of a coil-magnet assembly and/or piezoelectric elements, depending on the hybrid topology. In the electromagnetic branch, relative motion between the coil and the magnetic field induces an electromotive force according to Faraday's law, with the output strongly dependent on flux density, coil geometry, and the relative velocity of the moving component. For analytical tractability, the magnetic field is frequently modeled as quasi-uniform in the active region, a reasonable approximation when the flux is generated by axially symmetric permanent magnets and the air-gap is designed to minimize spatial non-uniformity. This assumption simplifies the derivation of the electromechanical coupling coefficient and the equivalent circuit representation used for coupled aeroelastic–electrical simulations [12], [17], [18], [19].

Figure 2 Wind energy system with bladeless turbines [20]

Peak vibration amplitudes in vortex-induced vibration (VIV) harvesters are attained when the vortex-shedding frequency, f_s, coincides with the dominant structural natural frequency, f_n, i.e., $f_s \approx f_n$. This operating condition is typically described as aeroelastic resonance and is frequently associated with the lock-in regime, in which wake dynamics synchronize with the structural response, resulting in a marked increase in oscillation amplitude and mechanical power availability. Within this regime, the unsteady aerodynamic loading-primarily the lift component induced by alternating vortex shedding, is commonly represented in reduced-order formulations as a quasi-harmonic (approximately sinusoidal) excitation acting transverse to the mean flow. The electromechanical conversion stage is then implemented via electromagnetic induction, whereby relative motion between a coil and a magnetic flux field induces an electromotive force in accordance with Faraday's law, consistent with the fundamental operating principle of conventional electromagnetic generators [19].

From a system-level perspective, bladeless VIV-based wind harvesters exhibit several practical advantages relative to bladed turbines. The most prominent benefit is the absence of rotating drivetrain components, which reduces mechanical complexity, mitigates failure modes associated with bearings/gearboxes, and lowers both manufacturing and life-cycle maintenance costs. Additionally, these devices can offer comparatively high power density per occupied area when deployed in arrays, due to reduced spacing constraints and the potential for closer packing without wake-interaction penalties typical of large-rotor systems. They are also generally associated with lower acoustic emissions and reduced ecological disturbance, particularly with respect to avian interactions, since they eliminate high-tip-speed blades that drive tonal noise and collision risk [12], [13], [14], [16], [19], [21]. A further operational advantage is their capability to sustain energy conversion at low mean wind speeds, provided that the aeroelastic system is tuned such that lock-in can occur within the prevalent wind-speed distribution, thereby improving the continuity of energy supply in weak-wind environments [18].

Notwithstanding these merits, the dominant performance constraint of VIV harvesters remains their strong dependence on resonant conditions. In realistic atmospheric boundary-layer flows, wind velocity is intrinsically non-stationary; thus, deviations from the resonant band ($f_s \neq f_n$) cause reduced oscillation amplitudes, weaker electromechanical coupling utilization, and a measurable decline in harvested power and conversion efficiency [19]. To alleviate this limitation, recent studies have proposed strategies to broaden the effective resonance bandwidth (or to shift resonance in real time), including the implementation of magnetorheological elastomers (MREs) with field-dependent stiffness. By modulating the shear modulus and effective stiffness through an applied magnetic field, MRE-based elements enable adaptive tuning of $f_n$and, consequently, improve frequency tracking relative to the variable excitation spectrum imposed by fluctuating wind conditions [14].

Experimental and modeling investigations indicate that magnetic-field-controlled stiffness variation can enhance energy capture by maintaining operation closer to the lock-in region over a wider range of wind speeds, thereby increasing average power output and reducing yield volatility. Beyond purely energetic metrics, such adaptive systems support decarbonization objectives by enabling distributed, low-maintenance renewable generation suitable for applications with stringent reliability constraints and limited servicing access, such as remote environmental sensing platforms and industrial automation nodes. Accordingly, VIV-based bladeless architectures-particularly when combined with adaptive

Creative Commons Attribution BY 4.0 International Licence (CC BY-4.0)

Journal of Marine
Technology and Environment
DOI:10.53464/JMTE.01.2026.07
ISSN (Print): 1844-6116
ISSN (Online): 2501-8795
https://www. jmte.eu

tuning, are increasingly positioned as enabling technologies within broader renewable energy transition pathways [12], [14], [18].

Reported performance figures in the literature further underscore the potential of the concept under optimized conditions. For example, an overall conversion efficiency of 82.7% has been documented for a specific operating point, corresponding to 1.438 W electrical output from 1.739 W extracted mechanical power. Such performance is typically attributed to the simplified mechanical architecture, characterized by the elimination of rotating gear trains and reduced parasitic drivetrain losses, suggesting that, with appropriate scaling and array-level design, bladeless VIV systems may offer a viable route toward higher-capacity implementations in future wind energy deployments [19].

2.2 Passive wind turbine system

Passive wind turbine technology has recently attracted increased attention as a non-conventional wind-harvesting paradigm, primarily because it is engineered to exploit built-in aerodynamic guidance rather than active yaw control or large-scale rotor orientation. In these architectures, the energy conversion unit is typically embedded within a stationary housing, and the system's ability to intercept and process the incoming flow is governed by the geometry of the intake, diffuser, and flow-acceleration features. The elimination of externally exposed rotating components substantially reduces tonal aerodynamic noise, mitigates vibration transmission to supporting structures, and decreases susceptibility to wear mechanisms associated with bearings, pitch systems, and yaw drives. As a result, passive wind concepts are frequently positioned as low-maintenance, low-disturbance solutions with reduced environmental footprint and limited wildlife interaction risk relative to open-rotor configurations [22], [23], [24], [25].

A defining aerodynamic mechanism enabling these devices is the Venturi effect, which arises when a fluid is forced through a locally constricted cross-section. In practical passive wind designs, the contraction is realized by two optimally contoured aerodynamic profiles (or guide-vanes/airfoils) that shape a converging passage. Under quasi-steady conditions, conservation of mass and Bernoulli-type arguments imply that the mean flow velocity increases in the throat region while the static pressure decreases, thereby establishing a pressure-driven entrainment that draws additional air from the lateral boundaries of the channel. This induced suction effectively increases the volumetric flow rate through the energy conversion core beyond what would be captured by the rotor's frontal area alone, thereby raising the available aerodynamic power flux delivered to the generator stage. The conversion unit typically consists of a small-diameter rotor placed within a duct connected to (or coincident with) the throat region, where the accelerated flow produces higher local dynamic pressure and improved rotor loading. Consequently, the wind's kinetic energy is converted into mechanical shaft power and subsequently into electrical power via an integrated generator, with overall performance strongly dependent on contraction ratio, loss coefficients, inlet turbulence intensity, and duct/rotor matching (i.e., the coupling between accelerated flow conditions and rotor aerodynamic characteristics) [22], [23], [24], [25], [26].

Figure 3 Concept of the Aeromine passive wind turbine system [24]

The Aeromine concept leverages a building-integrated aerodynamic flow-conditioning architecture intended to intensify and redirect the near-building wind field toward a compact power take-off unit. The system employs contoured airfoil-like fins and guide elements that impose a controlled redistribution of static pressure around the device, thereby establishing a sustained pressure gradient between the intake and the discharge region. This pressure differential drives an accelerated through-flow along a defined intake pathway and delivers conditioned airflow to an internally enclosed energy conversion stage. From an aerodynamic standpoint, the device functions as a localized flow

Creative Commons Attribution BY 4.0 International Licence (CC BY-4.0)

Journal of Marine
Technology and Environment
DOI:10.53464/JMTE.01.2026.07
ISSN (Print): 1844-6116
ISSN (Online): 2501-8795
https://www. jmte.eu

concentrator in which geometric contraction, guided turning, and pressure recovery are exploited to increase the effective mass flow rate through the conversion core relative to the ambient free-stream, with system performance governed by local boundary-layer behavior, turbulence intensity, and rooftop/edge flow separation phenomena [22], [23], [24], [25].

The electromechanical module typically incorporates a permanent-magnet generator (PMG) integrated within a sealed enclosure. Hermetic sealing reduces ingress of particulates, moisture, and saline aerosols (relevant for coastal installations), while passive thermal management (conduction to the housing and natural/forced convection to ambient air) supports long-duration operation without active cooling hardware. These design choices reduce failure susceptibility and extend service intervals by minimizing exposure of critical components to weathering and contamination. In certain implementations, the system is engineered to provide an AC output compatible with direct coupling to the building's electrical distribution architecture, thereby reducing balance-of-system complexity. Specifically, inverter-less operation can be achieved when the generator topology and power-conditioning strategy (e.g., grid-synchronous generation or integrated conversion within the machine electronics) are configured to meet voltage/frequency requirements, which can lower conversion losses and decrease installation and operational expenditures [22], [23], [24], [25].

Figure 4 Installation of the Aeromine passive wind turbine system on a building [24]

From an integration perspective, the device's vertically oriented, compact form factor is advantageous for deployment in urban and peri-urban environments where strict spatial constraints, setback requirements, and acoustic/environmental regulations often limit the feasibility of conventional open-rotor turbines. By concentrating the energy conversion components within a building-mounted enclosure and avoiding large exposed rotors, such systems can reduce visual impact, mitigate noise concerns, and simplify permitting pathways, thereby expanding the addressable application space for wind-derived generation in densely built settings [22], [23], [24], [25].

Aeromine-type systems are also well suited for hybrid renewable configurations, particularly in combination with rooftop photovoltaic (PV) arrays. The complementarity between wind and solar resource availability, driven by diurnal thermal gradients, seasonal weather patterns, and synoptic variability, can improve aggregate generation smoothness and increase the effective utilization of on-site electrical infrastructure. In practice, co-located wind–PV architectures can reduce reliance on grid imports during non-overlapping resource periods, improve self-consumption ratios, and support peak-shaving strategies, thereby enhancing both techno-economic performance and operational resilience [22], [23], [24], [25].

More broadly, the Aeromine approach aligns with sustainability-driven energy strategies by enabling distributed renewable generation that can be retrofitted into existing building stock and integrated into established electrical infrastructures with comparatively low additional balance-of-system burden. As regulatory and environmental constraints become increasingly stringent, building-integrated passive wind solutions provide a pragmatic pathway toward cleaner electricity supply, reduced operational carbon intensity, and improved energy autonomy at the building or campus scale [22], [23], [24], [25].

2.3 Modular multi-rotor wind energy system

Modular multi-rotor wind energy systems constitute an emerging alternative to conventional single-rotor, utility-scale turbines by adopting a distributed-rotor architecture in which multiple small or medium turbines are integrated into a coordinated array mounted on a common, typically vertical, support structure. The underlying design rationale is to increase the effective rotor-swept capture through modularity while mitigating well-known constraints of large-rotor platforms, including high yaw-system duty cycles under veering winds, elevated installation complexity, and the pronounced maintenance burden associated with large drive-train components and offshore logistics [27], [28], [29], [30], [31].

Creative Commons Attribution BY 4.0 International Licence (CC BY-4.0)

Journal of Marine
Technology and Environment
DOI:10.53464/JMTE.01.2026.07
ISSN (Print): 1844-6116
ISSN (Online): 2501-8795
https://www. jmte.eu

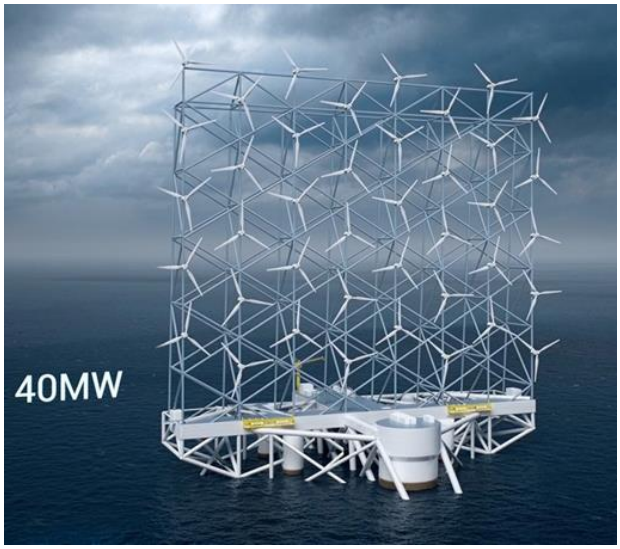

Figure 5 Modular multi-rotor wind system [30]

A principal technological advantage of this concept is its improved directional robustness. By distributing several rotors across a fixed frame and exploiting spatially varying inflow conditions, the system reduces dependence on continuous active yawing and can maintain energy extraction over a broader range of wind directions. In effect, the array behaves as a multi-aperture collector whose aggregate performance is less sensitive to instantaneous wind-direction fluctuations, thereby improving operational stability and resilience under non-stationary meteorological forcing (gusts, shear, turbulence intensity variations, and mesoscale directional shifts) [27], [28], [29], [30], [31].

From a structural–aerodynamic standpoint, modular multi-rotor configurations also enable a more favorable load partitioning relative to a single large rotor. Mechanical and aerodynamic loads are distributed among multiple units and transferred through the support structure as a superposition of smaller contributions, potentially reducing peak bending moments and allowing refined control of fatigue damage accumulation through redundancy and modular operation. Additionally, the distributed layout can improve wind-resource utilization by enabling design strategies that manage wake interactions at smaller spatial scales, with the possibility of tailoring rotor spacing and vertical placement to local shear profiles and turbulence structures. These attributes can support energy yields comparable to-or, in certain deployments, exceeding, those of a single large turbine, while reducing the overall environmental footprint through lower visual impact, potentially reduced wildlife interaction risk, and improved siting flexibility [27], [28], [29], [30], [31].

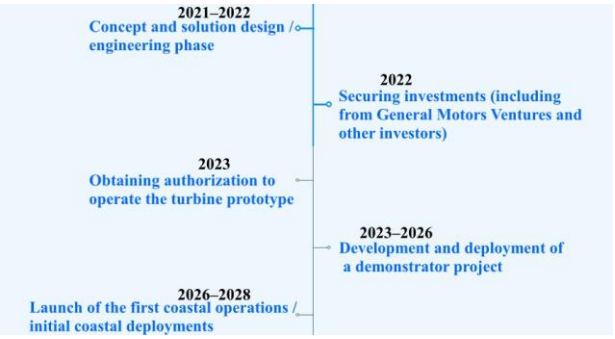

Figure 6 Project stages for the development of modular multi-rotor wind systems [30]

A further differentiator is the potential reduction in operations and maintenance (O&M) costs. Since aerodynamic loading and drivetrain torque are shared across multiple rotors, individual components experience lower extreme load events and may exhibit reduced wear rates, thereby extending service life and improving reliability. The modularity of the system can also enhance maintainability by enabling unit-level replacement (swap-out of a turbine module rather than major on-site overhaul), reducing downtime and limiting the scope of unplanned interventions-an especially relevant advantage for offshore/coastal installations where access windows are constrained and maintenance costs dominate life-cycle expenditure [27], [28], [29], [30], [31]. Over the project horizon, these effects translate into improved availability, reduced corrective maintenance frequency, and lower total operating costs.

Overall, modular multi-rotor systems represent a meaningful step in the evolution of wind-energy conversion technology by introducing a flexible, scalable design space that can reshape wind-farm engineering-particularly for offshore and coastal deployments where logistics, reliability, and structural scaling constraints are critical. By combining potential gains in annual energy production with reduced O&M intensity and improved environmental compatibility, this approach aligns with the broader objective of accelerating the transition toward cost-effective, low-carbon electricity generation [27], [28], [29], [30], [31].

3. INNOVATIVE PV TECH CONCEPTS

3.1 Bifacial photovoltaic systems

Bifacial photovoltaic (PV) modules differ fundamentally from monofacial architectures through the incorporation of optically transmissive rear encapsulation (e.g., glass–glass or transparent backsheet configurations), which enables photoactive conversion on both the front (direct-facing) and rear (ground-facing) surfaces. By activating the rear-side junctions, bifacial devices can convert not only the plane-of-array (POA) direct component but also a significant fraction of the

Creative Commons Attribution BY 4.0 International Licence (CC BY-4.0)

Journal of Marine
Technology and Environment
DOI:10.53464/JMTE.01.2026.07
ISSN (Print): 1844-6116
ISSN (Online): 2501-8795
https://www. jmte.eu

diffuse sky irradiance and the albedo-driven reflected component originating from the surrounding environment (ground cover, roof membranes, façade elements, and adjacent structures). Consequently, the energy yield of bifacial modules typically exceeds that of monofacial counterparts under identical front-side irradiance conditions, with the incremental gain governed by the rear irradiance ratio, spectral distribution, view factors, and array geometry. When deployed on single- or dual-axis trackers, bifacial configurations can exhibit substantial yield enhancements, commonly reported in the range of ~35–40% relative to fixed-tilt monofacial baselines, owing to increased POA irradiance capture and improved rear-side exposure over the diurnal cycle [32], [33], [34], [35], [36], [37], [38], [39].

Figure 7 Bifacial photovoltaic systems

The performance advantage of bifacial PV is further amplified in high-albedo settings (e.g., snow-covered terrain, bright sand, light-colored gravel) or when engineered reflective surfaces are introduced to increase effective ground reflectance. Under such boundary conditions, rear-side irradiance can become a non-negligible contributor to the total collected photon flux, thereby improving specific yield (kWh/kWp) and enhancing project-level economics in large-scale plants. These attributes render bifacial technology particularly attractive for utility-scale installations, where small percentage improvements in annual energy production translate into meaningful reductions in levelized cost of electricity (LCOE) and accelerated payback periods [32], [33], [34], [36], [40]

Beyond yield improvements, bifacial systems introduce additional degrees of freedom in site design and layout optimization. Parameters such as module elevation, row spacing, tilt, and the selection of ground treatment (e.g., reflective coatings, membranes, or optimized ballast layouts) can be tuned to manage the rear irradiance field and mitigate self-shading. This flexibility is especially relevant for commercial and industrial rooftop deployments, where geometric constraints and shading from parapets or rooftop equipment can be addressed through optimized placement and structural integration. As a result, bifacial configurations provide a credible pathway to maximize energy harvest within a limited footprint while improving the sustainability metrics and techno-economic viability of PV projects [32], [33], [35], [37]

Despite these advantages, bifacial PV systems still face non-trivial technical challenges. Key issues include (i) minimizing electrical mismatch and power losses induced by partial shading (row-to-row shading, structural shading from mounts and clamp zones, and transient shading from nearby objects), (ii) accurately quantifying rear-side irradiance under complex, time-varying boundary conditions, and (iii) developing reliable energy-yield models that capture anisotropic diffuse irradiance, spectral effects, and geometry-dependent view factors. In practice, uncertainty in rear irradiance modeling can propagate into yield prediction errors, affecting bankability and system sizing. Nevertheless, continuous progress in bifacial performance characterization, standardized measurement protocols, advanced ray-tracing/thermal-electrical co-simulation frameworks, and field validation campaigns is consolidating bifacial modules as a cornerstone technology for next-generation PV deployment and the broader transition toward low-carbon energy systems [32], [40], [41].

3.2 Transparent photovoltaic panels (TPV)

Transparent photovoltaic (TPV) panels show substantial potential across multiple application domains, particularly in the built environment and in agricultural systems. In agricultural settings, TPV modules can deliver low-emission electricity generation while simultaneously providing partial shelter for crops against adverse weather (e.g., heavy rainfall) and certain pest pressures, and they may also support covered areas intended for post-harvest handling or grain storage. As urban agriculture expands, the development and deployment of advanced technologies have become increasingly important; however, technology integration can also increase on-site energy demand. In this context, agrivoltaic systems, which co-locate crop cultivation and photovoltaic power generation on the same land footprint, have demonstrated the capability to improve both plant biomass productivity and electrical energy yield when appropriately designed and managed [42], [43], [44], [45].

A promising TPV approach employs transparent luminescent solar concentrator (TLSC) technology, in which the device selectively absorbs ultraviolet and infrared components of the solar spectrum and converts them into electricity while maintaining visible-light transmission. Using an indium–tin oxide (ITO) functional layer together with silver electrodes, such devices have been reported to achieve power conversion efficiencies up to 10.8% with an average optical transmittance of 45.8%, indicating a practical trade-off

Creative Commons Attribution BY 4.0 International Licence (CC BY-4.0)

Journal of Marine
Technology and Environment
DOI:10.53464/JMTE.01.2026.07
ISSN (Print): 1844-6116
ISSN (Online): 2501-8795
https://www. jmte.eu

between energy harvesting and transparency for integrated applications [46].

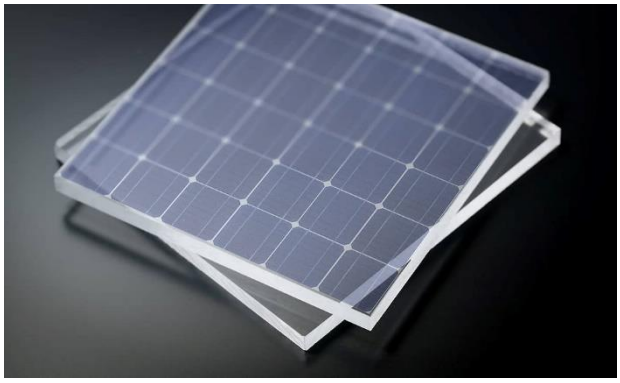

Figure 8 Transparent photovoltaic (TPV) panel

Transparent solar panel technology constitutes a notable advance in renewable energy engineering, providing an efficient and architecturally appealing pathway for solar harvesting in urban environments. These devices can be integrated into window assemblies and other glazed building envelopes, enabling high transmission of visible light while selectively absorbing portions of the solar spectrum to generate electricity, thereby maintaining indoor daylighting performance while delivering on-site power generation [43], [45], [46].

A further critical contribution of transparent PV systems lies in their potential to improve building energy performance. By modulating solar radiation entering the interior space, such glazing-integrated devices can reduce cooling loads and, consequently, lower operational energy costs and associated carbon emissions. In addition, the technology expands design flexibility for sustainable infrastructure, as it can be adapted to a wide range of architectural typologies and urban design constraints [43], [46].

4. CONCLUSIONS

IRENA capacity statistics confirm a structural shift in global renewable deployment toward converter-interfaced variable renewable energy (VRE), with solar PV and wind jointly dominating net additions in 2024; consequently, future decarbonization trajectories will be disproportionately governed by the performance, cost, and grid-integration capabilities of PV and WECS, centric technology pathways.

The examined non-conventional wind-harvesting architectures, vortex-induced vibration (VIV) bladeless systems, passive/ducted building-integrated concepts, and modular multi-rotor arrays, collectively target the principal limitations of conventional large-rotor turbines (O&M intensity, noise, wildlife impact, siting constraints, and directional sensitivity) through simplification of drivetrain topology, flow-conditioning-driven capture, and distributed load partitioning.

For VIV-based bladeless harvesters, the fundamental bottleneck remains resonance dependence (lock-in bandwidth), implying that practical scalability under non-stationary atmospheric forcing is contingent upon adaptive tuning strategies (e.g., magnetorheological elastomers) capable of real-time natural-frequency modulation and sustained electromechanical coupling under variable inflow spectra.

Passive wind systems leveraging Venturi-driven flow acceleration and pressure-gradient entrainment indicate a viable route for urban/peri-urban wind utilization, where compact form factors and enclosed power take-off modules can reduce acoustic emissions and mechanical wear while enabling integration into existing building electrical infrastructures and hybrid rooftop PV-wind configurations.

Distributed multi-rotor wind architectures introduce a scalable design space in which rotor modularity and redundancy can enhance availability and maintainability, while structural load redistribution and reduced yaw dependency can improve robustness to veering winds and turbulence, attributes that are particularly relevant for offshore/coastal deployments with constrained maintenance access windows.

On the PV side, bifacial module technology provides a high-leverage pathway for increasing specific yield (kWh/kWp) by harvesting rear-side irradiance components (diffuse and albedo-reflected), but bankable performance gains remain tightly coupled to accurate rear-irradiance modeling, mismatch-loss mitigation under partial shading, and geometry-dependent view-factor characterization.

Transparent photovoltaic (TPV) and TLSC-based devices extend PV functionality beyond conventional energy-only modules by enabling envelope-integrated generation and agrivoltaic co-utilization, where the key techno-physical trade-off is governed by the coupled optimization of spectral selectivity, optical transmittance, and power conversion efficiency under application-specific constraints.

Overall, the combined evidence supports the conclusion that near-term renewable scale-up will be maximized by accelerating innovation in PV module architectures and wind-conversion topologies that simultaneously improve energy yield, reduce life-cycle cost, and enhance deployment feasibility under spatial, environmental, and grid-operational constraints, thereby aligning technology development priorities with observed global capacity-growth dynamics.

5. FUNDING

The authors received no financial support for the research, authorship, and/or publication of this work.

Creative Commons Attribution BY 4.0 International Licence (CC BY-4.0)

Journal of Marine
Technology and Environment
DOI:10.53464/JMTE.01.2026.07
ISSN (Print): 1844-6116
ISSN (Online): 2501-8795
https://www. jmte.eu

6. Credit Author Statement

Conceptualization: P.C; D.D.A..

Data curation: P.C; D.D.A..

Formal analysis: P.C; D.D.A..

Funding acquisition: P.C; D.D.A..

Investigation: P.C; D.D.A..

Methodology: P.C; D.D.A..

Project administration: P.C; D.D.A..

Resources: P.C; D.D.A..

Software: P.C; D.D.A..

Supervision: P.C; D.D.A..

Validation: P.C; D.D.A..

Visualization: P.C; D.D.A..

Writing – original draft: P.C;

Writing – review & editing: P.C.

7. REFERENCES

[1] N. Ramadevi, K. Rajendra, D. Nagalakshmi, G. V. Satyanarayana, A. Rakesh, and K. L. Sai, "Design of Hybrid Solar & Wind Tree for Domestic Applications," *Proc. 2024 2nd Int. Conf. Cyber Phys. Syst. Power Electron. Electr. Veh. ICPEEV 2024*, 2024, doi: 10.1109/ICPEEV63032.2024.10932026.

[2] F. Ahmed, A. Begum, and M. M. Rashid, "Optimal Design and Techno-Economic Feasibility Analysis of Hybrid Renewable Energy Systems," Proc. 2024 IEEE Int. Women Eng. Conf. Electr. Comput. Eng. WIECON-ECE 2024, pp. 392–397, 2024, doi: 10.1109/WIECON-ECE64149.2024.10915171.

[3] P. P., "Study on the efficiency of a low-power vertical wind turbine," Sci. Bull. Nav. Acad., vol. XXII, no. 2, pp. 318–324, Dec. 2019, doi: 10.21279/1454-864X-19-I2-038.

[4] Y. Gao, H. Liu, K. Gao, and P. Wang, "Multi-Objective Optimization of a Integrated PV-CSP-Wind Power System Under Two Different Operational Mechanisms," 2024 11th Int. Forum Electr. Eng. Autom. IFEEA 2024, pp. 1194–1199, 2024, doi: 10.1109/IFEEA64237.2024.10878642.

[5] F. Deliu, P. Popov, P. Burlacu, and V. Dobref, "'Mircea cel Batran' licensed under the Creative Commons Attribution-Noncommercial-Share Alike 4.0 License. IMPLEMENTATION PHOTOVOLTAIC PANELS IN LIGHTING SYSTEM OF A SHIP," Nav. Acad. Sci. Bull., 2015, doi: 10.21279/1454-864X-16-I1-033.

[6] T. Deopujari, R. K. Nema, S. Nema, M. K. A. Ansari, S. K. Gautam, and T. Suryavanshi, "Modeling and Simulation of Hybrid PV-Wind-Battery Stand-Alone Generation System," 2024 IEEE 3rd Int. Conf. Electr. Power Energy Syst. ICEPES 2024, 2024, doi: 10.1109/ICEPES60647.2024.10653582.

[7] D. Monika et al., "Integrating Wind and Solar Energy: A Study on Measurement Accuracy and System Stability," 7th Int. Semin. Res. Inf. Technol. Intell. Syst. Adv. Intell. Syst. Contemp. Soc. ISRITI 2024 - Proc., pp. 605–609, 2024, doi: 10.1109/ISRITI64779.2024.10963525.

[8] G. S. Pratap, Midhunchakkaravarthy, and K. R. K. V. Prasad, "Implementation of Solar and Wind based Hybrid Renewable Energy System for in-House Power Generation," 2024 IEEE 11th Uttar Pradesh Sect. Int. Conf. Electr. Electron. Comput. Eng. UPCON 2024, 2024, doi: 10.1109/UPCON62832.2024.10983226.

[9] F. Deliu, P. Popov, and P. Burlacu, "The Impact of the Wind Speed on the Dynamics of the Wind Energy System," Int. Conf. KNOWLEDGE-BASED Organ., vol. 22, no. 3, pp. 628–633, Jun. 2016, doi: 10.1515/KBO-2016-0108.

[10] Adrian POPA, Beazit ALI, and Ionut Cristian SCURTU, "Considerations regarding Aerodynamic Interaction between Two Wind Turbines. Case of Study: Two Wind Turbines with Rotor Diameter of 6 Meters," Ecology, no. 1, 2017.

[11] I. R. E. Agency, "Renewable Capacity Highlights," Irena, no. April, pp. 1–3, 2023.

[12] H. Kang, S. Han, C. An, and Y.-K. Kim, "Design Process of a Small-Scaled Bladeless Vortex-Induced Wind Turbine with Tunable Resonance Mechanism," 2024 IEEE 22nd Int. Conf. Ind. Informatics, pp. 1–6, Aug. 2024, doi: 10.1109/INDIN58382.2024.10774332.

[13] D. Han, S. Huang, P. K. Abia Hui, and Y. Chen, "Development of a New Type of Vortex Bladeless Wind Turbine for Urban Energy Systems," 2024 9th Int. Conf. Power Renew. Energy, ICPRE 2024, pp. 973–978, 2024, doi: 10.1109/ICPRE62586.2024.10768593.

[14] H. Y. Kang and Y. K. Kim, "Development of Smart-Rubber Based Resonance Tuning Module for Bladeless Wind Turbine System," Int. Conf. Control. Autom. Syst., pp. 1830–1833, 2023, doi: 10.23919/ICCAS59377.2023.10316880.

[15] Z. S. Bahri, W. Barday, S. Ez-Zabri, and Y. Salih-Alj, "Design Considerations of a Hybrid Piezoelectric-Electromagnetic Tuning System for Vortex Induced Vibration Bladeless Turbines: Morocco Case Study," 2022 IEEE Int. Conf. Mechatronics Autom. ICMA 2022, pp. 611–616, 2022, doi:

Creative Commons Attribution BY 4.0 International Licence (CC BY-4.0)

Journal of Marine
Technology and Environment
DOI:10.53464/JMTE.01.2026.07
ISSN (Print): 1844-6116
ISSN (Online): 2501-8795
https://www. jmte.eu

10.1109/ICMA54519.2022.9855963.
[16] W. Barday, Z. S. Bahri, S. Ez-Zabri, and Y. Salih-Alj, "An Off-Grid Hybrid Piezoelectric-Electromagnetic Tuning System for Vortex Induced Vibration Bladeless Turbines," Colloq. Inf. Sci. Technol. Cist, pp. 342–349, 2023, doi: 10.1109/CIST56084.2023.10409962.
[17] K. K. Verma and A. V. Ravi Teja, "Force and Motion Analysis of Blade-less Wind Energy Harvesters," 2023 IEEE Int. Conf. Power Electron. Smart Grid, Renew. Energy Power Electron. Smart Grid, Renew. Energy Sustain. Dev. PESGRE 2023, 2023, doi: 10.1109/PESGRE58662.2023.10405378.
[18] P. K T, T. K. Makanur, P. R, M. M, V. G. S, and K. Manickavasagam, "Design and Analysis of a Miniaturized Vortex Induced Wind Turbine," pp. 1–6, Jul. 2024, doi: 10.1109/AMATHE61652.2024.10582248.
[19] V. Bhardwaj and A. V. Ravi Teja, "Mathematical Modelling and Equivalent Circuit Representation of Bladeless Wind Turbines," IECON Proc. (Industrial Electron. Conf., vol. 2021-October, Oct. 2021, doi: 10.1109/IECON48115.2021.9589902.
[20] "The Future of Wind Turbines? No Blades | WIRED." https://www.wired.com/2015/05/future-wind-turbines-no-blades/ (accessed Sep. 22, 2025).
[21] A. C. R. Buela et al., "Design and Nonlinear Static Simulation of a Small-Scale Vortex Bladeless Wind Power Generator," 2021 IEEE Int. Conf. Autom. Control Intell. Syst. I2CACIS 2021 - Proc., pp. 185–190, Jun. 2021, doi: 10.1109/I2CACIS52118.2021.9495882.
[22] F. E. Tonny, M. K. Hassan kajal, T. Anam, A. M. Tafikul Islam, M. R. Mobarrat, and M. Hassan, "Optimizing Community Energy with Smart Hardware Integration in Offline Microgrid Systems," 2024 IEEE Int. Conf. Power, Electr. Electron. Ind. Appl., pp. 1–6, Sep. 2024, doi: 10.1109/PEEIACON63629.2024.10800723.
[23] S. Pol, B. C. Houchens, D. V. Marian, and C. H. Westergaard, "Performance of aeromines for distributed wind energy," AIAA Scitech 2020 Forum, vol. 1 PartF, pp. 1–8, 2020, doi: 10.2514/6.2020-1241.
[24] "Home." https://aerominetechnologies.com/ (accessed Sep. 22, 2025).
[25] S. Pol, C. Westergaard, D. Marian, and B. Houchens, "Pilot-scale performance of AeroMINE at low wind speeds.," 2021, doi: 10.2172/1870762.
[26] S. Budea, A. Ciocănea, and F. Opriș, "Natural Ventilation of Buildings by Using Venturi Devices Placed on the Rooftops," 2023 11th Int. Conf. ENERGY Environ. CIEM 2023, 2023, doi: 10.1109/CIEM58573.2023.10349752.
[27] "A Norwegian company is working on a wall of floating wind turbines." https://www.cnbc.com/2023/05/16/a-norwegian-company-is-working-on-a-wall-of-floating-wind-turbines.html (accessed Sep. 22, 2025).
[28] "floating 'windcatchers' will rise 1,000 feet to power 80,000 homes each." https://www.designboom.com/technology/norway-wind-catching-systems-wcs-floating-windcatcher-turbine-06-09-2021/ (accessed Sep. 22, 2025).
[29] E. MacMahon and W. E. Leithead, "Performance Comparison of Optimised and Non-Optimised Yaw Control for a Multi Rotor System," 2018 IEEE Conf. Control Technol. Appl. CCTA 2018, pp. 1638–1643, Oct. 2018, doi: 10.1109/CCTA.2018.8511353.
[30] "Wind Catching Systems." https://www.windcatching.com/ (accessed Sep. 22, 2025).
[31] "Wind Catching Systems designs giant floating wind farm with 117 turbines." https://www.dezeen.com/2021/08/26/wind-catching-systems-floating-offshore-farm/ (accessed Sep. 22, 2025).
[32] H. Kathuria, I. Singh, A. Gupta, G. Puniya, and B. Kumar, "Analysis of Bifacial Photovoltaic Panel Under Different Reflective Surfaces," Proc. 3rd IEEE Int. Conf. Power Electron. Intell. Control Energy Syst. ICPEICES 2024, pp. 933–938, 2024, doi: 10.1109/ICPEICES62430.2024.10719302.
[33] S. K. Magableh, C. Wang, and F. Lin, "Utility-Scale Bifacial Solar Photovoltaic System: Optimum Sizing and Techno-Economic Evaluation," IEEE Power Energy Soc. Gen. Meet., 2024, doi: 10.1109/PESGM51994.2024.10688984.
[34] H. L. Tan et al., "Investigation of Bifacial Gain and Albedo of Bifacial Photovoltaic Modules that Operate in a Tropical Site," 2024 8th Int. Conf. Green Energy Appl. ICGEA 2024, pp. 265–270, 2024, doi: 10.1109/ICGEA60749.2024.10560565.
[35] M. M. Hoque et al., "Performance Analysis of a Grid Integrated Bifacial Solar Energy System for Dhaka-Mawa Expressway," 2023 10th IEEE Int. Conf. Power Syst. ICPS 2023, 2023, doi: 10.1109/ICPS60393.2023.10428925.
[36] A. Singh and D. Jones, "Snow Shedding properties of Bifacial PV Panels," Conf. Rec. IEEE Photovolt. Spec. Conf., vol. 2022-June, pp. 646–648, 2022, doi: 10.1109/PVSC48317.2022.9938947.
[37] T. M. Mahim, A. H. M. A. Rahim, and M. M. Rahman, "Weather Responsive Multidimensional Photovoltaic Efficiency Model for Simulation of Custom-Built Bifacial Panel," IEEE J. Photovoltaics, vol. 14, no. 5, pp. 848–860, Jul. 2024, doi: 10.1109/JPHOTOV.2024.3421252.
[38] A. Anjum, A. H. Tanveer, M. K. Sikder, A. Arefin, M. Islam, and M. M. Rahman, "Bifacial Module Based Multilevel Solar Panel System: A Comparative Study," 2020 IEEE Reg. 10 Symp. TENSYMP 2020, pp. 324–327, Jun. 2020, doi: 10.1109/TENSYMP50017.2020.9230649.
[39] J. Li, M. Tang, B. An, and X. Guo, "Research on MPPT Strategy of Bifacial Photovoltaic Power Generation System Based on PSO," 2023 7th Int. Conf.

Creative Commons Attribution BY 4.0 International Licence (CC BY-4.0)

Journal of Marine
Technology and Environment
DOI:10.53464/JMTE.01.2026.07
ISSN (Print): 1844-6116
ISSN (Online): 2501-8795
https://www. jmte.eu

Smart Grid Smart Cities, ICSGSC 2023, pp. 468–473, 2023, doi: 10.1109/ICSGSC59580.2023.10319179.
[40] T. A. Fernandes, A. M. Da Silva Ferraz, V. M. Cavalcante, E. J. Barbosa, M. C. Cabral, and Z. D. Lins, "Analysis of Energy Yield in Bifacial PV Plants as a Function of Installation Factors Through the View Factor Model," COBEP 2023 - 17th Brazilian Power Electron. Conf. SPEC 2023 - 8th IEEE South. Power Electron. Conf. Proc., 2023, doi: 10.1109/SPEC56436.2023.10407162.
[41] P. K. Sahu, S. Karpana, C. Chakraborty, and J. N. Roy, "A Bifacial PV/Battery Three Port Hybrid System for Stand-alone Applications," 2023 IEEE 2nd Ind. Electron. Soc. Annu. On-Line Conf. ONCON 2023, 2023, doi: 10.1109/ONCON60463.2023.10431198.
[42] R. Mahkeswaran, A. K. Ng, C. Toh, and B. Toh, "Maximising Solar Irradiation of Semi-transparent Solar Panels in a Multi-loop Aquaponics System," 5th Technol. Innov. Manag. Eng. Sci. Int. Conf. TIMES-iCON 2024 - Proc., 2024, doi: 10.1109/TIMES-ICON61890.2024.10630753.
[43] K. Nath, B. Nath, M. S. Islam, A. N. Chowdhury, and M. A. Matin, "Exploring the Performance of QDIBSC for Spherical QD Structure," 12th IEEE Int. Conf. Renew. Energy Res. Appl. ICRERA 2023, pp. 445–450, 2023, doi: 10.1109/ICRERA59003.2023.10269410.
[44] A. Kavga, V. Thomopoulos, and T. Petrakis, "The Contribution of Semi-Transparent Photovoltaics for Energy Autonomy in Aloe Vera Greenhouse Cultivation," 2023 31st Mediterr. Conf. Control Autom. MED 2023, pp. 85–88, 2023, doi: 10.1109/MED59994.2023.10185759.
[45] H. Apostoleris, K. Younes, and M. Chiesa, "A simple, semi-empirical performance modeling approach for partially transparent tracking-integrated concentrator photovoltaics," Conf. Rec. IEEE Photovolt. Spec. Conf., pp. 1373–1376, Jun. 2021, doi: 10.1109/PVSC43889.2021.9518698.
[46] A. Ponmalar, A. Jose Anand, P. Saravanan, S. Deeba, and J. Br, "IoT Enabled Inexhaustible E-vehicle using Transparent Solar Panel," 2022 Int. Conf. Commun. Comput. Internet Things, IC3IoT 2022 - Proc., 2022, doi: 10.1109/IC3IOT53935.2022.9767921.

Creative Commons Attribution BY 4.0 International Licence (CC BY-4.0)

Journal of Marine
Technology and Environment
DOI:10.53464/JMTE.01.2026.08

ISSN (Print): 1844-6116
ISSN (Online): 2501-8795
https://www. jmte.eu

ANALYSIS OF SPECIFIC FUEL CONSUMPTION BY SHIP INERT GAS GENERATOR: NITROGEN VS COMBUSTION-TYPE

Kostiantyn RUDYK [1], Olga KHLIYEVA [1]

[1]National University "Odessa Maritime Academy", Ukraine, email address: kostiantynrudyk@gmail.com

Abstract ***:*** The paper compares two methods of generating inert gas on ships. The advantages and disadvantages of two inert gas generators are considered: membrane nitrogen generator and combustion-type generator. Based on the analysis of electricity and fuel consumption of both systems, it was shown that the membrane nitrogen generator outperforms the combustion-type inert gas generator. Specific fuel consumption for a nitrogen generator (at 5 % of oxygen on inert gas) is more than two times less compared with a combustion-type one: 34.8 kg/nm^3 vs 78.5 kg/nm^3. However, when the required oxygen content in the inert gas decreases, the membrane nitrogen generator will be inherent in higher electricity consumption, requiring further analysis of its feasibility compared to the combustion-type one.

Key words : Combustion, comparison, consumption, cost, energy, fuel, inert gas generator, membrane nitrogen generator, ship.

1. INTRODUCTION

Inert gas generation (IGG) systems are critically important for ensuring fire safety on tankers transporting petroleum products. The inert gas system operates on a typical product tanker for approximately 750 hours per year [1]. In modern practice, two main types of such systems are predominantly used: the traditional inert gas generator (combustion-type IGG), which operates based on fuel combustion, and membrane installations for nitrogen production. Given the increasing demands for energy efficiency in maritime transport, especially in the context of implementing the IMO Energy Efficiency Design Index (EEDI) for new vessels, a detailed analysis of both systems in terms of energy consumption is warranted [2].

2. PRINCIPLE OF OPERATION AND ENERGY EFFICIENCY

Combustion-type IGG operates by burning fuel in a special chamber, after which the flue gases are cooled, purified, and delivered to the cargo tanks [3]. The composition of such gas predominantly includes CO_2, N_2, water vapors, and Sulphur impurities, which necessitate purification that contributes to additional power consumption. The overall efficiency coefficient of such systems ranges from 15% to 30% [4].

Membrane nitrogen generators function on the principle of separating compressed air through a polymer membrane, allowing for the extraction of nitrogen with a purity of up to 99.9% [5]. These systems consume electrical energy to operate compressors and are considered not to produce harmful emissions, achieving efficiencies of up to 70% [6].

However, the above statement is not entirely accurate, as ship fuel is burned to operate the compressors on board the vessel. Moreover, it is not entirely clear how to compare the efficiency of combustion-type IGG and the nitrogen generator based on the data from [4] and [6]. Therefore, it is more appropriate to compare the fuel consumption of the two systems rather than the abstract concept of efficiency, which can be calculated differently for these systems.

3. ANALYSIS

The Nitrogen Generator model NCl type approved by DNV (produced by Air Products AS) was chosen for analysis. The operational principle is based on membrane separation. This PRlSM® Nitrogen system, based on PRISM® membranes, allows for continuous on-site production of pure and dry nitrogen from air that can cover various purposes. The main characteristics of the two operation modes are presented in Table 1.

Nitrogen generation is based on the following processes. Compressed air is fed to the Filter & Control

Creative Commons Attribution BY 4.0 International Licence (CC BY-4.0)

Journal of Marine
Technology and Environment
DOI:10.53464/JMTE.01.2026.08
ISSN (Print): 1844-6116
ISSN (Online): 2501-8795
https://www. jmte.eu

Unit and passes through a filter-package which will protect the membranes from harmful particles and oil and water condensate. The air then passes through a heater (electric or heat exchanger type), which will raise the air temperature by min. 5°C to approx. 50°C.

Table 1. Performance data of membrane nitrogen generator

Data	Mode 1	Mode 2
Capacity – Nitrogen Flow, nm^3/h	925	110
N_2 purity (N_2+Argon), vol %	95.4	99.9
N_2 Dew Point (at atm. Pressure), °C	-60	-60
Outlet Pressure, kPa	21	700
Outlet Temperature (max), °C	50	50

The heated air is now fed from the Filter & Control Unit to each Membrane Bank and then to each individual membrane separator. The nitrogen product exiting the membrane modules is collected in a manifold and fed back to the Filter & Control Unit. The Filter & Control Unit is equipped with an oxygen analyzer that will continuously monitor the oxygen content in the nitrogen product. Should the oxygen content, for some reason, rise above the design value, an alarm will be initiated. If the nitrogen consumption is lower than the design, the backpressure in the distribution lines will build up and give a lower product flow. A lower flow in the tum will result in higher nitrogen purity, i.e. less oxygen in the product.

The electricity consumed in the production of nitrogen using the Nitrogen Generator, which is discussed in the paper, is used for the operation of the:

- compressor (the predominant part),
- electric heater for heating the airflow before the membranes,
- powering the control system (a small amount).

The Nitrogen Generator discussed has a water-cooled marine screw compressor DSDX 305 (KAESER compressor) installed. Their main characteristics are the following: max. working pressure 14 bar, min. working pressure 5,5 bar, free air delivery 1162 m^3/h, shaft power 152 kW.

Electricity on board a vessel is produced by burning marine fuel either in the main engine using a shaft generator or in auxiliary engines with electric generators.

The hour fuel consumption for the electricity production for the operation of the Nitrogen Generator:

$$M^{El}_{Fuel} = g_F \cdot (P_c \cdot + P_c), \quad (1)$$

where P_c, and P_c are the electrical power of the compressor and heater; correspondently, kW; g_F is the specific fuel consumption of a diesel generator, kg/kWh (taken 0.185 kg/kWh [7]).

It was calculated that the compressor power when compressing 1162 m^3/h of air to 9 bar (working pressure according to the manometer for mode 1) and with an efficiency of 0.75 is 138 kW. The power of the electric heater for this amount of air when heated by 10 K, considering the heat capacity and density of compressed air according to [8], is 36.2 kW.

For comparison, the Alfa Laval Smit Combustion inert gas system was chosen, which consumes the MDO (DMB or DMC) as fuel. The special burners of the Ultramizing system ensure inert gas production with low NOx emissions and no soot. Quality is further assured by sprayer systems that avoid creating salt crystals through water evaporation.

The energy during inert gas production in a Combustion-type IGG is consumed for the operation of the:

- scrubber pumps,
- gas blower after the generator,
- power supply for the control system (a small amount).

Similar to eq. (1), the hour fuel consumption for the electricity production for the operation of the Combustion-type IGG:

$$M^{El}_{Fuel} = g_F \cdot (P_{SP} \cdot + P_{GB}), \quad (2)$$

where P_{SP}· and P_{GB} are the electrical power of the scrubber pumps and gas blower; correspondently, kW.

For scrubbers in a Combustion-type IGG system, typical power consumption is no more than 7 kW/1000 nm^3 of gas being cleaned. The calculated compressor power when compressing 925 m^3/h of inert gas from a pressure of 0.15 bar after the Combustion-type IGG to 0.5 bar (for supply to cargo tanks) with an efficiency of 0.75 is 10.7 kW.

Fuel consumption for producing 1000 nm^3 of inert gas depends on many factors (fuel type, oxygen content in the inert gas, and others). According to the analysis of information provided by various manufacturers of Combustion-type IGG, the specific fuel consumption is 0.075…0.084 kg of MDO per 1 m^3 of inert gas.

All this data is needed later to compare fuel consumption per unit of inert gas the IGGs produce.

4. RESULTS AND DISSCUTIONS

Table 2 provides information for comparing the combustion-type and the membrane nitrogen inert gas generators.

Creative Commons Attribution BY 4.0 International Licence (CC BY-4.0)

Journal of Marine
Technology and Environment
DOI:10.53464/JMTE.01.2026.08
ISSN (Print): 1844-6116
ISSN (Online): 2501-8795
https://www. jmte.eu

Table 2. Comparison of the Nitrogen IGG and Combustion-type IGG.

Characteristic	Nitrogen IGG	Combustion-type IGG
Operating principle	Air separation through the membrane	Fuel combustion
Oxygen content in inert gas	≈ 0.5...5%, but performance drops and energy consumption increases with lower O_2	≈2...4%, even less without loss of performance
Inert gas purity	High	Low (soot, sulphur oxides even after cleaning)
Initial capital investment	Relatively high (per IG unit)	Relatively low (per IG unit)
Fire safety	High	Fire risk due to fuel
Compactness	High	Low
Sensitivity to air quality	High (requires pre-filtration)	Low
Maintenance complexity	Frequent maintenance costs for membrane and filter replacement	Simple, but requires combustion process monitoring

Information on the components of the total energy consumption of IGGs and the calculated specific fuel consumption for the production of a unit of inert gas are presented in Table 3.

Table 3. Comparison of energy characteristics for Nitrogen IGG and Combustion-type IGG

Characteristic	Nitrogen IGG	Combustion-type IGG
Capacity, nm^3/h	925	
Fuel consumption for combustion in IGG, kg	-	69.4
Electric power consumed by the compressors, kW	137.6	10.7
Power consumed by a heater, kW	36.2	-
Power consumed by scrubber, kW	-	7.0
Fuel consumption for electricity production (auxiliary engine-driven generator), kg	32.2	3.3
Total fuel consumption, kg	32.2	72.6
Specific fuel consumption, kg/nm^3 of IG	34.8	78.5

As can be seen from the results presented in Table 3, in terms of energy consumption, the membrane nitrogen IGG wins over the Combustion-type IGG**.**

5. CONCLUSIONS

Membrane nitrogen inert gas generators, despite a higher installation cost, demonstrate a significant advantage in terms of energy saving, environmental safety, and ease of operation. In the medium and long term, they have lower operating costs, faster payback, and fully comply with modern environmental standards.

A disadvantage of the membrane nitrogen inert gas generators is that their productivity is relatively low. In this regard, they may lose to traditional combustion-type inert gas generators, especially when it is necessary to service large tankers. This issue can be partially resolved by using buffer tanks.

The results of the calculations show that specific fuel consumption for membrane nitrogen IGG is more than two times less compared with combustion-type IGG: 34.8 kg/nm3 vs 78.5 kg/nm3. This indicates the greater efficiency of the membrane nitrogen IGG when used on most merchant vessels. However, in cases where the oxygen content in the inert gas is required to be below 4…5 %, the combustion-type IGG may be more energy efficient than the membrane nitrogen IGG (during operation in mode 2 – Table 1). The issue of the energy feasibility of using one or another method of inert gas production depending on the oxygen content will be considered in my further research.

6. CREdit authors statement

Conceptualization:R.K., K.A.

Creative Commons Attribution BY 4.0 International Licence (CC BY-4.0)

Journal of Marine
Technology and Environment
DOI:10.53464/JMTE.01.2026.08
ISSN (Print): 1844-6116
ISSN (Online): 2501-8795
https://www. jmte.eu

Data curation: R.K., K.A.

Formal analysis: R.K., K.A.

Funding acquisition:-

Investigation: R.K., K.A.

Methodology: R.K., K.A.

Project administration: R.K., K.A.

Resources: R.K., K.A.

Software:-

Supervision: R.K.; K.A.

Validation: R.K., K.A.

Visualization: R.K., K.A.

Writing – original draft: R.K.

Writing – review & editing:.R.K.

7. REFERENCES

[1] Alfa Laval, *Smit Gas Combustion*. https://www.alfalaval.com/products/process-solutions/safety-solutions/inert-gas-system/smit-gas-combustion/.

[2] International Maritime Organization. Energy Efficiency Measures for Ships. London: IMO, 2023.

[3] DNV. Inert Gas Systems on Tankers – Guidelines and Best Practices. DNV Technical Report No. 512, 2022.

[4] Giacomo P., 2021. *Energy Use and Losses in Inert Gas Systems on Oil Tankers*. Journal of Marine Engineering. 2021. Vol. 33, Iss. 2. P. 45–52.

[5] Wärtsilä, 2022. *Nitrogen Generation for Marine Applications*. Technical Data Sheet, 2022.

[6] Smith R., Müller L., 2020. *Membrane-Based Nitrogen Systems: Design and Efficiency*. Ocean Engineering Review. 2020. Vol. 18, Iss. 4. P. 99–108.

[7] Fourth IMO GHG Study 2020. Full Report. London: International Maritime Organization; 2021. https://www.imo.org/en/OurWork/Environment/Pages/Fourth-IMO-Greenhouse-Gas-Study-2020.aspx.

[8] Lemmon E. W., Bell I. H., Huber M. L., McLinden M. O., 2018. *NIST Standard Reference Database 23: Reference Fluid Thermodynamic and Transport Properties-REFPROP*, Version 10.0, NIST, Standard Reference Data Program, Gaithersburg, 2018.

Creative Commons Attribution BY 4.0 International Licence (CC BY-4.0)

Journal of Marine
Technology and Environment
DOI:10.53464/JMTE.01.2026.09

ISSN (Print): 1844-6116
ISSN (Online): 2501-8795
https://www. jmte.eu

DETERMINATION OF OPTIMAL OPERATING MODES OF MARINE DIESEL ENGINES EXHAUST GAS BYPASS SYSTEMS

Anton SAMUSENKO [1], Yurii ZABLOTSKYI [1]& Sergii SAGYN [1]

[1]National University "Odessa Maritime Academy", Odessa, Ukraine, email address: antoshasamusenko@gmail.com

Abstract : A method for determining the optimal operating modes of marine diesel exhaust gas bypass systems is considered. The aim of this research was to determine the optimal volume of exhaust gas bypass for a marine medium-speed diesel engine, specifically the 6L20 Wartsila. Electronic engine control allows flexible adjustment of exhaust gas bypass process within a range of 0 to 10 % of the total volume of gases exiting the diesel cylinder. The use of exhaust gas bypass contributes to improving the environmental performance of marine medium-speed diesel engines, particularly in the operational load range of 55–85 %, where NO_x emissions in exhaust gases decrease by 3.5–15.4 %. The greatest reduction in NOx emissions occurs at loads of 75–85 %. The use of the exhaust gas bypass system is deemed effective for loads exceeding 75 %, with potential reductions in nitrogen oxide emissions ranging from 9.2 % to 15.4 %. For loads of 55–65 %, a reduction in nitrogen oxide emissions (3.3–5.6 %) is also observed, but with a simultaneous increase in specific fuel oil consumption (4.2–4.4 %). However, for certain bypass values, the diesel engine's thermal stress exceeds acceptable limits.

Key words : Efficiency, exhaust gas bypass, exhaust gas recirculation, fuel consumption optimization, marine diesel engine, NO_x emissions, operating mode, performance metrics, , scavenge air pressure, waste-gate, turbocharger bypass ratio.

1. INTRODUCTION

Currently, among the controlled parameters of marine diesel engines, much attention is paid to such an environmental indicator as the concentration of nitrogen oxides NO_X in exhaust gases (Figure 1) [1], [2]. This value is regulated by the requirements of international conventions, and its maintenance in the specified range is mandatory during the operation of ship power plants, both in the waters of the World Ocean and in the territorial waters of maritime countries.

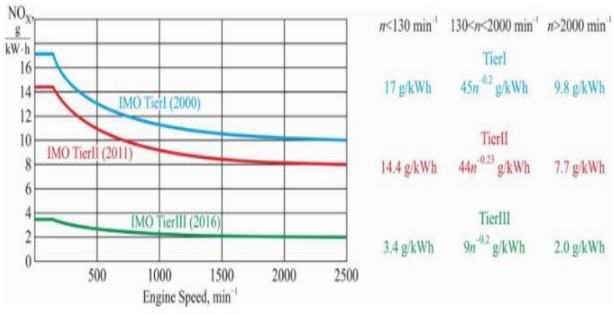

Figure 1 MARPOL-Annex VI-NOx in the exhaust gases of marine diesel engines [2]

The reduction of NO_X concentration in exhaust gases is achieved by:

- influencing the work process occurring in the cylinder;
- changing the design and operating parameters of high-pressure fuel equipment;
- introduction of reagents into exhaust gases during their passage through special reactors;
- by using the exhaust gas management system, which provides either Exhaust Gas Recirculation (EGR) or Exhaust Gas Waste-gate (EWG) [1].

Systems that provide recirculation of exhaust gases (EGR system), as a rule, are used for low-speed diesel engines. For marine medium-speed diesel engines, exhaust gas flow control can be carried out by bypassing them (EWG system). In this case, part of the exhaust gases of the diesel engine go directly to the gas exhaust line, bypassing the gas turbine of the gas turbocharger.

Creative Commons Attribution BY 4.0 International Licence (CC BY-4.0)

Journal of Marine
Technology and Environment
DOI:10.53464/JMTE.01.2026.09
ISSN (Print): 1844-6116
ISSN (Online): 2501-8795
https://www. jmte.eu

At the same time, the frequency of rotation of the gas turbocharger, the pressure and the amount of air injected into the cylinder are reduced. Gases are bypassed with the help of a special valve, which allows you to direct part of the gases not to the gas turbocharger, but directly to the gas exhaust pipe. Currently, EWG systems are installed on marine medium-speed main and auxiliary diesel engines [2].

The use of the EGW system ensures a decrease in the concentration of NO_X in the exhaust gases, however (due to the deterioration of the combustion process) the power of the diesel engine decreases and the specific effective fuel consumption increases. In addition, the bypass of gases leads to an increase in the temperature stress of the diesel engine [3].

2. MATERIALS AND METHODS

The aim of this research was to determine the optimal volume of exhaust gas bypass for a marine medium-speed diesel engine, specifically the 6L20 Wartsila. When utilizing the EGW system, part of the exhaust gases is directed into the exhaust system bypassing the gas turbocharger. Electronic engine control allows flexible adjustment of this process within a range of 0 to 10 % of the total volume of gases exiting the diesel cylinder [4 - 6].

Research was conducted on three identical 6L20 Wartsila diesel engines with an electronic control system for fuel, air and gas distribution phases. The diesels were part of the ship's power plant as diesel generators, had the same engine life and were operated at equal loads. The EWG system is installed as an exhaust gas management system on these diesel engines. The Wartsila company recommends the use of this system primarily to limit the pressure of supercharged air and prevent surging phenomena during high loads and as an additional function – to reduce NO_X emissions. According to the project documentation, the EWG system provides the bypass of gases in the range of 0-10 % of their total volume. The schematic diagram of the 6L20 Wartsila marine diesel engine EWG system is shown in Figure 2 [7].

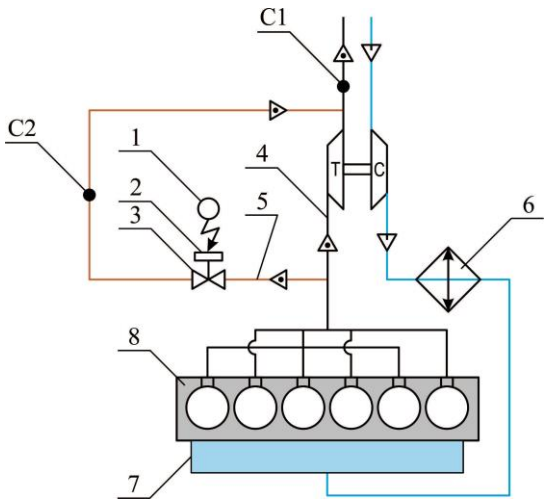

Figure 2 Schematic diagram of a marine medium-speed diesel engine 6L20 Wartsila with EWG exhaust gas management system [7]

Where:
1 – bypass valve position controller; 2 – pneumatic drive of the bypass valve; 3 – waste-gate valve; 4, 5 – outlet lines of the main and bypass flow of gases; 6 – charge air cooler; 7 – purge receiver; 8 – diesel cylinders; C1, C2 – gas flow control points;
T, C – gas turbine and air compressor of the turbocharger.

The air pumped in by the compressor is cooled in the charge air cooler 6 and enters the cylinders 8 through the purge receiver 7. The diesel engine implements a pulsed gas turbine supercharging system, in which the gas from the cylinders 8 is fed to the blades of the turbocharger through separate gas ducts. Depending on the position of the bypass valve 3 (the movement of which is carried out using a pneumatic drive 2 and regulated by the controller 1), the exhaust gases enter either the main line 4 or the bypass 5.

3. RESULTS AND DISSCUTIONS

The consumption of exhaust gases in the lines 4 and 5 was determined at points C_1 and C_2 using flowmeter. During the experiment, the NO_X concentration in the exhaust gases was determined using a gas analyzer at point C_1. The specific fuel oil consumption (SFOC) was determined with the help of ship measuring devices [2, 6].

The degree of gas bypass was calculated according to the formula [8]:

$$\delta_{EWG} = \frac{G_w}{G_\Sigma} \cdot 100\%, \quad (1)$$

where G_w – is the amount of exhaust gases that passed through the bypass valve, kg/s (measured at point C_2 using a flow meter);

Creative Commons Attribution BY 4.0 International Licence (CC BY-4.0)

Journal of Marine
Technology and Environment
DOI:10.53464/JMTE.01.2026.09
ISSN (Print): 1844-6116
ISSN (Online): 2501-8795
https://www. jmte.eu

G_Σ – is the total amount of exhaust gases entering the gas exhaust line from the gas turbocharger with the bypass valve completely closed, kg/s (measured at point C1 using a flow meter).

The error in gas flow measurement did not exceed ±0.5 %, the error in measuring NO_X emission in exhaust gases did not exceed ±3.5 %, the error in measuring the specific effective fuel consumption did not exceed ±2.5 %.

The diesel, on which experimental studies were carried out, provided power to permanent groups of consumers. At the same time (depending on the studied modes) its power was 660 kW, 805 kW, 890 kW, 1010 kW, which corresponded to $0.55N_{enom}$, $0.67N_{enom}$, $0.74N_{enom}$, $0.83N_{enom}$. The error in power change did not exceed ±1.5 %.

The ship's power plant included three diesel engines of the same type, therefore, in the event of a change in the number of energy consumers and their power, the necessary load was redistributed to the diesel engines not involved in the experiment, while the diesel engine on which the research was carried out was operated at a constant load. In addition, during the diesel experiment, constant temperature conditions were maintained in the lubrication and cooling systems.

During the experiment, the diesel operated for 2.5–3 hours at a constant load and with an unchanged position of the bypass valve in each of the experimental modes.

To determine the degree of opening of the waste-gate valve, first, at point C1, the total gas flow G_Σ was determined, leaving the diesel cylinders and passing through the main gas flow line 4 (with fully closed valve 3).

After that, with the changed position of the waste-gate valve 3 at the point C_2, the gas flow G_w through the bypass line 5 was determined and the degree of gas bypass δ_{EWG} was calculated using formula (1).

The diesel cylinders exhaust gases average temperature – t_{eg}, which was measured by the ship's Doctor diagnostic system, was taken as a criterion for the thermal stress of the diesel engine.

The exhaust gases temperature is recommended by diesel manufacturing companies and scientific researchers as criteria for evaluating the course of the work process and the condition of high-pressure fuel equipment [9-10].

The results of the research are shown in Figure 3.

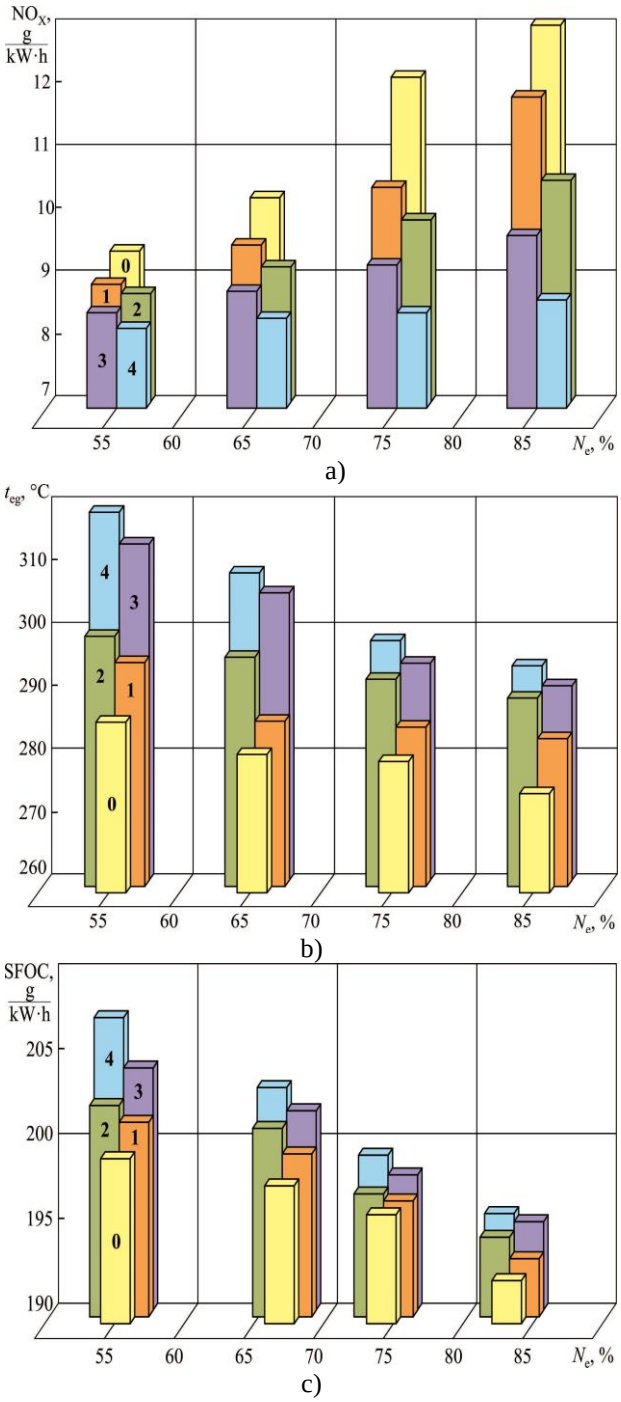

Figure 3 Change in a) NO_X emission, b) t_g, °C, and c) SFOC, for different loads N_e, %, marine diesel engine 6L20 Wartsila and different grades gas bypass [9] δ_{EWG}:
0 – no bypass; 1 – 3.8 %; 2 – 6.0 %; 3 – 8.1 %, 4 – 9.6 %

4. CONCLUSIONS

Analysing the above results we can draw the following conclusions:

- During the operation of marine diesel engines, it is necessary to ensure their environmental

Creative Commons Attribution BY 4.0 International Licence (CC BY-4.0)

Journal of Marine
Technology and Environment
DOI:10.53464/JMTE.01.2026.09
ISSN (Print): 1844-6116
ISSN (Online): 2501-8795
https://www. jmte.eu

performance, particularly concerning nitrogen oxides (NOx) emissions that are part of the exhaust gases. One method explored for reducing NOx emissions is the Exhaust Gas Waste-Gate (EGW), where a portion of diesel exhaust gases is directed into the exhaust gas bypassing system.

- While the use of the EGW system reduces NO_x concentration in exhaust gases, it also leads to a decrease in diesel engine power and an increase in specific fuel consumption due to the deterioration of the combustion process. Additionally, exhaust gas bypass contributes to an increase in the temperature stress on the diesel engine.
- The use of exhaust gas bypass contributes to improving the environmental performance of marine medium-speed diesel engines, particularly in the operational load range of 55–85 %, where NOx emissions in exhaust gases decrease by 3.5–15.4 %. The greatest reduction in NOx emissions occurs at loads of 75–85 %, which are common operating conditions for marine medium-speed diesel engines.
- The use of the EGW system results in an increase of the thermal stress on the diesel engine, which can be assessed by the temperature of the exhaust gases.
- To determine the effectiveness of the EGW system as a means of meeting the requirements of MARPOL Annex VI for limiting NOx emissions, a comprehensive assessment of the diesel engine's operation parameters is necessary. This includes the reduction of nitrogen oxides in exhaust gases, the increase in specific fuel consumption, and the increase in exhaust gas temperatures. The optimal level of gas bypass should be chosen based on achieving the maximum reduction in nitrogen oxide emissions with minimal increase in fuel consumption while simultaneously maintaining exhaust gas temperatures within acceptable thermal stress levels.
- The use of the EGW system is deemed effective for loads exceeding 75 %, with potential reductions in nitrogen oxide emissions ranging from 9.2 % to 15.4 %. For loads of 55–65 %, a reduction in nitrogen oxide emissions (3.3–5.6 %) is also observed, but with a simultaneous increase in fuel consumption (4.2–4.4 %). However, for certain bypass values, the diesel engine's thermal stress exceeds acceptable limits.
- These results confirm the feasibility of using the EGW system to reduce NOx emissions. However, its most rational use may be as an additional method in combination with an exhaust gas recirculation system, requiring further research.

5. ACKNOWLEDGMENTS

The authors thank Constanta Maritime University for support to publish this work.

6. FUNDING

No funding for this work.

7. CREdit authors statement

Conceptualization, Data curation, Formal analysis, Investigation, Methodology, Project administration, Resources, Software, Supervision, Validation, Visualization: : S.A; Z.Y; S.S.

Funding acquisition:-No funding

Writing – original draft, riting – review & editing: S.A.

8. REFERENCES

[1] Sagin, S.V.; Kuropyatnyk, O.A.; Zablotskyi, Y.V.; Gaichenia, O.V., 2022. *Supplying of Marine Diesel Engine Ecological Parameters,* Naše More International Journal of Maritime Science and Technology, *69*, 53–61. https://doi.org/10.17818/NM/2022/1.7.

[2] Sagin S., Kuropyatnyk O., Sagin A., Tkachenko I., Fomin O., Píštěk V., Kučera P. 2022. *Ensuring the Environmental Friendliness of Drillships during Their Operation in Special Ecological Regions of Northern Europe*. International Journal of Maritime Science and Engineering, *10* (9), 1331, https://doi.org/10.3390/jmse10091331.

[3] Ni, P.; Wang, X.; Li, H, 2020. *A review on regulations, current status, effects and reduction strategies of emissions for marine diesel engines,* Fuel, *279*, 118477, https://doi.org/10.1016/j.fuel.2020.118477.

[4] Sagin, S.V.; Kuropyatnyk, O.A., 2018. *The Use of Exhaust Gas Recirculation for Ensuring the Environmental Performance of Marine Diesel Engines* , Naše More Int. J. Marit. Sci. Technol., *65*, 78–86. https://doi.org/10.17818/NM/2018/2.3.

[5] Sagin, S.; Haichenia, O; Karianskyi, S.; Kuropyatnyk, O; Razinkin, R; Sagin, A., 2025, *Improving Green Shipping by Using Alternative Fuels in Ship Diesel Engines*. J. Mar. Sci. Eng., *13*(3), 589. https://doi.org/10.3390/jmse13030589.

[6] Van, T.G.; Ramirez, J.; Ristovskim, Z.; Brown, R.J., 2019. *Global impact of recent IMO regulation on marine fuel oil refining processes and ship emissions*.Transportation Research Part D Transport & Environment, *70*, 123-134,

Creative Commons Attribution BY 4.0 International Licence (CC BY-4.0)

Journal of Marine
Technology and Environment
DOI:10.53464/JMTE.01.2026.09
ISSN (Print): 1844-6116
ISSN (Online): 2501-8795
https://www. jmte.eu

https://doi.org/10.1016/j.trd.2019.04.001.

[7] Kuropyatnyk, O.A. Sagin, S.V., 2019. *The Exhaust Gas Recirculation as a Major Technique Designed to Reduce NOx Emissions from Marine Diesel Engines*. Naše More Int. J. Marit. Sci. Technol., *66*, 1–9. https://doi.org/10.17818/NM/2019/1.1.

[8] Chena, Z.; Chena, H.; Wang, L.; Geng, L.; Zen, K., 2020. *Parametric study on effects of excess air/fuel ratio, spark timing, and methanol injection timing on combustion characteristics and performance of natural gas/methanol dual-fuel engine at low loads*. Energy Conversions & Management, *210*, 112742, https://doi.org/10.1016/j.enconman.2020.112742.

[9] Castells-Sanabra, M.; Borén, C.; van der Meer, R.; Torralbo, J.; Ordás, S., 2020. *Existing Emission Calculation Methods Applied to Monitoring, Reporting and Verification (MRV) on Board*. Naše More International Journal of Maritime Science and Technology, *67*, 163–171, ISSN 0469-6255, E-ISSN 1848-6320, DOI 10.17818/NM/2020/2.9, https://www.nasemore.com/existing-emission-calculation-methods-applied-to-monitoring-reporting-and-verifi-cation-mrv-on-board/.

[10] Lopatin, O.P., 2020. *Study of the influence of the degree of exhaust gas recirculation on the working process of a diesel.*Journal of Physics:conference Series, *1515*, 042021, https://iopscience.iop.org/article/10.1088/1742-6596/1515/4/042021.

Creative Commons Attribution BY 4.0 International Licence (CC BY-4.0)

Journal of Marine
Technology and Environment
DOI:10.53464/JMTE.01.2026.10

ISSN (Print): 1844-6116
ISSN (Online): 2501-8795
https://www. jmte.eu

THERMAL BALANCE ANALYSIS OF THE MAN B&W 6S50ME-C MARINE DIESEL ENGINE

Andrei Răzvan TUDOR [1], Bogdan Mihai VÂRLAN [1]

[1]Constanta Maritime University, Faculty of Naval Electro-Mechanics, 104 Mircea cel Batran Street, 900663, Constanta, Romania, ORCID ID 0009-0004-3328-3825,e-mail address: trazvan72@gmail.com

Abstract : This study investigates the thermal balance of a MAN B&W 6S50ME-C two-stroke marine engine operating as the main propulsion system of a 40,000 DWT Oil/Chemical Tanker. Within the current maritime context, where fuel efficiency and emission reduction have become major priorities, a clear understanding of how thermal energy is distributed inside large marine engines is essential for performance optimization and energy recovery solutions. The objective of the paper is to determine how the energy released during fuel combustion is converted into useful mechanical work and how it is dissipated through various loss mechanisms. The analysis is based on a detailed thermal balance calculation using real operational data, such as effective engine power, specific fuel consumption, cooling fluid flow rates, lubrication oil parameters, and exhaust gas temperatures. The applied methodology consists of thermal balance calculations based on established thermodynamic relations, expressed in absolute, relative and percentage terms. The results indicate that approximately 40.98% of total thermal energy supplied by the fuel is transformed into effective mechanical output. A significant part of the remaining energy is lost through exhaust gases, accounting for about 29.37%, while cooling systems represent approximately 22.32% of total losses. Additional minor losses, including radiation and mechanical friction represent around 7.04%.The analysis confirms that exhaust gas losses constitute the dominant source of recoverable thermal energy. Consequently, the study highlights the importance of exhaust heat recovery systems as an effective means to improve overall engine efficiency, reduce fuel consumption, and support more sustainable marine propulsion operations.

Key words : Exhaust gas losses, Marine diesel engine, MAN B&W 6S50ME-C, Thermal balance, Waste heat recovery.

1. INTRODUCTION

Internal combustion engines convert the energy released during fuel combustion into mechanical work. In practice, only part of this energy is effectively transformed into useful output, while the remaining amount is dissipated toward the cold source. For this reason, engine operation is characterized by a specific thermal efficiency. The distribution of energy within an internal combustion engine can be described in a comprehensive manner by means of the thermal balance, which is obtained through thermal calculations and is commonly used to evaluate energy losses and the potential for residual heat recovery.

Depending on the form of expression, the thermal balance can be presented as:

- hourly, when the energy terms are expressed in [kJ/h];
- energetic, when the terms are given in [kJ/kWh];
- percentage, when the results are expressed as percentages.

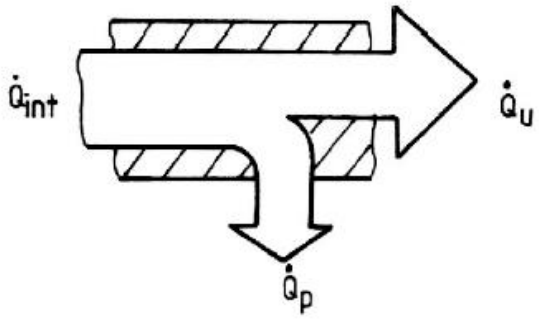

Figure 1 Energy distribution within a transformation process

Creative Commons Attribution BY 4.0 International Licence (CC BY-4.0)

Journal of Marine
Technology and Environment
DOI:10.53464/JMTE.01.2026.10
ISSN (Print): 1844-6116
ISSN (Online): 2501-8795
https://www. jmte.eu

2. ENGINE DESCRIPTION AND MAIN TECHNICAL DATA

The engine analysed in this study is a DOOSAN–MAN B&W 6S50ME-C9.5-TII, manufactured by DOOSAN ENGINE Co., Ltd., in compliance with the requirements of the Registro Italiano Navale (RINA) classification society, applicable at the time of contract conclusion between MAN Diesel & Turbo and the Korean engine builder.

- Engine application: Main propulsion engine for a 40,000 DWT oil tanker;
- Engine type: Two-stroke, medium-speed, turbocharged, reversible marine diesel engine, coupled to a fixed-pitch propeller;
- Number of cylinders: i = 6, in-line configuration;
- Cylinder bore: D = 0.500 m;
- Piston stroke: S = 2.214 m;
- Engine power: P_{en} = 6,480 kW (8,812 BHP).

3. THERMAL BALANCE METHODOLOGY

To describe the distribution of energy resulting from the combustion process, the energy balance of the marine engine is expressed in mathematical form by accounting for the useful mechanical output and the main heat loss components.

In absolute terms, the energy balance relation of a marine engine is given by:

$$Q_{tot} = Q_u + Q_{cl} + Q_{gl} + Q_{dl} \text{ [kJ/h]}, \quad (1)$$

where:

1. Q_{tot} - the energy flow resulting from fuel combustion and calculated using the following relation:

$$Q_{tot} = c_e \cdot P_e \cdot Q_i \text{ kJ/h} \quad (2)$$

$$Q_{tot} = 5.692 \cdot 10^7 \text{ kJ/h}$$

where: $c_e = 0.208\ kg/kWh$ - effective hourly fuel consumption

Q_i=4.229*10^4 kJ - lower heating value of the fuel

$P_e = 6480\ KW$-effective engine power

2. Q_u - the useful heat flow (corresponding to the useful mechanical work) and calculated using the following relation:

$$Q_u = 3600 \cdot P_e \quad (3)$$

$$Q_u = 2.333 \cdot 10^7 kJ/h$$

3. Q_{pr} - heat flow lost through the cooling fluids of the engine components
4. Q_{pg} - heat flow lost through the exhaust gases discharged from the engine
5. Q_{pd} - miscellaneous heat losses that cannot be directly evaluated

By relating equation (1) to the effective engine power, the energy balance expressed in relative terms is obtained:

$$q_{tot} = q_u + q_{pr} + q_{pg} + q_{pd} \text{ [kJ/kWh]} \quad (4)$$

From this relation, the percentage form of the thermal balance can be derived:

$$100 = q_u + q_{pr} + q_{pg} + q_{pd} \quad (5)$$

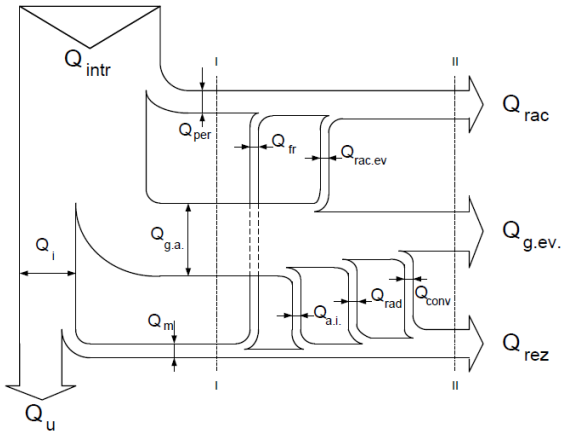

Figure 2 Energy balance diagram of the MAN B&W 6S50ME-C engine

A clear graphical representation of the energy balance of a marine engine is provided by the diagram shown in Figure 2. Within this energy balance diagram, the following energy flows cross the balance boundary:

✓ the total thermal energy input supplied by the fuel;

✓ the useful energy flow corresponding to the effective power developed by the engine;

✓ the heat flow lost through the cooling fluids, which is given by:

$$Q_{pr} = Q_{cc} + Q_{pc} + Q_{ras} + Q_{injc} + Q_{oc} \quad (6)$$

Where:

1. Q_{cc} - the heat flow removed from the engine through the cooling water of the cylinders and the turbocharger, which depends on the cooling water flow rate $\dot{m}_{rc}$ and on the temperature difference between the outlet cooling water temperature t_{rc2} and the inlet cooling water temperature t_{rc1}, and is calculated using the following relation:

$$Q_{cc} = \dot{m}_{rc} \cdot c_a \cdot (t_{rc2} - t_{rc1}) \quad (7)$$

$$Q_{cc} = 8.19 \cdot 10^6 \text{ kJ/h}$$

Where: $\dot{m}_{cc} = \rho_{rc} \cdot G_{rc}$ (8)

$\dot{m}_{cc} = 150000$ kg/h

$c_a = 4.2$ kJ/kW$\cdot K$

$t_{cc2} = 83$ C

$t_{cc1} = 75$ C

2. Q_{cp} - the heat flow removed through piston cooling water:

$$Q_{cp} = \dot{m}_{cp} \cdot c_{cp} \cdot (t_{cp2} - t_{cp1}) \quad (8)$$

Creative Commons Attribution BY 4.0 International Licence (CC BY-4.0)

Journal of Marine
Technology and Environment
DOI:10.53464/JMTE.01.2026.10
ISSN (Print): 1844-6116
ISSN (Online): 2501-8795
https://www. jmte.eu

$$Q_{cp} = 8.239 \cdot 10^5 \text{ [kJ/h]}$$

Where: $\dot{m}_{cp} = \rho_{cp} \cdot G_{cp}$ (10)

$\dot{m}_{cp} = 422500$ kg/h

$c_a = 4.2$ kJ/kW$\cdot K$

$t_{cp2} = 55$ C

$t_{cp1} = 45$ C

3. Q_{injc} - the heat flow removed from the engine through the injector cooling fluid (diesel fuel), which depends on the cooling fluid flow rate $\dot{m}_{rinj}$, its specific heat c_{fl}, and the temperature difference between the inlet and outlet of the cooling fluid Δt_{inj}, and is calculated using the following relation:

$$Q_{injc} = \dot{m}_{injc} \cdot c_{fl} \cdot \Delta t_{inj} \quad (11)$$

$$Q_{injc} = 1.68 \cdot 10^5 \text{ kJ/h}$$

Where: $\dot{m}_{injc} = \rho_{injc} \cdot G_{injc}$ (12)

$\dot{m}_{injc} = 4200$ kg/h

$c_{fl} = 2$ kJ/kW$\cdot K$

$\Delta t_{inj} = 20$ C.

4. Q_{oc} - the heat flow removed from the engine through the lubricating oil, depending on the oil flow rate $\dot{m}_{ulei}$and the oil temperatures at the inlet $t_{u1}$and outlet t_{u2}, and calculated using the following relation:

$$Q_{oc} = \dot{m}_o \cdot c_o \cdot (t_{o2} - t_{o1}) \quad (13)$$

$$Q_{oc} = 3.69 \cdot 10^6 \text{ kJ/h}$$

where:

$$\dot{m}_o = \rho_o \cdot G_o \quad (14)$$

$\dot{m}_o = 4200$ kg/h

$c_{fl} = 2$ kJ/kW$\cdot K$

$t_{o2} = 55$ C

$t_{o1} = 45$ C

5. Q_{egl} - the heat flow lost through the exhaust gases discharged from the engine, which can be expressed by the following relation:

$$Q_{egl} = c_e \cdot P_e \cdot [v''_{ga} \cdot (a'_{am} + b'_{am} \cdot T_{ev}) \cdot T_{ev} - L \cdot (a_{aer} + b_{aer} \cdot T_{aer}) \cdot T_{aer}] \quad (15)$$

$$Q_{egl} = 1.672 \cdot 10^7 \text{ kJ/h}$$

$$T_{eg} = T_b \cdot \left(\frac{p_a}{p_b}\right)^{\frac{n_e - 1}{n_e}} \quad (16)$$

$$T_{eg} = 791.367\ K.$$

6. Q_{rez} - the heat flow associated with miscellaneous losses that cannot be evaluated by measurements.

$$Q_{rez} = Q_{tot} - (Q_u + Q_{cc} + Q_{cp} + Q_{injc} + Q_{oc} + Q_{egl}) \quad (17)$$

$$Q_{rez} = 4.006 \cdot 10^6\ kJ/h.$$

As can be observed from the energy balance diagram of the marine engine, the heat flow equivalent to mechanical losses, Q_{mec}, which includes friction losses and the mechanical consumption of the engine auxiliary mechanisms, is partly transferred to the cylinder cooling water due to piston ring friction, Q_{frs}. Another part, corresponding to bearing friction losses, Q_{fr1}, is transferred to the lubricating oil, while the remaining portion contributes to the miscellaneous loss flow. This includes heat lost by radiation to the surrounding environment, Q_{rad}, heat associated with incomplete combustion, Q_{ain}, as well as the heat equivalent to the kinetic energy of the exhaust gases discharged from the engine, Q_{gcin}.

Relative thermal balance:

$$q'_u = 100 \cdot \frac{Q_u}{Q_{tot}} \quad (18)$$

$$q'_u = 40.981\ \%$$

$$q'_{cooling} = 100 \cdot \left(\frac{Q_{cc}}{Q_{tot}} + \frac{Q_{cp}}{Q_{tot}} + \frac{Q_{injc}}{Q_{tot}} + \frac{Q_{oc}}{Q_{tot}}\right) \quad (19)$$

$$q'_{cooling} = 22.32\%$$

$$q'_{egl} = 100 \cdot \frac{Q_{pgev}}{Q_{tot}} \quad (20)$$

$$q'_{egl} = 29.37\%$$

$$q'_{rez} = 100 \cdot \frac{Q_{rez}}{Q_{tot}} \quad (21)$$

$$q'_{rez} = 7.037\%$$

It can be observed that, among the thermal energy losses, the largest share is represented by the losses through the exhaust gases discharged from the engine, which constitute the most significant source of thermal energy and should therefore be the primary target for recovery efforts.

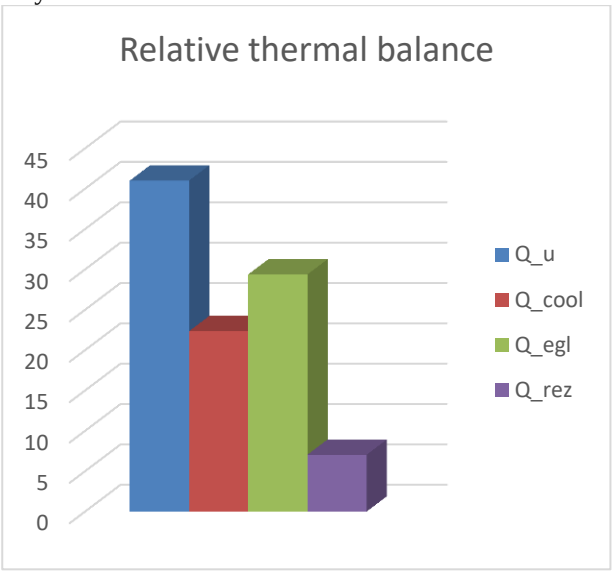

Figure 3. Graphical representation of the relative thermal balance

The graphical representation of the thermal balance highlights the manner in which energy flows are distributed throughout the engine system.

Creative Commons Attribution BY 4.0 International Licence (CC BY-4.0)

Journal of Marine
Technology and Environment
DOI:10.53464/JMTE.01.2026.10
ISSN (Print): 1844-6116
ISSN (Online): 2501-8795
https://www. jmte.eu

4. CONCLUSIONS

The analysis shows that exhaust gases represent the dominant source of thermal losses, followed by losses

associated with the cooling water and lubricating oil systems. These findings indicate that exhaust gas heat recovery and improved cooling system management offer significant potential for increasing the overall efficiency of marine propulsion plants.

In the context of the ongoing decarbonisation of the maritime industry, a detailed assessment of the thermal balance becomes essential, as it provides a solid basis for identifying energy-saving measures and supporting the development of more efficient and environmentally sustainable propulsion systems.

6. FUNDING

This paper received no external funding.

8. CREdit authors statement

Conceptualization: T.A.R.

Data curation; T.A.R.

Formal analysis: V.B.M.

Funding acquisition: -

Investigation: T.A.R.

Methodology: T.A.R.

Project administration: T.A.R.

Resources: T.A.R.

Software: T.A.R.

Supervision: V.B.M.

Validation: V.B.M.

Visualization: V.B.M.

Writing – original draft: T.A.R.

Writing – review & editing: V.B.M.

8. REFERENCES

[1] Buzbuchi, N., Sabău, A., 2006, Procese, caracteristici și supraalimentarea motoarelor navale, Editura Nautica, Constanța.

[2] MAN Diesel & Turbo, Technical Documentation: MAN B&W ME/ME-C, Copenhagen SV, Denmark, www.mandieselturbo.com.

[3] MAN Diesel, 2006, Operation Manual – 50-108ME/ME-C, Volume I, Edition 0003, MAN Diesel A/S.

[4] MAN Energy Solutions, 2021, ME-C Engines Technical Manual – Operation and Maintenance, Copenhagen.

[5] Ciucur, V.V., Increasing the efficiency of marine energy conversion, *Journal of Marine Technology and Environment*, vol. 2, 2021, 7-10, Nautica publish House, Constanta, Romania.

[6] LEO TERESA J., NAVARRO EMILIO, RASO MIGUEL A., RODRIGUEZ-CORTIJO JOSE M., COBO JUAN M., The dead state choice in exergy calculations for marine and naval applications, *Journal of Marine Technology and Environment*, vol. 1, 2012, 67-74, Nautica publish House, Constanta, Romania.

Creative Commons Attribution BY 4.0 International Licence (CC BY-4.0)

PUBLISHED SINCE : 2008

ISSN (Print): 1844-6116 ISSN (Online): 2501-8795

ON LINE SINCE : 2008

https://www. jmte.eu

PUBLISHED BY : EDITURA NAUTICA/CONSTANTA MARITIME UNIVERSITY

ISSN: 1844-6116